Christina Arras

A Global Survey of Sporadic E Layers based on GPS Radio Occultations by CHAMP, GRACE and FORMOSAT−3 / COSMIC

Christina Arras

A Global Survey of Sporadic E Layers based on GPS Radio Occultations by CHAMP, GRACE and FORMOSAT–3 / COSMIC

Dissertation
zur Erlangung des akademischen Grades
Doktor der Naturwissenschaften (Dr. rer. nat.)

eingereicht an der Fakultät für Physik und Geowissenschaften
der Universität Leipzig

September 2010

Scientific Technical Report STR10/09

Summary

The ionosphere is a part of the upper atmosphere stretching from a height of about 60 km to more than 1 000 km. A certain fraction of the gas particles in that region is ionised by solar extreme ultra violet radiation. Since electromagnetic waves are influenced and significantly modified by ionospheric free charge carriers, the altitude range is of great scientific interest.

GPS satellites emit electromagnetic waves on $L-$band frequencies travelling through the ionosphere and lower neutral atmosphere. Subsequently, they are received by low–Earth orbiting satellites. Consequently, the signals are affected by strong electron density gradients at altitudes above approximately 80 km and by atmospheric density, pressure and water vapour content in the troposphere and stratosphere. This measurement method is termed radio occultation technique and it allows to receive a global picture of ionospheric and lower neutral atmospheric conditions.

This study focusses on the detection and analysis of sporadic E layers from GPS radio occultation measurements on a global scale. Sporadic E layers are localised patches of relatively high electron density appearing in the E region of the ionosphere. They are represented in GPS signals as intense fluctuations.

This work reveals that global sporadic E occurrence rates underlie variations on different time scales. It is demonstrated that the sporadic E occurrence depends on several geophysical parameters and it is subject to coupling processes between the neutral atmosphere and ionosphere. For example, the global sporadic E occurrence is oriented along Earth's magnetic field. It is shown additionally that sporadic E altitudes are subject to tidal winds and that its annual cycle varies with meteor influx.

Contents

List of Figures

List of Tables

Acronyms and abbreviations

C / A code	Coarse / Acquisition code
CHAMP	CHAllenging Minisatellite Payload
COSMIC	Constellation Observing System for Meteorology, Ionosphere and Climate
DLR	Deutsches Zentrum für Luft - und Raumfahrt (German Aerospace Center)
DIAS	European Digital upper Atmospheric Server
DT	Diurnal Tide
E_s	Sporadic E
EUV	Extreme Ultra Violet
ESA	European Space Agency
FORMOSAT–3	FORMOsa SATellite mission–3
GFZ	German Research Center for Geosciences
GLONASS	GLObal NAvigation Satellite System
GNSS	Global Navigation Satellite System
GPS	Global Positioning System
GPS / MET	Global Positioning System / METeorology Program
GRACE	GRAvity recovery and Climate Experiment
GSWM	Global Scale Wave Model
HF	High Frequency
IGRF	International Geomagnetic Reference Field
IGOR	Integrated GPS Occultation Receiver
IGS	International GNSS Service for Geodynamics
ISR	Incoherent Scatter Radar
JPL	Jet Propulsion Laboratory
LEO	Low Earth Orbiter
MLT	Mesosphere / Lower Thermosphere
MPS	Multiple Phase Screen
MR	Meteor Radar
NASA	National Aeronautics and Space Administration
NAVSTAR	NAVigation Satellite Timing And Ranging
NSPO	National SPace Organization

P – code	Precision – code
PRN	Pseudo Random Noise
RO	Radio Occultation
SAC–C	Satellite de Aplicaciones Cientificas–C
SDT	Semidiurnal Tide
SNR	Signal–to–Noise Ratio
SuperDARN	Super Dual Auroral Radar Network
TEC	Total Electron Content
TIDs	Travelling Ionospheric Disturbances
UCAR	University Corporation for Atmospheric Research
UHF	Ultra High Frequency
UT	Universal Time
UV	Ultra Violet
VHF	Very High Frequency
WINDII	WIND Imaging Interferometer

List of symbols

α	bending angle
a	impact parameter
A	intercept of regression line
$A_{m,s}$	amplitude of tides
B	slope of regression line
$\vec{B}$	Earth's magnetic field
B_0	total intensity of Earth's magnetic field
B_{hori}	horizontal intensity of the Earth's magnetic field
c_0	speed of light in vacuum
d	phase delay
D	diffusion coefficient
$\vec{E}$	electric field
e	elementary charge
e^-	free electron
ε_0	permittivity
f_{L1}	frequency of GPS L_1 signal
f_{L2}	frequency of GPS L_2 signal
f_c	critical frequency
g	acceleration due to gravity
H	scale height
h	altitude
$h_{E,F}$	altitude of E or F layer
h'	virtual height
$h'E_s$	virtual height of sporadic E layer
I	inclination of the magnetic field
K	constant value
λ	longitude
λ_1	wavelength of GPS L_1 signal
λ_2	wavelength of GPS L_2 signal
λ_c	critical wavelength
m	subharmonic of a solar day
M_a	molecular mass of dry air
m_e	electron mass
m_i	ion mass

ν	ion neutral collision frequency
N	refractivity
n	refractive index
N_e	electron density
Ω	rotation of Earth, angular velocity
ω	ion cyclotron frequency
$\phi_{m,s}$	phase of tides
p	pressure
ρ	air density
R	correlation coefficient
R_g	universal gas constant
s	zonal wave number
S	wind shear
$S_0 F$	ratio of vertical ion velocity to horizontal ion velocity
Std	standard deviation
T	temperature
$\widetilde{TEC}$	calibrated TEC values
$\vec{u_n} = (U, V, W)$	neutral wind velocity
$\vec{v_i} = (v_1, v_2, v_3)$	ion velocity
w	liquid water content
x	horizontal distance in MPS model
z	vertical distance

Chapter 1

Introduction

Our planet is surrounded by a shell consisting of gas – the atmosphere. The atmosphere is the fundament for life on Earth due to its chemical composition. Major constituents are nitrogen, oxygen and argon. Further, several trace gases like methane, CO_2, ozone, several other noble gases and a variable amount of water vapour are present.

The focus of this study is set on the Earth's ionosphere, a region that stretches between 60 km above surface up to about 1000 km. Special focus is set to the lower boundary of a region called E layer which is located at altitudes between 90 and 125 km. A certain fraction of the air molecules is ionised due to their direct exposition to solar radiation. Since this altitude range works as a link between space and the lower neutral atmosphere, it is subject to influences from above and below. Optical phenomena, e.g., meteors and polar lights also appear in this altitude range. They are exited mainly by interactions between extraterrestrial energy and particle influx with the ionospheric gas. Simultaneously, neutral gas processes from below influence the ionosphere. Atmospheric waves, especially gravity waves and solar tides, have an impact on the movement of charged particles. The tides are induced by absorption of solar radiation in the lower atmosphere, propagate upward dominating the wind field of the mesosphere and thermosphere.

Interactions of several atmospheric and ionospheric parameters occasionally generate clouds of enhanced electron density at altitudes around 100 km. Due to their apparently irregular appearance in time and space, these clouds are termed sporadic E layers. They were discovered by the first ionosonde experiments in the first half of the 20th century, yet their origin and formation process stayed unclear for a long time. First global maps of sporadic E occurrence were produced during the International Geophysical Year in 1957 / 1958 (Leighton et al., 1962). The map displaying summer solstice conditions is shown in Figure 1.1. In 1960, Ratcliffe and Weekes (1960) proposed, *"It seems that the only type of force which could reasonably be expected to redistribute electrons into thin*

13

layers would be an electromagnetic one..." and *"Another mechanism by which extra elec-trons might be produced is through transport upward of some atmospheric constituent which carried stored energy, ready to be released in the production of free electrons. The most likely constituent of this kind appears to be negative ions. The precise mechanism for detaching the electrons has not been suggested, and it is difficult to see why it should be most efficient near 100 km.".* Just some months later, Whitehead (1960) described the mechanisms responsible for sporadic E formation at midlatitudes. His publication is still one of the elementary works on this subject. He suggested that sporadic E forma-tion is a complex process of interactions between ion concentration, the Earth's magnetic field and vertical shears in the lower thermospheric wind field. Subsequent studies (an overview is given by Whitehead (1989)) revealed that sporadic E formation is the result of interaction between wind shears, mainly produced by atmospheric tides, and long–lived metallic ions originating from meteors. This issue is addressed to in Chapter 2.

Sometimes sporadic E layers reach very high ionisation rates that radio signals travelling through one of these layers are considerably disturbed. Hence, the exact global radio communication and navigation is compromised. Scientific satellites flying in low–Earth
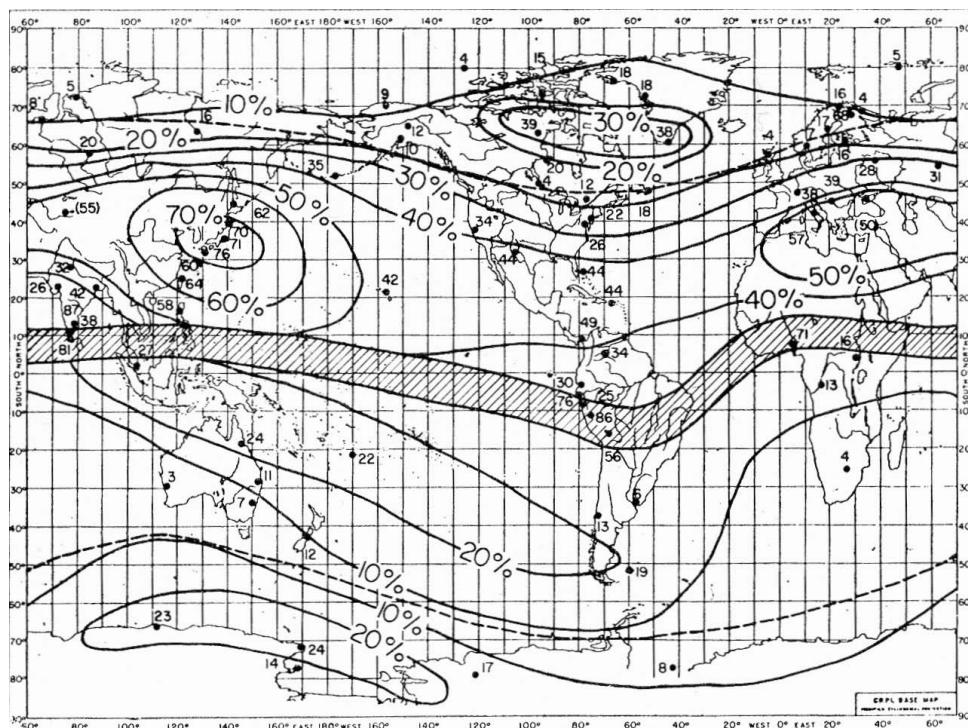
Figure 1.1: First global sporadic E map representing northern hemispheric summer sol-stice conditions based ionosonde measurements during the International Geophysical Year in 1957 / 1958. Adapted from (Leighton et al., 1962).

orbit receive the signals of the conversant GPS navigation satellites whenever they rise or set behind the Earth's limb. This modern method is called radio occultation technique. It is used to scan the atmosphere of the Earth by tracking GPS signals after they travelled through the atmosphere. The GPS signals are modified when propagating through the different atmospheric layers due to their refractive index.

These modifications are used to receive information on several atmospheric parameters between the surface and the orbit altitude of the scientific satellites. Based on radio occultation measurements, the atmosphere's properties and their behaviour is globally monitored covering a large altitude range. The profiles, registered by the radio occultation method, contain information on atmospheric parameters like temperature, pressure, moisture and electron density as well as on their global distribution and spatial and temporal variations.

The Earth's atmosphere is subject to permanent modifications on various time scales. In order to obtain knowledge on these variations, their causes and coupling processes between the layers, it is essential to monitor the atmosphere in a preferably high spatial and temporal resolution. Thus, it is informative and important to obtain a continuously regenerating global picture of these variables. Since ground based remote sensing or in–situ measurements of the atmosphere are mainly restricted to the continents of the northern hemisphere, the radio occultation technique is complementing these measurements. Recently, radio occultation profiles are also assimilated into several weather models. It has been shown that the weather forecast especially for the southern hemisphere was significantly improved (Anthes et al., 2008).

This thesis aims to receive a global picture of sporadic E occurrence and on its variations as well as on its dependence on other geophysical and solar–terrestrial processes. By analysing radio occultation profiles obtained from the three different satellite missions namely CHAMP[1], GRACE[2] and FORMOSAT–3 / COSMIC[3] (in the following referred to as COSMIC) it is possible for the first time to provide a comprehensive view on the global sporadic E occurrence and its variations in a high spatial resolution. Data from the three satellite missions are used for the investigations presented in this thesis. CHAMP already started to collect data in 2001. Its time series was complemented by GRACE and COSMIC measurements in 2006. This fact improved the data resolution significantly as discussed in Chapter 3. CHAMP, GRACE and COSMIC observations provide excellent data base of more than 2 million globally distributed radio occultation measurements during the years 2007 and 2008. Their radio occultation profiles are investigated in order

---

[1] CHAllenging Minisatellite Payload
[2] Gravity Recovery and Climate Experiment
[3] FORMOsa SATellite Mission–3 / Constellation Observing System for Meteorology, Ionosphere and Climate

to extract sporadic E signatures. Their position in latitude and longitude and altitude is obtained by additionally analysing the satellite's ephemerids.

The main tasks and questions addressed in this thesis correspond to sporadic E appearances and changes. During the last years, sporadic E was investigated from both radio occultation case studies (e.g. Hocke et al., 2001; Wickert et al., 2004; Wu et al., 2005) and ionosonde time series (Whitehead, 1989; Mathews, 1998; Haldoupis et al., 2006, and references therein). The obtained results raised further questions which have not been answered yet. A fundamental one is the question whether the radio occultation measurements and different detection algorithms (chapter 4) are an adequate procedure for sporadic E investigations. Subsequently, two validation procedures confirm the detection algorithms (chapter 5). Further it is known that sporadic E formation depends on the ion concentration, the Earth's magnetic field and the thermospheric wind field. But which parameter is the most influencing one? Do sporadic E layers really appear sporadically? Are there other variables that have to be taken into account? Or is it inversely justified to draw conclusions on the wind conditions from sporadic E appearance? The proposed wind shear theory for sporadic E formation works well in midlatitudes. Which process is responsible for sporadic E in equatorial or polar regions?
The global distribution of sporadic E layers in an unprecedented high spatial resolution is presented in Chapter 6. In Chapter 7, sporadic E formation and its global occurrence is investigated corresponding to characteristics of Earth's magnetic field, thermospheric tidal winds and meteors entering the atmosphere.

Chapter 2

The ionosphere as part of Earth's atmosphere

The Earth's atmosphere has a vertically layered structure and can be classified due to several attributes, for example temperature, chemical composition or plasma content (Figure 2.1). The most common classification results from the vertical temperature profile. The temperature is the most often concerned parameter of the atmosphere. Its altitude dependent behaviour divides the atmosphere into several layers.

The lowest one is the troposphere reaching from the Earth's surface up to about $10-15$ km. The tropospheric temperature decreases continuously with height due to adiabatic cooling up to the tropopause. In the stratosphere the temperature increases with height as a result of present ozone. The ozone molecules absorb solar UV (Ultra Violet) radiation and emit subsequently thermal radiation. At heights around 50 km the stratosphere gives way to the mesosphere. Due to the absence of ozone and no efficient thermal conduction in this layer the temperature decreases to its lowest atmospheric values of about $-80°$C in the mesopause region at around 80 km altitude. The mesopause marks the beginning of the thermosphere where the temperature gradient switches again. At heights above 200 km about 1000 K are reached due to the absorption of solar EUV (Extreme Ultra Violet) radiation.

Below $\sim$100 km the atmospheric gases are well mixed. Above, the composition varies with altitude depending on the molecular weight of the gas particles. The heavier ones such as nitrogen and molecular oxygen are present near 100 km and the low weight atomic oxygen is found above. Further information concerning the constitution of the lower atmosphere can be found in introductory meteorology books, e.g., Liljequist and Cehak (1984); Kraus (2004) and for the upper atmosphere by , e.g., Prölls (2004) or

17
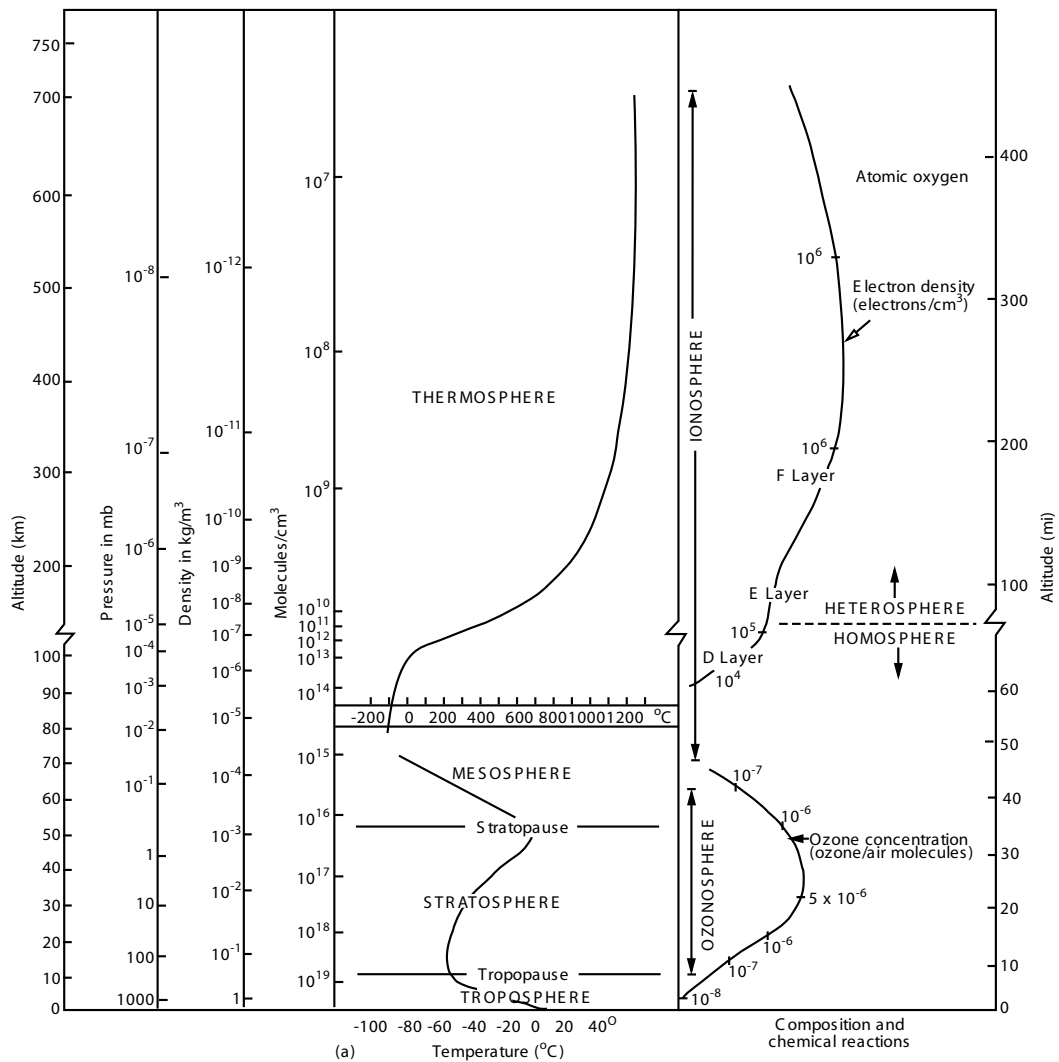
Figure 2.1: Classification of the Earth's atmosphere concerning several characteristics. Adapted from Rocken et al. (1997).

Craig (1965).

2.1   Composition of the ionosphere

In consequence of solar EUV radiation, the atmosphere above 60 km is weakly ionised and thus termed ionosphere. In contrast to other atmospheric layers, the ionosphere does not possess a sharp upper boundary. Rather it has a smooth transition into the interplanetary space. The ionospheric plasma is a mixture of thermal and gravitational bonded charge carriers. Due to the absorption of different wavelengths of solar radia-

tion in different heights, the distribution of ions and free electrons is not homogeneous. The ion composition is coupled to the neutral air composition. Solar radiation, acting on the different compositions of the atmosphere with height, leads to a weak ionisation. Recombination processes work against the increasing ionisation. Recombination is dependent on the mean free path and is therefore more efficient in the lower ionosphere. The interplay of both processes, ion production and recombination, acting on the height–dependent composition generate layers of different ionisation levels. Their main characteristics are described below and shortly summarised in Table 2.1.

D layer

The D layer is the innermost layer between $60 - 90$ km altitude. The ionisation is mainly controlled by the intensity of solar radiation. The ionisation rates show daily variations with increasing electron concentrations from sunrise to noon. Because of the relative high air density, the recombination rates are extremely high in the D region. For this reason the D layer diminishes almost completely after sunset.

E layer

The E layer is located between 90 and 170 km above Earth's surface. The maximum ionisation is usually reached at altitudes around 110 km with electron densities of $\sim 10^{11}$ m^{-3} during daytime. Due to the fact that the ionisation is mainly produced by photo–ionisation processes the electron density decreases after sunset to values around $5 \cdot 10^{10}$ m^{-3}. In the lower E region thin layers of strongly enhanced electron density are sometimes observed that are called sporadic E (E_s).

F layer

The maximum in electron density is usually found in the F layer which spans between 170 and about 1000 km altitude. It consists mainly of O^+ ions. During daytime the F layer is splitted into F_1 and F_2 layers with higher electron density values in the F_2 layer.

Plasmaphere

The plasmasphere, the outermost layer, affiliates at heights above 400 km and consists predominantly of H^+ ions with typical electron densities of 10^8 m^{-3}. The plasmasphere follows the shape of Earth's magnetic field. Its outer boundary is the plasmapause located in a distance between three and seven Earth's radii.

Layer	Altitude range	Prevalent ions	Typical electron density
Plasmasphere	$400\,km - 3\text{-}7$ Earth's radii	H^+	$\sim 10^8\,m^{-3}$
F layer	$170 - 1000\,km$	O^+	$\sim 10^{11} - 10^{12}\,m^{-3}$
E layer	$90 - 170\,km$	O_2^+, NO^+	$\sim 10^{11}\,m^{-3}$
D layer	$\leq 90\,km$	H_3O^+, NO_3^-	$\sim 10^8 - 10^{11}\,m^{-3}$

Table 2.1: Main properties of the ionospheric layers.

The electron density is not evenly distributed around the globe. Typical electron density values for the different ionospheric layers are given in Table 2.1. Generally, the electron content is on average higher at low latitudes compared to high latitudes. This is caused by the more intensive solar radiation in equatorial regions leading to higher ionisation rates.

Additionally, the ionosphere varies on different time scales that follow daily, seasonal and solar sunspot cycle (~ 11 years) changes. Daily variations in the ionosphere are a result of the $24 -$ hour rotation of the Earth around its axis. After sunrise, the electron density increases until its maximum is reached in the afternoon. Afterwards, the electron density decreases again. Seasonal variations result from the Earth's revolution around the sun. The relative position of the sun moves from one hemisphere to the other with the seasons. The ionisation level of the different ionospheric layers correspond to the altitude of the sun which reaches its highest values in hemispheric summer. The sunspot number corresponds to the solar activity level peaking approximately every 11 years. During periods of high solar activity, the ionisation density in all ionospheric layers is increased.

Besides the regular variations also irregular events occur in the ionosphere. They are a result of abnormal behaviour of the solar radiation or the atmosphere itself and cannot be predicted. Some examples of irregular ionospheric phenomena are shortly introduced in the following. For a more detailed description of the ionospheric constitution and its variations it is referred to (Kelley, 1989) and Prölls (2004).

Ionospheric storms are induced by enhanced solar particle and radiation influx. Coronal solar mass ejections are hitting the Earth's ionosphere producing strong density enhancements or depletions. As a result, the F region density can vary up to 100 % of positiv or negative deviation from undisturbed relations.

Sudden ionospheric disturbances are density enhancements due to solar EUV and X − ray radiation reaching down to the D region and having strong disturbing effects on the global radio communication.

Travelling ionospheric disturbances (TIDs) are wave–like structures in the ionospheric F region that are visible in the electron density. They are associated with thermospheric gravity waves and result from ion–neutral molecule collisions (Tsybulya and Jakowski,

2005). As mentioned above, thin sheets of extremely dense ionisation can sometimes form in the ionospheric E region. These sporadic E layers are focus of this thesis.

2.2 Characterisation of sporadic E layers

This section presents an overview on sporadic E characteristics and is followed by a description of the sporadic E formation process in midlatitudes.

2.2.1 Overview on sporadic E properties

Sporadic E layers are phenomena of the lower ionospheric E region. They appear mainly at daytime in midlatitudes in the summer hemisphere. In winter E_s rates are generally low. Sporadic E layers are considered as clouds of enhanced electron density compared to the background ionisation. They occur between 90 and 120 km altitude with a thickness of usually $0.5 - 5.0$ km and a horizontal extent of $10 - 1000$ km (Wu et al., 2005). They last from minutes to hours and are able to cause intense disturbances in radio wave propagation due to their strong vertical electron density gradients. The resulting disturbance in radio waves depends on the waves' transmission frequency.

In the past, observations came mostly from ground based remote sensing or from rare in–situ rocket measurements (Whitehead, 1989, and references therein). Ionosonde measurements allow to observe an E_s layer for a comparatively long time over a single location and to detect temporal variations of the layer. The main advantage of recent E_s observations by the satellite based GPS RO technique is the global data coverage with a relatively high spatial resolution.

Variations in E_s occurrence exist over broad temporal and spatial scales which may be related to different atmospheric and ionospheric processes. Pancheva et al. (2003) reported on significant correlations between midlatitude winds and E_s variations near 100 km altitude and attributed these variations to planetary wave and tidal modulations. Investigations using GPS phase measurements (e.g., Hocke et al., 2001; Wu et al., 2005) postulate that the strong E_s variability, found in summertime at mid and lower latitudes, appears to be correlated with deep convective and topographic induced processes in the troposphere. Fluctuations in long–term E_s observations have been investigated by Baggaley (1984) and Maksyutin et al. (2001). The authors did not find convincing arguments for the correlation of E_s appearance or strength with the course of solar cycle or solar activity. Recently, Haldoupis et al. (2007) used ionosonde observations to find conclusive evidence that both, sporadic E critical frequency, f_oE_s, and meteor influx observed from

westward wind

eastward wind

$\otimes$ **B**
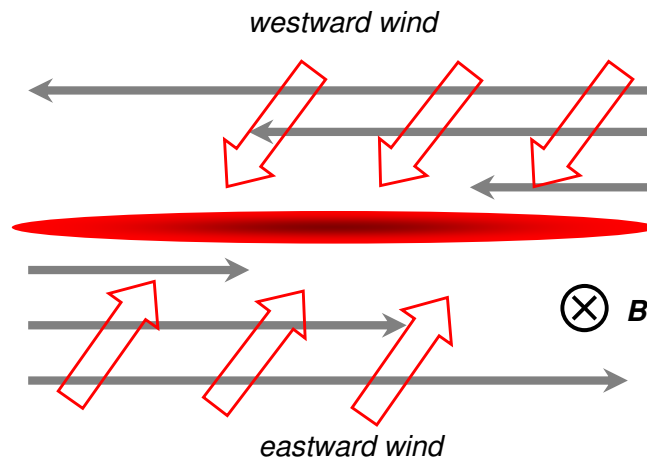
Figure 2.2: Illustration of the wind shear mechanism that is responsible for sporadic E formation. The process works well in midlatitudes at altitudes between 95 and 120 km. The orientation of the magnetic field $\vec{B}$ is indicated as well.

radar measurements follow a similar seasonal course. Namely, strong maxima occur in summer and minima are observed in early spring not confirming the formerly expected winter minima (e.g. Smith and Matsushita, 1962). The investigation of these properties is subject of this thesis and will be discussed in more detail in the Chapter 6 and 7.

2.2.2   Sporadic E formation

Our understanding of the E_s formation process in midlatitudes relies on the wind shear theory which was published by Whitehead (1961). For E_s generation, as illustrated in Figure 2.2, ionospheric plasma of large volume is swept together into a thin layer by the combined action of vertical wind shears, mainly produced by atmospheric tides, ion–neutral collision coupling and geomagnetic Lorentz forcing. Ions are transported efficiently by wind fields. Electrons follow them moving along the magnetic field lines to maintain charge neutrality. If there exists a height–dependent reversal of the zonal wind, the ions accumulate into dense sporadic E layers at the convergence nulls. The high recombination rates of the most abundant NO^+ and O_2^+ ions would effectively prevent the generation of high plasma densities. Therefore, the presence of slowly recombining metallic ions is assumed. The origin of metallic ions in the upper atmosphere is due to the evaporation of small micrometeors crossing Earth's orbit. Fe^+, Mg^+, Na^+, and Ca^+ are the metallic ions found most frequently by rocket measurements (Kopp, 1997; Williams et al., 2006). Although these rocket soundings refer to altitudes between 80 and

100 km, it seems reasonable to assume that generally similar conditions will hold in the 100 − 120 km range. Metallic ions have lifetimes of several days in the upper atmosphere (Plane, 2003) and are thus transported by atmospheric dynamics.

The velocity of the vertical plasma drift is estimated starting with the ion–momentum equation:

$$e\vec{v}_i \times \vec{B} - m_i\nu(\vec{v}_i \times \vec{u}_n) + e\vec{E} = 0, \tag{2.1}$$

with

e	elementary charge,
$\vec{v}_i = (v_1, v_2, v_3)$	ion velocity, v_1, v_2 are the horizontal, v_3 the vertical component,
$\vec{B}$	Earth's magnetic field,
m_i	ion mass,
ν	ion neutral collision frequency,
$\vec{u}_n = (U, V, W)$	neutral wind velocity, (zonal, meridional, vertical),
$\vec{E}$	electric field.

In the simplest form of Equation (2.1), neutral vertical winds and electric fields are neglected. The acceleration of the charged particles is assumed to be zero. The magnetic field lies in the southward and upward plane. For the northern hemisphere, it is defined by $\vec{B} = -B_0(\cos I, 0, \sin I)$, where I is the dip angle. With these simplifications and some small modifications we get in vectorial notation (cf. Mathews and Bekeny, 1979):

$$\begin{pmatrix} v_1 \\ v_2 \\ v_3 \end{pmatrix} \times \begin{pmatrix} \cos I \\ 0 \\ \sin I \end{pmatrix} + r \begin{pmatrix} v_1 - U \\ v_2 - V \\ v_3 \end{pmatrix} = 0, \tag{2.2}$$

with

$$r = \frac{\nu}{\omega} \qquad \text{and} \qquad \omega = \frac{eB_0}{m_i}. \tag{2.3}$$

The variable ω symbolises the ion cyclotron frequency and B_0 the total intensity of Earth's magnetic field. After solving the system of equations (2.2), the formula for estimating the vertical ion velocity is given by:

$$v_3 = \frac{V \cos I \sin I}{1 + r^2} + \frac{r\, U \cos I}{1 + r^2}. \tag{2.4}$$

The vertical ion velocity, v_3, represents the plasma drift since the electrons follow the ion's movement along the magnetic field lines to maintain charge neutrality. Consequently, sporadic E formation is possible where the vertical velocity of the ions is zero and the absolute value of its vertical gradient $\frac{dv_3}{dz}$ is large.

Equation (2.4) is the major formula to explain theoretically the sporadic E formation process in midlatitudes. It includes all influencing parameters, i.e. magnetic field, neutral winds, and ion properties. Therefore, its parameters are discussed in more detail in the following paragraph.

Discussion of Equation (2.4)

1. The wind shear process, as described above, works only in midlatitudes. In polar and equatorial regions, electric fields become too strong for effective E_s formation and cannot be neglected. In the polar cusp regions, E_s layers are often caused by particle precipitation (Nygren et al., 1984; Maehlum, 1962). In equatorial regions, electric field forces and the missing inclination of the magnetic main field prohibits E_s formation according to the described wind shear mechanism.

2. Above $\sim 125\,\mathrm{km}$ altitude the plasma drift is not collision–dominated and in Equation (2.4) the parameter r^2 becomes considerably larger than unity. One can infer that above 125 km the first term becomes too small and is thus negligible. At higher altitudes E_s formation is controlled by the shear of the meridional wind with northward wind above the convergence null and southward wind below (Haldoupis et al., 2006).
   Below approximately 125 km the ion collision frequency increases and the first term of Equation (2.4), including the shear of the zonal wind dominates the second one. A downward plasma drift induced by westward wind and an uplift caused by eastward wind leads to a formation of a layer of enhanced plasma density that accumulates in the region of convergence null (Figure 2.2). Note that the wind directions are given for the northern hemisphere. In the southern hemisphere the wind directions have to be inverse compared to the northern hemisphere to enable E_s formation. Below about 95 km, sporadic E layers start to deplete quickly because of a sharp increase of metallic ion recombination rates (Plane, 2003).

3. When substituting the parameter r in Equation (2.4) by $\frac{\nu}{\omega}$, the resulting equation now includes the term $\omega \cos I$ which is directly proportional to the horizontal component of Earth's magnetic field. This component is calculated by $B_{hori} = B_0 \cos I$, where B_0 is also existent in the ω variable (cf. Equation (2.3)). Thus, it is expected that sporadic E formation is directly correlated with the horizontal component of Earth's magnetic field and that E_s layers appear preferably in regions with large values of the magnetic's field horizontal intensity.

The wind shear theory gives a conclusive explanation for E_s formation in midlatitudes. But some features known from observations still remain unclear. For example the annual cycle of E_s in midlatitudes cannot be explained by the wind shear theory only. The missing of E_s along the magnetic equator and its very low occurrence rates in the region of the South Atlantic Anomaly (cf. Chapter 7.1) needs further discussion. Possible explanations of these phenomena are given in the Chapters 6 and 7.

2.3 The origin of metallic ions in the upper atmosphere

Additional to air components, metallic ions are found in the E region that have significantly longer lifetimes than the ionised air molecules. The metallic ions, mostly Mg^+, Fe^+, Na^+, and Ca^+, have their origin in meteoroids. Whenever such a piece of rock enters Earth's atmosphere, it is decelerated due to the increase of the atmospheric density and thus friction. During its way through the atmosphere, the initial kinetic energy is mainly transferred to thermal energy. Therefore, the meteoroid starts to glow and evaporates in most cases completely in the upper atmosphere. Big meteoroids become visible as bright shining meteors.

The meteor influx underlies daily and seasonal variations as well, which are depicted in Figure 2.3. These plots are based on meteor radar (MR) measurements performed at Collm observatory, Germany ($51.3°N$, $13.0°E$) in 2006 and 2007. They show the annual and the monthly mean diurnal cycle of meteoric influx. During daytime, maximum meteor rates appear in the early morning hours. With progression of time, the hourly rates decrease significantly to the minimum in the late afternoon. The total number of detected meteors also shows a diurnal cycle. The reason for that is of astronomic origin. Depending on the viewing angle in direction of Earth's revolution around the sun, more or less meteoroids are able to enter the atmosphere, respectively. In the morning we are on the front side of Earth's movement around the sun and thus all meteors enter Earth's atmosphere. In the afternoon, we are on the backside where only high speed (fast than the velocity of Earth's revolution around the sun) meteors can enter. Consequently, the meteors appearing in the afternoon are slower than the ones which appear during morning hours and penetrate deeper into the atmosphere. Thus, they evaporate at lower altitudes.

Additionally, an annual cycle in the daily meteor rates is detected (upper panel of Figure 2.3). The minimum in daily meteor counts occurs in spring. It is followed by a steep increase to the maximum in June, July, and August. In order to explain the observed annual variation, it is necessary to know that nearly all meteoroids are relicts originating
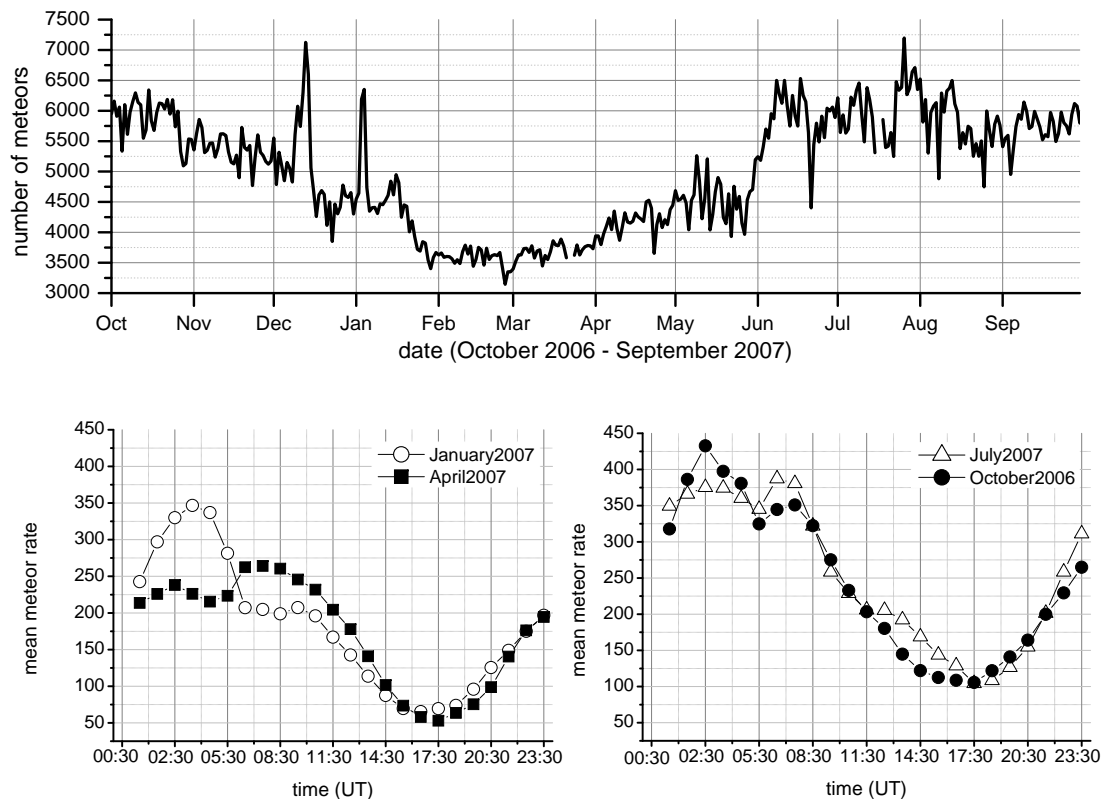
Figure 2.3: Daily meteor count rates (upper panel) detected with the meteor radar Collm, Germany (51.3°N, 13.0°E) between October 2006 and September 2007. The lower panel contains information on the monthly mean diurnal cycle of meteor influx for four different months (adapted from Arras et al. (2009)).

from the asteroid belt. Consequently, they move along the ecliptic. At northern mid-latitudes, the ecliptic plane rises between 10° to 15° in northern winter and up to 60° in northern summer. Naturally, more meteors enter the atmosphere during the summer months. The annual cycle reverses in the southern hemisphere accordingly with maximum values appearing during February and March. The minimum is reached during late northern summer and autumn.

The annual cycle is interfered by intensive events with sometimes extremely high daily meteor rates. During those days, the Earth passes through cometary trails. The comets loose a lot of material on their orbit around the sun. The ablated dust leads to the so called meteor showers on Earth. Two of them can be identified in the upper panel of Figure 2.3; the Geminids appear in December 2006 and the Quadrantids in January 2007. More information on the physics of meteors can be found in Rendtel (1991); Mc Kinley (1961) and (Plane, 2003, and references therein).

When a meteoroid evaporates in the atmosphere, metallic components are ablated from its surface. Metallic atoms have low ionisation potentials leading to easy ion formation by charge transfer or photo–ionisation. In the thermosphere, these metallic ions have lifetimes of at least several days (Plane, 2003). As a result, they are exposed to neutral atmospheric dynamic processes. They are transported by winds and experience $\vec{v} \times \vec{B}$ forces, where $\vec{v}$ represents the neutral wind and $\vec{B}$ Earth's magnetic field. The most important dynamical features are the solar tides at mesospheric and thermospheric altitudes.

2.4 A short overview on solar tides

Solar tides are global scale oscillations that are present in the upper atmospheric wind, density, temperature, and pressure fields. In contrast to the gravitational–forced ocean tides, the tidal waves in the upper atmosphere are thermally excited by solar radiation. The atmospheric tides with the largest amplitudes have periods of 8, 12 and 24 hours that are multiples or equal of a solar day. The alternation between heating of the atmosphere during daytime and cooling at night induces a temperature oscillation with a diurnal and a semidiurnal component. Solar radiation involving heating of tropospheric water vapour is the origin of the diurnal component in the lower atmosphere. The source region of the semidiurnal tide is located at higher altitudes. The tidal wave is excited by absorption of solar UV radiation of the stratospheric ozone at altitudes between 30 and 60 km.
Solar thermal tidal fields can be expressed, in general, in the form (Forbes et al., 2006):

$$A_{m,s} \cos(m\,\Omega\,t + s\,\lambda - \phi_{m,s}), \tag{2.5}$$

where $A_{m,s}$ is the amplitude, m denotes a subharmonic of a solar day, $\Omega = 2\,\pi\,day^{-1}$ represents the rotation rate of Earth, t is the time (days), s symbolises the zonal wave number, λ is the longitude, and $\phi_{m,s}$ the phase that is defined as the time of maximum at zero longitude. Sun–synchronous components of the tidal waves are referred to as migrating tides. In that special case the zonal wave number equals m. All other components are referred to as nonmigrating tides.
The initial temperature and corresponding pressure oscillations yield to periodic airflow – the tidal winds. The oscillations propagate in horizontal and vertical direction. Hence, they are considered as tidal waves with amplitudes and phases. Near their source region, the amplitudes are small. But the amplitudes increase exponentially with height caused by the density decrease in the atmosphere.

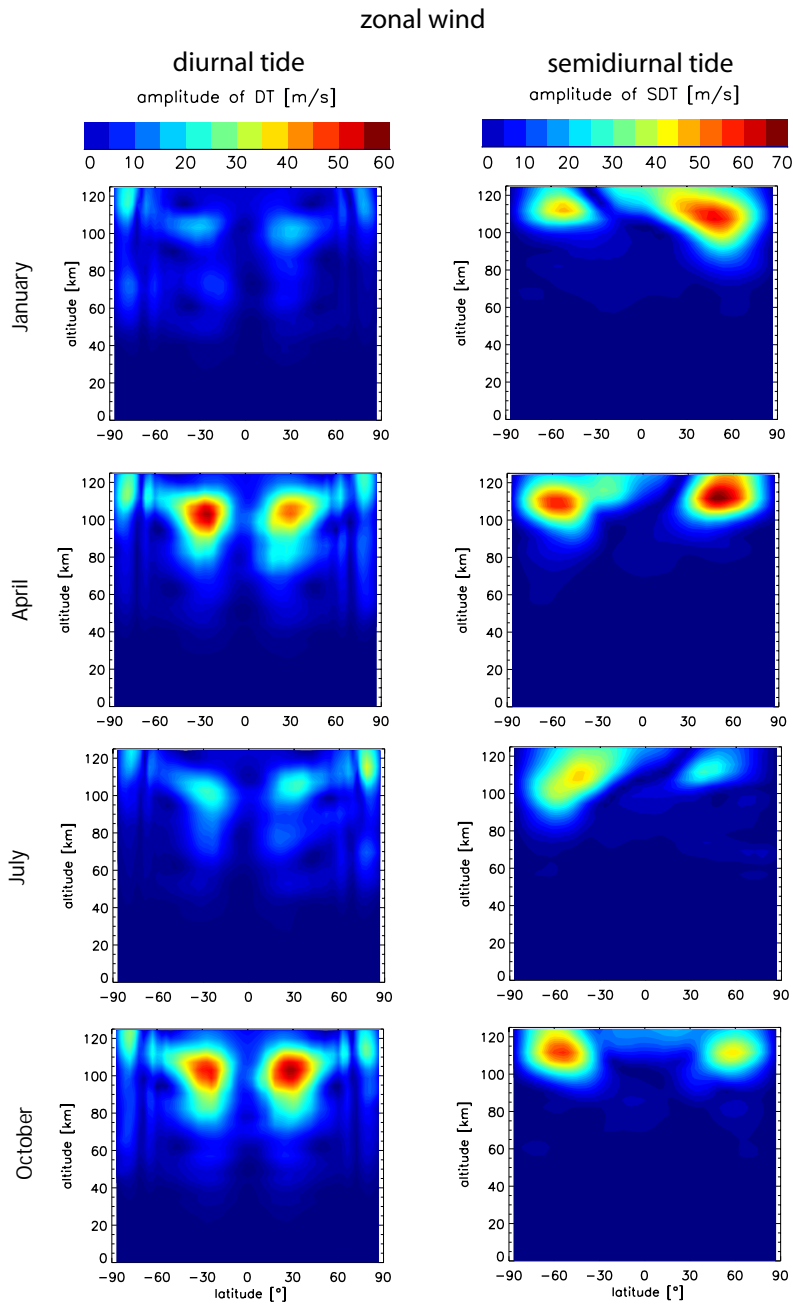**Figure 2.4:** Latitude – altitude cross–sections of the amplitudes of the zonal component of the semidiurnal (right panels) and the diurnal (left panels) tide for January (upper-most row), April (second row), July (third row) and October (lowermost row). Note the different scaling for DT and SDT amplitudes. Data were taken from the GSWM model (http://www.hao.ucar.edu/modeling/gswm/gswm.html).

Tidal structures are dominating the wind field in the upper mesosphere and lower thermosphere region. In order to obtain an impression on the global distribution of tidal amplitudes, model outputs from the GSWM (Global Scale Wave Model) of the diurnal and the semidiurnal tide (Hagan and Forbes, 2002, 2003) are displayed in Figure 2.4. In these plots, the focus is set on the zonal amplitudes of the semidiurnal (SDT) on the right hand side and the diurnal tide (DT) on the left hand side. Both components are present throughout the year with some seasonal enhancements at distinct latitudes. The amplitudes of the SDT are generally larger than the DT ones. SDT maxima appear during summer and winter solstices in midlatitudes at altitudes between 100 and 125 km. During equinoxes, the amplitudes reduce by 50 % compared to the solstice months. Yet the SDT is stronger in the vernal hemisphere. The DT appears mostly conjugated with similar behaviour in both hemispheres. The DT reaches its maximum also during the solstices but in lower midlatitudes at about 100 km altitude. During equinox seasons, the amplitudes of DT are significantly smaller than during the solstices.

Caused by upward wave propagation, the tidal structure appears in the alternation of the wind speed as well as in its direction with height, the so–called wind shear. The metallic ions are transported with the tidal wind. The tidal shears assist to compress these ions into thin but compact sporadic E layers.

2.5 Ground based remote sensing of the ionosphere

Already in the 19th century, Gauss and Kelvin postulated a conducting layer in the upper atmosphere from observations of variations in Earth's magnetic field. At the beginning of the 20th century, Marconi performed the first transmission of radio signals over the Atlantic Ocean. This phenomenon was attributed to radio wave reflections on free electrons by Heaviside and Lodge in 1902. However, only in 1924, Appleton did prove the existence of the ionosphere with systematic radio wave experiments.

The significant influence of the ionosphere on radio wave propagation has a large impact on our modern way of life. The ionosphere may has adjuvant influences and can act as a disturbing source as well. For example, the ionosphere enables worldwide radio communication in the frequency range between 2 and 20 MHz. Waves, as transmitted from the Earth's surface are reflected at the ionospheric E or F region and are received at locations far behind the horizon and sometimes all around the globe. This phenomenon is exploited by radio and TV stations.

Yet the ionosphere, and especially irregularities in its electron density distribution, can disturb radio signals intensively. For example trans–ionospheric signals from satellites are

principally affected by the ionosphere. In opposite cases, the radio waves are degraded so extensively that a correct reception is not possible at all. One prominent problem is that ionospheric disturbances considerably decrease the reliability of satellite communication and navigation systems. Corrections have to be applied to these systems. Therefore, it is important to know as much as possible about the ionosphere and its variations, its temporal behaviour and spatial distribution.

Basically, there are two different types of ionospheric observation methods; in–situ measurements and remote sensing techniques. Since the ionosphere is difficult to access for in–situ observations, the most available data sets are based on remote sensing techniques as ionosondes, incoherent scatter radars and GPS signal observations.

An example for in–situ measurements are rocket soundings which allow among others to determine the chemical composition of the lower ionosphere (e.g., Grebowsky and Bilitza, 2000, and references therein). Another example is the Langmuir probe onboard the CHAMP satellite. The main parameter determined with this probe is the electron density at orbit altitude.

In the following, the most common remote sensing techniques are shortly introduced. The basis for all of these observations is the modification of the transmitted radio waves due to the ionospheric electron density distribution. The main observable is the atmospheric/ionospheric refraction which is closely related to the electron density.

2.5.1 Ionosondes

Since about 1940, ionosondes have been established as the most common ionospheric observation technique. This method allows to determine vertical electron density profiles from the ground to altitudes of about $200 - 400$ km.

The ionosonde broadcasts a sweep of frequencies, usually between 0.1 and 30 MHz. Parallel to the increase of the submitted frequency each wave is refracted less by the ionosation level and penetrates further into the ionosphere before it is reflected. By recording the time needed for each single frequency to be reflected, it is possible to determine the height as well as the electron density at the reflection point. The frequency where a wave just penetrates the ionisation layer is known as the critical frequency, f_c, of the layer. All transmitted frequencies above f_c will further penetrate into the ionosphere without being reflected. The critical frequency is related to the electron density by the following equation, deduced from the law of refraction by Eccles (1912):

$$f_c = \frac{1}{2\pi} \sqrt{\frac{e^2 N_e}{m_e \varepsilon_0}} \qquad (2.6)$$

with

e	elementary charge	$= 1.602 \cdot 10^{-19}$ C,
N_e	electron density,	
m_e	electron mass	$= 9.109 \cdot 10^{-31}$ kg,
ε_0	permittivity	$= 8.854 \cdot 10^{-12}$ AsV^{-1}m^{-1}.

One problem arises by estimating the real or geometric height, h, of the reflection point. Due to Snell's law, waves travel slower in a charged medium than in vacuum. Thus, the signal is delayed. The height of the reflection point is simply calculated via:

$$h' = c_0 \frac{\Delta t}{2}. \tag{2.7}$$

The received virtual height, h', does not equal the geometric height of the respective layer but it is larger than the real height. The term Δt stands for the signals travel time and c_0 for the speed of light in vacuum. The difference between the geometric and the virtual height is governed by the amount of ionisation traversed by the wave. The amount of ionisation is related to the the refractive index, n. In order to reconstruct a real–height profile of electron concentration, the integral over the refractive index along the ray path must be solved using:

$$h' = \int n \, dh. \tag{2.8}$$

The refractive index profile is calculated directly from ionosonde soundings.
Ionosonde ground stations do not give any information about the electron distribution above the F region peak value. Therefore, ionosondes are also used onboard satellites. These so–called top–side soundings give useful information about the electron concentration above the F layer. A detailed mathematical description of the inversion process used to determine electron density profiles from ionosonde measurements is given by Huang and Reinisch (1996).

2.5.2 Incoherent scatter radars

Developed in the 1960's, the Incoherent Scatter Radar (ISR) technique established quickly as a further ground based remote sensing method for ionospheric parameters. Besides the determination of electron density profiles the ISR technique allows to receive profiles of the plasma velocity and electron temperature as well as ion temperature. The measurement principle is based on radio wave scattering on free electrons. The system consists of a transmitting antenna and one large or several smaller receiving antennas. Pulsed VHF (Very High Frequency) or UHF (Ultra High Frequency) waves with
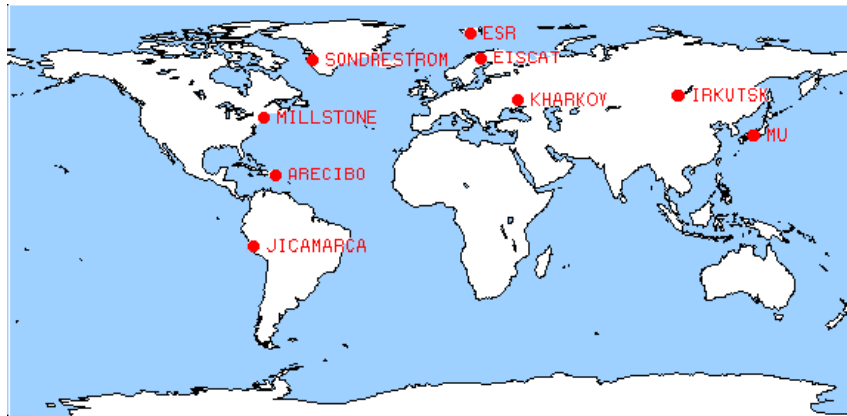
Figure 2.5: Location of the operational Incoherent Scatter Radars. Taken from http://www.haystack.mit.edu/atm/mho/iswg/index.html.

frequencies higher than the critical frequency of the F layer are transmitted through the ionosphere. Measurements of the signal power of the backscattered wave allow to determine vertical electron density profiles with a high altitude resolution. The Doppler shift of the received signal is a measure for the line–of–sight plasma velocity (Evans, 1969). Additionally, ion and electron temperatures are estimated from the backscattered wave spectrum. The operation of an ISR is very sophisticated and costly. Thus, ISR instruments are not used for continuous ionospheric monitoring like ionosondes. They are operated exclusively during campaigns. Currently only nine ISR instrument are in use world–wide. Their location is displayed in Figure 2.5.

2.5.3 High Frequency – Sounder

Monitoring of polar ionospheric conditions with ground based observations is done by SuperDARN (Super Dual Auroral Radar Network). In 1983, the network was started to build up with the installation of the first HF (High Frequency) radar at Goose Bay, Labrador, Canada. It developed into a system of twelve operational radars in the northern polar hemisphere and seven radars in the southern polar hemisphere[1]. Their locations and measurement ranges are displayed in Figure 2.6. The radars are operating at frequencies between 8 and 22 MHz. Each radar measures the line–of–sight plasma velocity at 75 ranges along 16 beam directions covering an area of about 3500 km in range and $56°$ in azimuth[2]. The measurements from the single stations are used to generate high–latitude plasma convection maps with a temporal resolution of two minutes. The plasma

---

[1]http://superdarn.jhuapl.edu/

[2]http://superdarn.gi.alaska.edu/
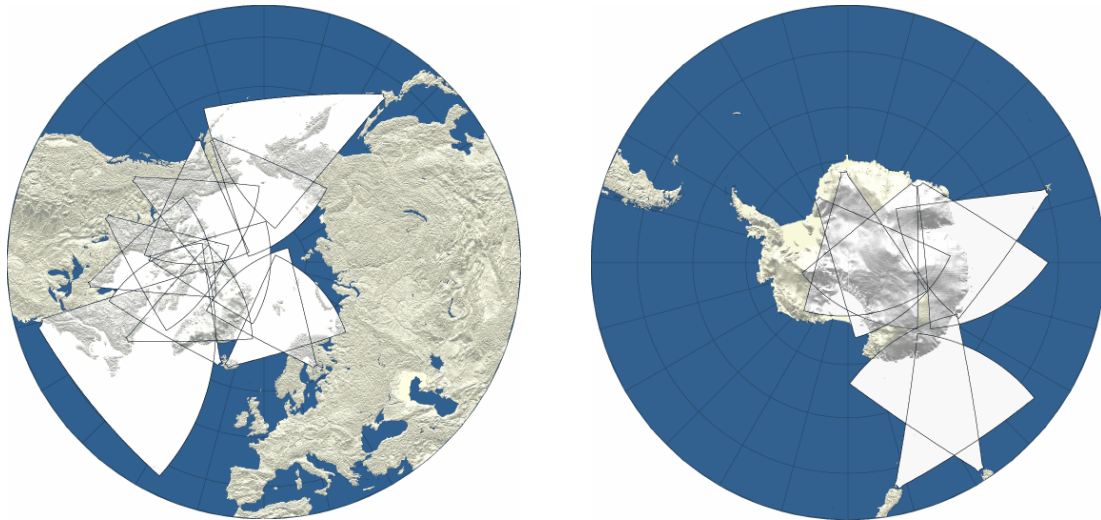
Figure 2.6: Locations and measurement ranges of the SuperDARN radars in the northern (left) and southern hemisphere (right). Taken from http://superdarn.jhuapl.edu.

convection maps are used to investigate the structure and dynamics of global plasma convection. Additionally, the measurements are used for gravity wave studies and to investigate the plasma structure and ionospheric irregularities (Greenwald et al., 1995).

2.5.4 Global maps of total electron content

A large number of ground based GPS receivers is distributed on Earth's surface. A large fraction of them belongs to the IGS (International GNSS Service for Geodynamics) that provides highly accurate data products, e.g., precise GPS satellite orbits[3]. The dispersive nature of ionosphere leads to phase differences between the received GPS L_1 and L_2 signals. The difference is directly related to the Total Electron Content (TEC) through which the GPS signals have travelled through. The observed slant TEC is projected to vertical TEC values by applying a mapping function under the assumption of a single layer ionosphere (e.g. Jakowski, 1996). The available data sets enable the construction of regional or global TEC maps. Since 1995 $2-$dimensional vertical TEC maps are produced routinely by DLR Neustrelitz[4]. These maps are used to identify and monitor disturbances at ionospheric F layer altitudes as well as travelling ionospheric disturbances (Borries et al., 2009).

---

[3]http://igscb.jpl.nasa.gov
[4]http://www.kn.nz.dlr.de/ionos/maps.html
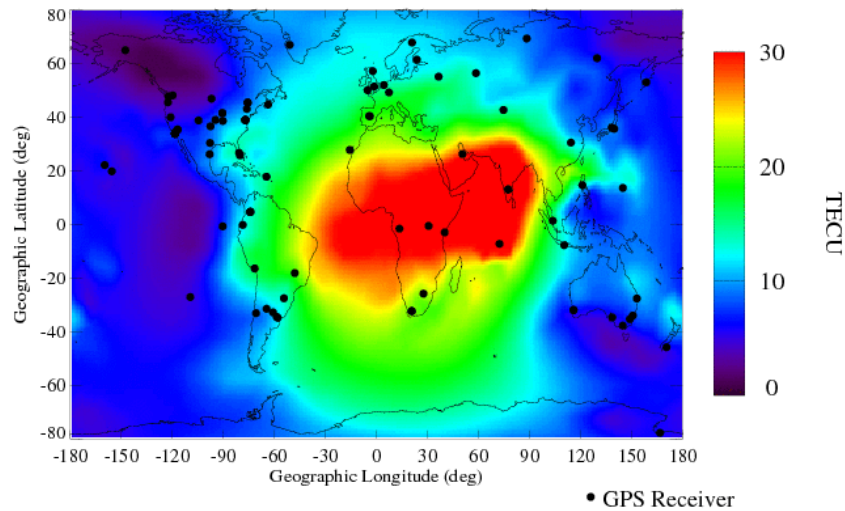
Figure 2.7: Real–time global TEC map provided from JPL at 22 March 2010 12:40 UTC. Taken from http://iono.jpl.nasa.gov/latest_rti_global.html.

Ionosondes and ISR systems provide time series, often in a high temporal resolution, of ionospheric data at one location or area, respectively. In order to receive a global picture on ionospheric conditions, these techniques are only of limited applicability.

Recently, GPS based observations from space as e.g. the radio occultation method can fill in this blank. They enable global data coverage but do not provide data in a sufficient time resolution to create time series over a small area. Therefore, the use of all these methods is justified.

Chapter 3

Atmospheric sounding with the GPS radio occultation technique

In 1904, Pannekoek published the principle of an occultation for the first time. He proposed to use stellar occultations to explore planetary atmospheres (Pannekoek, 1904). This concept was adopted and improved by a group at Stanford University in 1962. Together with JPL (Jet Propulsion Laboratory) they developed a two–way coherent Doppler tracking system which was chosen by NASA (National Aeronautics and Space Administration) for installation on Mariner 3 and 4 space crafts to probe the Martian ionosphere and atmosphere (Yunck et al., 2000; Fjeldbo and Eshleman, 1968). In the following years, the technique was used to study the atmosphere of Venus. The measurements were performed on the Mariner 5 space probe (Fjeldbo et al., 1971). It also served to explore the atmospheres of the outer planets of the solar system, their ring systems, and the atmospheres of several moons by the Voyager 1 and 2 missions (Lindal et al., 1983; Tyler, 1987; Lindal, 1988). In the late 1980's, this technique was proposed to apply to Earth's atmosphere using the GPS signals (e.g., Yunck et al., 1988) and was demonstrated for the first time by the GPS / MET experiment in 1995 (Ware et al., 1996).

Apart from that activities concerning radio occultations were initiated in the former Soviet Union. For example, Gurvich and Krasilnikova (1990) published the idea to use Soviet weather satellites for GPS radio occultation measurements and to use these measurements to improve weather forecasts.

35

3.1   Atmospheric observations based on GPS

A constellation of LEO (Low–Earth Orbiting) satellites is required to observe Earth's atmo-
sphere by the radio occultation technique in a sufficient spatial and temporal resolution.
Navigation satellites act as transmitters of the occultation signals. Primarily, their function
is the continuous transmission of radio waves which are used for public and military nav-
igation and positioning with global coverage. The scientific application of these signals
can be considered as a valuable spin–off product. These navigation satellite constella-
tions are also known as GNSS, an acronym for Global Navigation Satellite System. The
most established one is the U.S. American system called NAVSTAR–Global Positioning
System (GPS). It will be described in more detail in the following section. Other navigation
satellite systems are in use or in development by several countries. The formerly Soviet
and now Russian GLONASS was built up in 1982 but fell in disrepair since the collapse of
the Soviet Union. Russia intends to restore the system with the help of India until 2012.
As of April 2010, GLONASS consists of 23 satellites. 21 of them are in operational use.[1].
China indicated to expand its regional BEIDOU system to a global program named COM-
PASS (Hofmann-Wellenhof et al., 2008). The system was started to built up in 2007 with
the launch of the first COMPASS satellite. In spring 2010 already three satellites are in
orbit. Also India owns a regional navigation satellite system (IRNSS – Indian Regional
Navigation Satellite System) which will consist of seven satellites scheduled for comple-
tion in 2012[2].

The European Union and the European Space Agency (ESA) started to built up the
Galileo global navigation satellite system. This constellation will consist of 30 spacecraft
orbiting in three planes with an inclination of $56°$ at an altitude of $23\,260\,$km. Currently,
two test satellites are in orbit. The first one, GIOVE – A (Galileo In – Orbit Validation Ele-
ment), was launched on 28 December 2005 from the Baikonur cosmodrome. The satellite
started to emit first Galileo navigation signals on 12 January 2006 (Hofmann-Wellenhof
et al., 2008). The second test satellite, GIOVE – B, was brought into orbit on 26 April 2008.
During the test phase, the Galileo ground based infrastructure and spacecraft payload
are validated. After successful performance of the first tests, four operational satellites
will be launched using two separate launchers for further validation experiments in 2011.
These satellites will be used to validate the Galileo system as a whole. Afterwards, the
deployment phase will start, where all fully operational Galileo satellites will be brought
into orbit and the ground infrastructure will be completed. The full deployment is currently

---

[1]http://www.glonass-ianc.rsa.ru
[2]http://www.oosa.unvienna.org/pdf/icg/2008/expert/2-3.pdf
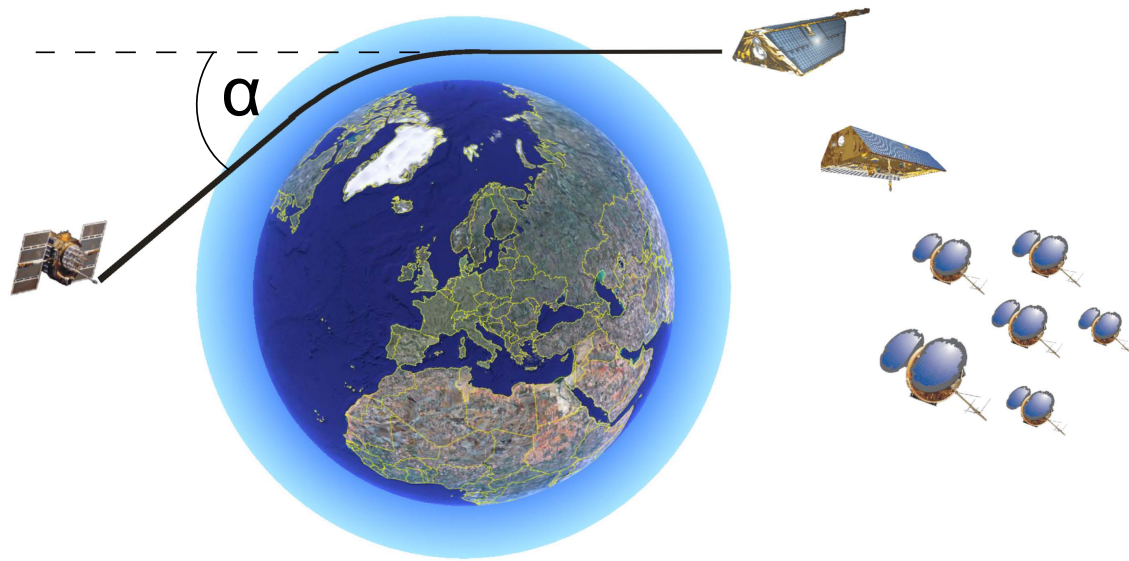
Figure 3.1: GPS Radio occultation principle. The LEO satellites CHAMP (top), GRACE (middle) and the COSMIC constellation (bottom) observe a rising or setting GPS satellite (left) behind Earth's limb. The key observable is the bending angle, α, which is induced by ionospheric and neutral atmospheric refraction.

scheduled for 2014[3].

3.1.1 GPS radio occultation principle

The GPS radio occultation technique relies on accurate dual frequency measurements by a LEO satellite. Due to their low altitude, LEO spacecraft orbit the Earth faster than GPS satellites which fly in significantly higher altitudes. During its revolution, the fast moving LEO spacecraft tracks the GPS satellite rising or setting behind Earth's limb. The GPS signals are received by the LEO satellite after they have travelled through the atmosphere. Hence, they contain information on the atmosphere.

One single occultation takes about five minutes. Thereby, the atmosphere is scanned in two sections. In the upper part, stretching between LEO altitude and around $50-60$ km the atmosphere is scanned with a sampling rate of 1 Hz refering to an altitude resolution of about 2 km. From about 130 km altitude down to the surface, the atmosphere is additionally scanned with a sampling rate of 50 Hz corresponding to a height resolution of approximately 50 m. On their way through the atmosphere, the GPS waves are modified

---

[3]http://ec.europa.eu/transport/galileo
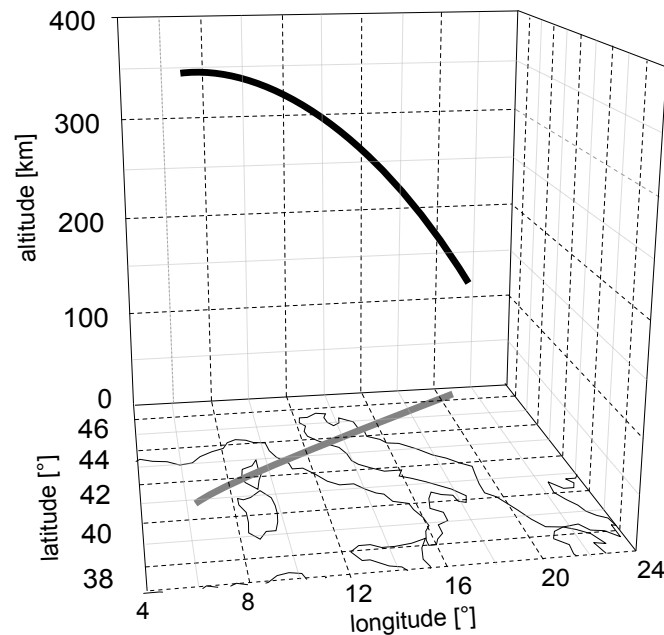
Figure 3.2: Location of the tangent point (black) and its ground projection (grey) during an ionospheric occultation observed by CHAMP over Corsica, Italy on 20 June 2004 at 03:15 UTC.

due to the refractive index of the atmosphere. Atmospheric induced path changes are detected by associating GPS measurements with velocities and positions in order to correct for the relative motion of GPS and LEO satellites. Bending angles of the rays are available after a calibration process (Hajj et al., 2002). Using the Abel integral transform, a series of bending angles are converted into vertical profiles of the refractive index which can be interpreted as electron density in the ionosphere and temperature, pressure and humidity profiles in the troposphere and stratosphere. The RO method reveals one main advantage compared to ground based measurements. With only one instrument profiles of different variables can be obtained covering the whole globe. Therefore, it is possible to receive a global picture of these atmospheric parameters. Adversely, it is not possible to record time series of these parameters over a distinct small area. Quarterly and monthly mean values on a global scale can easily be obtained allowing seasonal trend analysis of several atmospheric characteristics over a large altitude range. The high vertical resolution of the profiles is very profitable in the troposphere where temperature and water vapour content may change significantly in between small spatial sectors due to weather changes along weather fronts.

Radio occultation signals often experience strong scintillations in the Signal–to–Noise Ratio (SNR) and phase measurements on both GPS frequencies. In most applications, especially for the determination of tropospheric parameters, these oscillations are measurement noise. Occultation measurements including scintillations often do not pass quality checks successfully and yield no accurate profiles. If the oscillations appear at ionospheric altitudes, they are mostly caused by sporadic E layers and therefore contain valuable information concerning their occurrence, physical properties and variabilities.

As visible in Figure 3.2, the occultation profiles are not necessarily arranged vertically in the atmosphere. The black line in Figure 3.2 indicates the course of the tangent point during a CHAMP occultation on June 2004 at 03:15 UTC which took place over the Mediterranean area. The tangent point is defined as the point where the radius vector of the Earth is perpendicular to the GPS ray.

Although the GPS signals propagate a long way through the atmosphere, the majority of atmospheric bending occurs within a horizontal interval of $200 - 300$ km (Kursinski et al., 1997). The surrounding areas do not necessarily have an effect on the received signals. Only structures of lesser extent than the spread of the tangent points will cause significant errors in the refractive index profiles.

3.1.2 GPS constellation

The Navigation Satellite Timing and Ranging Global Positioning System (NAVSTAR–GPS or shortly GPS) is a space based radio navigation system installed and operated by the United States for civilian and military purposes. It is divided into a space and a control segment. The control segment consists of a master control station located in Colorado Springs, several monitor stations, and ground antennas. The main tasks of the control segment are the tracking of the satellites for orbit and clock determinations and predictions and for time synchronisation of the GPS satellites. The first satellite was launched on 22 February 1978 as one of 11 initial spacecraft. In the following year, the complete constellation was installed. As of 2010, the GPS space segment consists of 31 actively broadcasting satellites orbiting Earth in 20 200 km altitude with a period of 12 sidereal hours (Misra and Enge, 2001). A specific satellite constellation is therefore repeated every sidereal day. Accordingly, a shift of two minutes in universal time (UT) occurs daily due to the difference between the solar and the sidereal day. The satellites are arranged in six orbital planes that are inclined by about $55°$ with respect to Earth's equator. The planes are equally separated by $60°$ on the equator. The spacecraft's orbits are nearly circular. At least four satellites are unevenly distributed on each plane. This specific constellation allows simultaneous observation of at least 4 GPS satellites
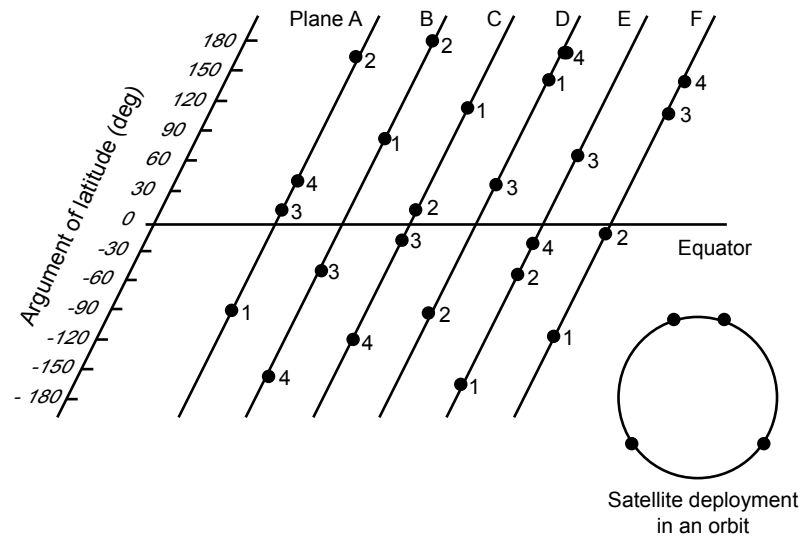
Figure 3.3: Visualisation of the GPS satellite orbit deployment. Four GPS satellites are installed on each of the six orbital planes. Adapted from Misra and Enge (2001).

from any place on Earth. This fact allows for very precise navigation and positioning. GPS was primarily intended for military use, but it becomes more and more important in the civil sector. It is used, e.g., in seafaring and aviation, in navigation systems for cars, for outdoor orientation, and for surveying and mapping.

GPS signals

The heart of each GPS spacecraft is an ultra stable oscillator which is an ensemble of rubidium and caesium atomic clocks. They are used to generate two coherent carrier frequencies in the $L-$Band:

$$f_{L1} = \quad 1.575\,\text{GHz} \qquad (\lambda_1 = 190\,\text{mm})$$
$$f_{L2} = \quad 1.227\,\text{GHz} \qquad (\lambda_2 = 244\,\text{mm}),$$

where $\lambda_{1,2}$ denotes the corresponding wavelength.

The aim of GPS measurements is to determine the distance between transmitter and receiver. Therefore, phases of the incoming signals are compared with a reference signal generated by the receiver. In order to avoid measurement ambiguities for the transfer of orbit data as well as to confine the availability of GPS data, the signals are phase modulated with Pseudo Random Noise codes (PRN).

The GPS signal is composed of a fundamental oscillation and overlapping codes. A short description of the complete signal is given in the following:

- The *carrier signal* consists of a sinusoidal signal with the frequencies f_{L1} or f_{L2}.

- The *ranging code* is a unique sequence assigned to each satellite. These sequences are called PRN. The codes have special properties that avoid interference of the signals transmitted by different GPS satellites.
  Each satellite transmits two different codes; a satellite related Coarse / Aquisition (C / A) code and an encrypted precision (P–) code. Only the L_1 signal is modulated with the freely accessible C / A code, while the P–code is overlapping on both the L_1 and L_2 signals. The P–code allows for precise range measurements and has therefore special relevance in military navigation. The P–code is extremely long and consists of $2.35 \cdot 10^{14}$ chips. Each GPS satellite generates a specific segment of this code. As a result, the received signal can be associated to the individual satellite.

- Additionally the satellites transmit *broadcast messages* containing navigation data. These messages include information on the GPS satellite's position and velocity, its health status, and its clock bias parameters.

The freely available L_1 signal is received with a distinctly higher intensity compared to the L_2 signal because the L_2 wave is encoded and has to be reconstructed via a cross–correlation method to get at least an evaluable signal. Detrimentally, the reconstruction is only possible at the expense of signal power. As a result, the SNR of L_2 is always significantly lower than the SNR of L_1.

Since 2006, three additional GPS signals have been broadcasted by the GPS satellites in order to improve the civilian navigation globally. For military encryption, a new M–code is added on the existing L_1 and L_2 waves. The third new signal is named L2C. It is a modification of the former L_2 signal with different but freely accessible codes (Kaplan and Hegarty, 2006). With the launch of the first GPS satellite of a new generation (IIR–M), since March 2009 a supplemental L_5 signal is transmitted at a frequency of 1.176 GHz. Compared to the GPS L_1 and L_2 signals, L_5 has an improved signal structure, higher transmitting power (about 3 dB), wider bandwidth, and longer spreading codes. It is intended to refine GPS accuracy for landing aircrafts and to perform other safety–of–life applications (Hofmann-Wellenhof et al., 2008).

3.1.3   Signal modification

GPS signals are affected by the transited medium. The major part of its way, the signal travels in vacuum. At heights of about 1 000 km above Earth's surface, the signals enter the ionosphere. The ionosphere as well as the neutral atmosphere below have strong impacts on the propagating GPS waves. The main effects provoking disturbances on the GPS RO signals are summarised in the following (Hajj et al., 2002; Wu et al., 2005).

Bending

Atmospheric refraction causes bending of GPS signals on their way through the atmosphere which induces an excess phase delay. The bending effect is proportional to water vapour content, air density, and electron density. Contributions from neutral components are generally small at heights above 60 km where the bending is only dependent on the electron density. Atmospheric bending is the main effect for the radio occultation technique. Due to bending, the LEO spacecraft still receives GPS signals after if the satellite has already set behind Earth's limb.

Focussing / Defocussing

Vertical gradients in the bending angle provoke radio waves to diverge or to converge leading to a decrease or increase, respectively, of signal intensity at the receiving antenna. This effect increases gradually with pressure at tangent height in the stratosphere and troposphere. Sharply layered structures near the boundary layer cause strong fluctuations in the GPS signal. In the ionosphere, thin layers of enhanced electron density, such as sporadic E, induce strong oscillations in the SNR due to the focussing / defocussing effect.

Diffraction

The deflexion of electromagnetic waves caused by an obstacle is called diffraction. If diffraction occurs, the wave is able to propagate after passing the obstacle where new waves are excited along a wave front following Huygens principle. Very similar effects are observed for electromagnetic waves travelling through a medium of abrupt refractivity changes. For GPS occultation signals, diffraction occurs when the waves travel through atmospheric irregularities modifying the refractive index of the atmosphere significantly within a short ray path. This effect is for instance caused by sharp vertical humidity gradients in the lower troposphere.

Multipath

Multipath refers to a phenomenon where the signal reaches the receiving antenna via two or more possible paths. Causes of multipath include ionospheric reflection and refraction by very sharp layers or reflection from water surfaces or terrestrial objects. In the atmosphere / ionosphere very sharp and thin layers consisting of water vapour / enhanced electron density may cause differential bending of the GPS rays. As a result, the transmitted signal reaches the LEO on different paths.

3.2 GPS radio occultation satellite missions

The aim of this section is to give an overview over the past and still ongoing GPS RO missions with focus on the CHAMP, GRACE and COSMIC missions. These low–Earth orbiting satellites are moving in a near polar orbit at altitudes between 350 and 800 km. Table 3.2 gives an overview of the characteristics of the CHAMP, GRACE and COSMIC missions at the end of the section.

The pilot satellite project for sounding Earth's atmosphere was Microlab − 1 with the accompanying GPS / MET experiment. The satellite was launched from the Air Force Base Vandenberg, California on 5 April 1995 into an altitude of 740 km (Rocken et al., 1997). Its payload consisted of an optical lightning imaging sensor and of the first generation of GPS receivers (Turbo Rogue) developed by JPL. The experiment proceeded successfully. For the first time, global observations of temperature, pressure, air density, and electron density were received using the GPS radio occultation technique. The analysis of GPS / MET RO data was focussed on times when encryption of the GPS signals was disabled. In these periods, approximately 150 RO measurements were perfromed per day. During the two years lifetime, several thousands of RO measurements were recorded and analysed (Hajj et al., 2002, further information: www.cosmic.ucar.edu/gpsmet).

Four years later, the first Danish satellite was launched on 23 February 1999. The Ørsted satellite is still in orbit today and operates enduringly. The main purpose of the Ørsted mission is to provide a precise global map of Earth's magnetic field. Its measurements are used to improve existing magnetic field models and to determine its changes. Additionally, the satellite carries a Turbo Rogue GPS receiver used for atmospheric sounding (Larsen et al., 1999).

Onboard the Argentinean scientific satellite SAC–C (Satellite de Aplicaciones Cientificas–C), the next generation of a GPS receiver (BlackJack) also developed by JPL was installed. The mission started with the launch of SAC–C on 21 November 2000. It was

initially planned four years but is currently (April 2010) still ongoing. The science objectives of this mission are broadly diversified. One objective is the observation of Earth's magnetic field and its variations and to measure high energetic radiation in Earth's environment. An other objective is the provision of multispectral images of Earth to monitor conditions and changes of the terrestrial and marine biosphere. Co–located measurements from two different RO missions (CHAMP and SAC–C) were compared for the first time (Hajj et al., 2004). It was shown that the temperature profiles collected from the two different satellites are consistent to 0.10 K on average with a standard deviation of 0.86 K between 5 and 15 km above sea level.

CHAMP

The German CHAMP mission was realised after a project proposed by GFZ Potsdam (Reigber, 1995). The spacecraft was constructed in cooperation with DLR (Deutsches Zentrum für Luft - und Raumfahrt) and several space industry companies under the lead of GFZ. Finally, CHAMP was successfully launched on 15 July 2000 from the Russian cosmodrome base Plesetzk to an initial altitude of 454 km (Reigber et al., 2003; Wickert et al., 2001, 2004).

The main scientific objectives of the CHAMP mission are the observation of spatial and temporal variation of Earth's gravity field and to determine the strength of Earth's magnetic field and its variations as well as the realisation of GPS radio occultations for global atmospheric sounding. An overview of scientific results of the CHAMP mission is given by Reigber et al. (2003, 2005). The GPS radio occultation experiment was started on 11 February 2001. Since that time CHAMP provided continuously about 250 RO measurements per day. Initially, the mission duration was planned for five years. After four orbit uplifts, the mission is expected to end in mid 2010. The elapsed and also predicted orbit scenario of the CHAMP satellite (green line) is given in Figure 3.4. The RO experiment ended in October 2008 due to problems of the GPS receiver. Nevertheless, the nearly eight year lasting time series of CHAMP records is unique. It allows for initial trend analysis of atmospheric and other geophysical parameters.

GRACE

Almost two years after the CHAMP satellite, the two identical satellites of the GRACE mission were launched on 17 March 2002. The twin satellites are co–orbiting Earth with a distance of 220 km between them. Just like CHAMP they have a near polar inclination

and the initial altitude amounts around 500 km. The major scientific objective is to identify changes in Earth's gravity field. Therefore, instantaneous changes in the distance between the satellites are used to make extremely precise gravitational measurements. Areas of slightly stronger gravity will affect the lead satellite first pulling it away from the trailing satellite. A STAR accelerometer is used for precise measurements of the non–gravitational accelerations acting on the satellites. This allows to distinguish gravity influences from those of air drag. With this method, scientists intend to observe large–scale water movements on and also beneath the surface as well as ocean currents. Additionally, changes in ice sheets, glaciers on Greenland and Antarctica, and variation of the global sea level can be tracked (Ward et al., 2004).

The second science objective of the GRACE mission is the performance of global atmospheric soundings using GPS radio occultations. The operational radio occultation experiment started in early 2006 and GRACE currently provides about 200 globally distributed measurements per day. The mission was initially planned for five years but was extended for at least seven further years. The decay scenario for the GRACE orbit altitude
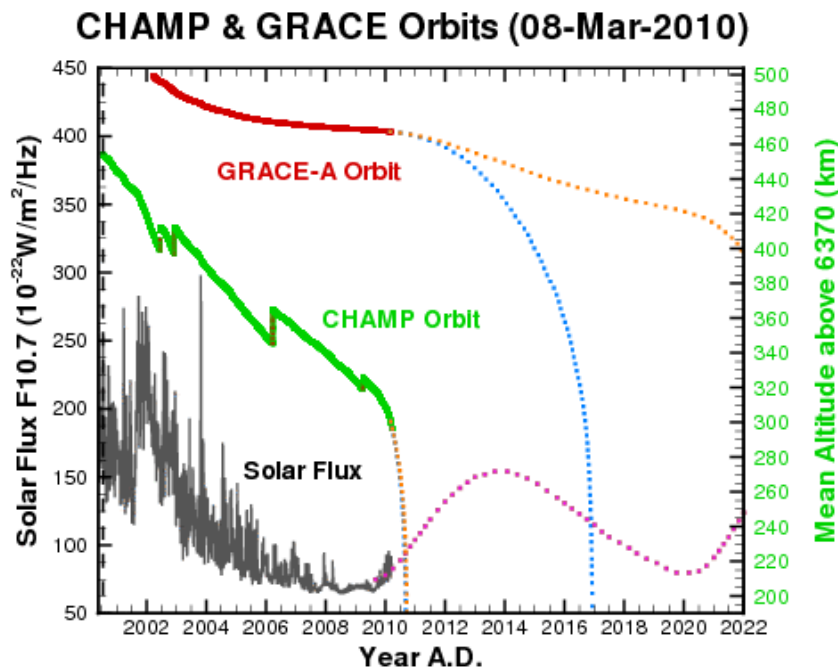
Figure 3.4: Orbit altitude (solid lines) and predictions (dotted) for the CHAMP (green) and GRACE (red) satellites (as of March 2010). Blue dots represent the expected orbit altitude for high solar activity during the next years whereas the dotted orange line indicates the expected orbit altitude for less intense solar activity. Measurements (grey) and predictions (violet) of the solar flux are added in the lower part of the figure. By courtesy of F. − H. Massmann, GFZ.
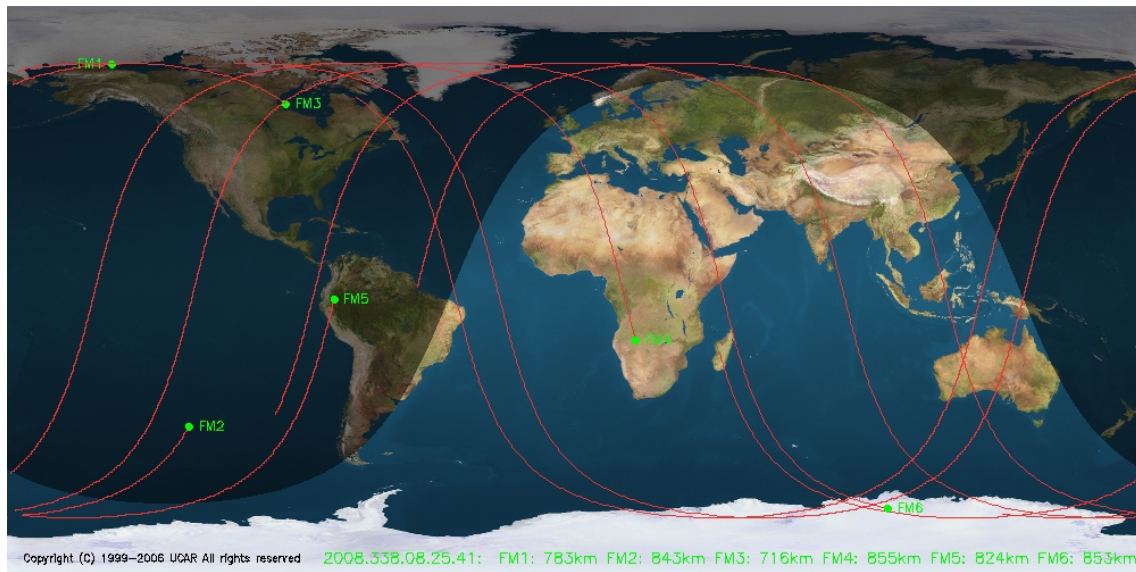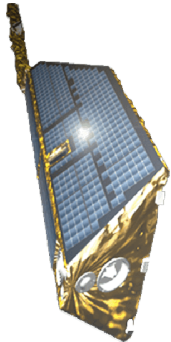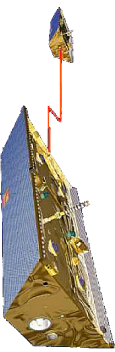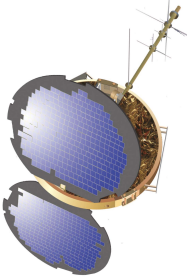
Figure 3.5: Ground tracks representing one orbit ($\sim$ 100 minutes) of COSMIC satellites in space on 5 December 2008. From http://www.cosmic.ucar.edu.

(red line) is displayed in Figure 3.4.

FORMOSAT–3 / COSMIC

FORMOSAT–3 / COSMIC stands for FORMOsa SATellite Mission–3 / Constellation Observing System for Meteorology, Ionosphere and Climate (Rocken et al., 2000; Anthes et al., 2008). It is a joint U.S. American and Taiwanese mission consisting of six mini satellites. They were launched on 15 April 2006. After the launch, the spacecraft were flying very close to each other at an initial altitude of 512 km. During their first 17 months in orbit the satellites were slowly moved to their final orbit configuration at $\sim$ 800 km altitude. The satellites are not equally distributed over the globe. The orbital planes have only a separation of 30° in longitude. In Figure 3.5 an example of ground tracks for the six spacecraft representing one orbit (time period of approximately 100 minutes) are mapped.

The final configuration and the use of a new GPS receiver, named IGOR (Integrated GPS Occultation Receiver), allows to record more than 2 000 rising and setting radio occultations per day. One major objective concerning the RO experiment is the provision of the profiles in near–real time and to supply them into global weather models to improve weather forecasts. In addition the COSMIC spacecraft provide about ten times more RO measurements compared to CHAMP and GRACE. The fact leads to a much larger data

Mission	CHAMP	GRACE	COSMIC
Number of spacecraft	1	2	6
Leadership	GFZ Germany	NASA / DLR USA / Germany	UCAR / NSPO USA / Taiwan
Launch	15 July 2000	17 March 2002	15 April 2006
Expected lifetime	2000 – 2010	2002 – 2015	2006 – 2011
Science application	gravity field magnetic field atmospheric sounding	gravity field atmospheric sounding	atmospheric sounding ionospheric investigations
Uppermost orbit altitude	454 km	500 km	800 km
Inclination	87.3°	89°	72°
Dimensions width height length	trapezoidal 1.6 m 0.75 m 8.33 m incl. 4.04 m boom	trapezoidal 1.92 m 0.72 m 3.123 m	cylindrical diameter: 1.03 m 0.16 m
Initial weight	525 kg	487 kg per satellite	70 kg per satellite
Further information	www.gfz-potsdam.de/champ	www.csr.utexas.edu/grace/	www.cosmic.ucar.edu

base for ionospheric investigations.

Additionally, an ionospheric photometer is arranged onboard the COSMIC satellites to monitor the intensity of far UV emissions that result from recombinations of oxygen ions with free electrons. The results can be converted into electron densities.

A nadir pointing tri–band beacon completes the satellites scientific payload. Based on its measurements the total electron content (TEC) between satellite and a network of dedicated ground stations can be estimated.

3.3 Atmospheric characteristics from radio occultations

The GPS radio occultation technique relies on accurate measurements of the amplitudes and phases of the L_1 and L_2 signals received by dedicated GPS flight receivers onboard LEO satellites. The RO technique is described in detail for example by Kursinski et al. (1996, 1997); Hajj et al. (2002) and Wickert (2002). The detected time series of phase modulations of the received signals are accompanied by a variation in frequency because the time derivation of the phase is directly proportional to the frequency shift. This classical Doppler effect is dependent on the relative movement of GPS and LEO satellites and on the atmospheric conditions along the wave paths. To extract the atmospheric part, the fraction from the relative satellite motion is subtracted from the total shift. The residual only contains information on Earth's atmosphere. Its impact on the propagating wave is characterised by the total bending angle α and the impact parameter a that is defined as the distance of the closest approach for the straight line path. The bending angle is calculated geometrically from the satellite positions under the assumption of local spherical symmetry. In the following the bending angle profiles are calculated for each GPS frequency. Since the ionosphere is a dispersive medium, the L_1 and L_2 signal travel along slightly different paths and have slightly different bending angles. This effect can be corrected by a linear combination of both bending angles. Subsequently, the bending angle profile $\alpha(a)$ of the neutral atmosphere is inverted to a refractive index profile by an Abel transformation given by (e.g., Tricomi, 1985):

$$n(a) = \int_{a}^{\infty} \frac{1}{\sqrt{a'^2 - a^2}} \frac{d \ln \alpha}{da'} da'. \tag{3.1}$$

3.3.1 Refraction of radio waves in the atmosphere

The influence of the ionosphere as well as the neutral atmosphere below 50 km changes the velocity and direction of the propagating radio signals. This phenomenon is referred

to as refraction. The variation of propagation speed changes the signals transit time, which is the basic observable from GPS.

The refractive index, n, of the atmosphere is defined as the ratio of propagation speed in vacuum, c_0, and the speed in a medium c_1:

$$n = \frac{c_0}{c_1} \qquad \text{with} \quad c_0 = 299\,792\,985 \text{ m/s.} \qquad (3.2)$$

The refractive index is often substituted by the refractivity N. Both parameters are connected via:

$$N = (n - 1) \cdot 10^6. \qquad (3.3)$$

The refractive index as well as the refractivity are dependent on atmospheric parameters like electron density in the ionosphere and temperature and water vapour in the neutral atmosphere. The refractive index changes due to the concentration or behaviour of mentioned parameters. This results in the bending of the signal path (Snell's law) leading to a curved ray path longer than the geometrical straight–line path. But following the Fermat principle, the signal's transit time is even shorter than that for a straight–line path.

Atmospheric parameters, namely temperature, pressure, moisture and electron density are connected to the refractivity via Equation (3.4) (Kursinski, 1997):

$$N = \underbrace{77.6\frac{p}{T}}_{\text{dry term}} + \underbrace{3.73 \cdot 10^5 \frac{p_w}{T^2}}_{\text{moist term}} - \underbrace{40.3 \cdot 10^6 \frac{N_e}{f^2}}_{\text{ionospheric term}} + \underbrace{1.4w.}_{\text{scattering term}} \qquad (3.4)$$

In this equation p denotes the atmospheric pressure, T is the temperature, p_w is the water vapour partial pressure, N_e symbolises the electron density, f the GPS L_1 or L_2 frequency, respectively and w represents the liquid water content. The numerical constants in each term result from complex calculations implementing the electromagnetic properties of the propagating wave. The entire procedure is described in detail by Budden (1985).

The dry term in Equation (3.4) is only dominant below about 60 km and characterises the polarisability of the molecules in the atmosphere. It is directly proportional to the molecular number density (Kursinski, 1997). Since relevant moisture values are only found in the lower part of the troposphere, the moist term is only significant near the surface. The moist term characterises the interaction of the propagating wave with permanent dipoles of water molecules. In contrast, the ionospheric term dominates at altitudes above ~ 60 km. It is proportional to the number of free electrons. The last term in Equation (3.4) is called scattering term and it is due to liquid water droplets in the atmosphere.

Accordingly, profiles of the various variables in the ionosphere and neutral atmosphere can be calculated from Equation (3.4).

3.3.2 Neutral atmospheric profiling

Below 50 km altitude, the ionospheric term and the scattering term of Equation (3.4) are neglected. The local refractivity is accurately converted into local mass density of dry air where no water vapour is present. Under "dry" conditions, Equation (3.4) reduces to $N = 77.6 \frac{p}{T}$. Assuming hydrostatic equilibrium, the local mass density is integrated downward in order to obtain the local pressure p:

$$p(h) = \int\limits_{h}^{\infty} g\rho \, dh, \qquad (3.5)$$

where ρ denotes the atmospheric mass density, *dh* the incremental vertical distance and *g* is the acceleration due to gravity. Applying the ideal gas law, the local temperature and density can also be derived by:

$$\rho = \frac{NM_a}{77.6R_g} = \frac{pM_a}{TR_g}, \qquad (3.6)$$

where M_a is the molecular mass of dry air and R_g denotes the universal gas constant. A complication to apply of this method arises below the tropopause due to the presence of water vapour. Here, the second term of Equation (3.4) has also to be taken into account. In combination with the ideal gas law it can be rearranged to solve for the partial pressure of water vapour:

$$p_w = \frac{NT^2 - 77.6pT}{3.73 \cdot 10^5}. \qquad (3.7)$$

The solution of this equation requires the temperature which can be derived from a climatology, weather model output, or in best case coinciding measurements. To separate the dry and the wet part from the measured refractivity profile, an iterative algorithm is applied leading to a pressure and humidity profile.

The neutral atmospheric RO profiles are used for a broad spectrum of scientific investigations. Especially the nearly eight year long time series of CHAMP measurements allows for initial trend analysis of atmospheric conditions. Information on the global behaviour of the tropopause are extracted from the temperature profiles (Schmidt et al., 2004, 2008). It was found that the tropopause raises with up to 7 m per year on global average with

large variations in different latitude regions. The temperature profiles are also used to estimate the wave activity especially of gravity waves in the upper troposphere and lower stratosphere (de la Torre et al., 2006; Namboothiri et al., 2008). The "wet" profiles are used to monitor the water vapour content in the lower and middle troposphere (Heise et al., 2006).

Several international weather forecast centers started to assimilate operationally data from the COSMIC satellites shortly after their launch in 2006. The centers tested the impact of refractivity profiles provided by COSMIC radio occultations on the numerical weather prediction. It was found that they positively influence forecasts of tropical cyclones and the prediction of upper tropospheric temperatures and winds (Anthes et al., 2008; Poli et al., 2009).

3.3.3 Ionospheric profiling

At ionospheric altitudes, only the third term in Equation (3.4) is relevant and therefore the refractive index only depends on the electron density. Between the LEO spacecraft orbit altitude and about $80 - 100$ km above surface, the radio occultation data are usually tracked with 1 Hz resolution. Abel inversion through bending angle or TEC profiles is the most common method to receive electron density profiles. The algorithm is described in detail by Schreiner et al. (1999) and Hajj and Romans (1998). Jakowski et al. (2002) developed a procedure for ionospheric profiling which is based on a tomographic approach using a spherically layered shell structure. Consequently, a global picture of the vertical electron density distribution and accompanying irregularities is received.

Initial retrieval of electron density profiles used at GFZ

In the following, the algorithm currently used at GFZ for inverting ionospheric radio occultation data into electron density profiles is described. The inversion is performed with the onion peeling algorithm (Syndergaard, 2007; Lei et al., 2007). A scheme of the geometry is displayed in Figure 3.6.

Calibrated TEC values taken from UCAR preprocessed profiles are used to calculate the electron density. Calibrated TEC means that it refers only to the portion of TEC below LEO altitude. Its derivation under the assumption of straight–line propagation of GPS signals in the ionosphere is described in detail by Schreiner et al. (1999). Assuming additional spherical symmetry of the electron density, now TEC varies only with altitude, the calibrated TEC, $\widetilde{TEC}$, is related to electron density as a function of the radius from Earth's
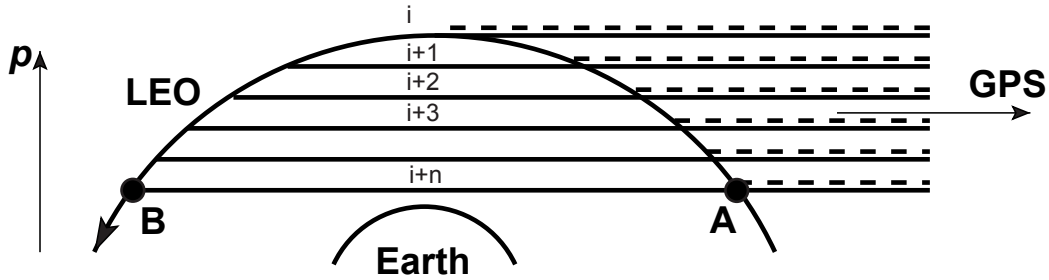
Figure 3.6: Visualisation of the onion peeling method (modified version of a figure taken from Syndergaard (2007)). Calibrated TEC values, $\widetilde{TEC}$, are calculated by $\widetilde{TEC}$ = solid − dashed lines.

center via:

$$\widetilde{TEC}(a_i) = \sum_{k=1}^{m} 2 \int_{a_{i+k-1}}^{a_{i+k}} \frac{r\, N_e(r)}{\sqrt{r^2 - a^2}} dr, \tag{3.8}$$

where N_e symbolises the electron density, r the radius from Earth's center and a denotes the distance from Earth's center to the tangent point altitude. In the following Equation (3.8) is inverted to Equation (3.9) in order to obtain an electron density profile. Assuming that the electron density varies linearly with altitude between discrete altitude levels the integrals in Equation (3.9) can be solved analytically using:

$$N_e(p_i) = c_{i,0}^{-1} \left(\frac{\widetilde{TEC}(a_i)}{a_i} - \sum_{k=1}^{m} c_{i,k} N_e(a_{i,k}) \right), \tag{3.9}$$

where the dimensionless coefficient $c_{i,k}, k = 0, 1, ..., m$ parameterises the altitude levels. The parameter m stands for the total number of levels. The electron density profile is now reconstructed recursively starting at LEO altitude. The initial electron density value is estimated by linear regression of the square of calibrated TEC as a function of $\sqrt{a_{orbit} - a}$ for the uppermost levels. The slope of straight line gives the electron density at orbit altitude (Syndergaard, 2007).

One example for an electron density profile is given in Figure 3.7. It was reconstructed from a CHAMP radio occultation measurement on 20 June 2004. The profile is calculated with the method described above and indicated with a red line. It is compared to profiles calculated with established algorithms at UCAR (green) and DLR Neustrelitz (blue). In principle an overall agreement is found between the different profiles. Only the course on
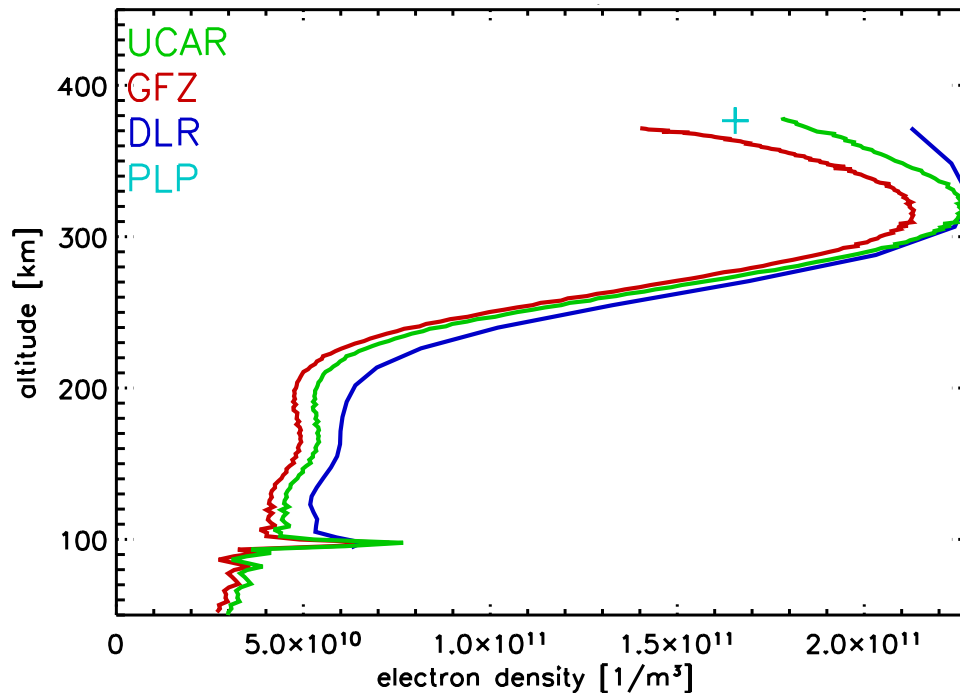
Figure 3.7: Electron density profiles calculated by GFZ (red), UCAR (green) and DLR Neustrelitz (blue). The occultation data were recorded by CHAMP on 20 June 2004 at 47°N, 52°E at 00:12 UTC. The light blue cross represents the electron density measured by the Langmuir probe onboard the satellite. At about 100 km altitude a sporadic E layer is present in all profiles.

the top–side of the F layer shows large differences between the three methods. In about 100 km altitude a sporadic E layer is present that is well reflected by the GFZ and UCAR profiles. The sharp electron density gradient is not clearly reproduced by the DLR profile.

3.4   Global distribution of radio occultation measurements

CHAMP, GRACE and COSMIC provide in total about 2 500 radio occultation profiles per day. The profiles are used to monitor the atmosphere all over the globe and to receive information on its spatial and temporal behaviour in a very high vertical and also horizontal resolution. In the following, an overview is given on the global and temporal resolution of radio occultation measurements performed by CHAMP, GRACE and the COSMIC constellation.

For the following investigations, 2 479 829 RO measurements were analysed whereof major contributions came from COSMIC satellites. Table 3.2 gives an overview on the avail-

Satellite	Total number of RO	Mean daily RO
CHAMP	541 527	~250
GRACE	141 987	~200
COSMIC	1 796 315	~2 200
Total	2 479 829	

Table 3.2: Total number of RO measurements from CHAMP, GRACE and COSMIC collected between 2001 and 2008.

able RO profiles from the different satellites. CHAMP allocates a continuous nearly 8 year long time series of data, which allows for initial trend analysis in ionospheric and also neutral atmospheric parameters. Yet the quarterly global data coverage is sparse. Since the start of COSMIC radio occultations the number of daily RO profiles increased significantly. Although COSMIC data are available only since August 2006, its number of profiles exceeds the sum of GRACE and CHAMP profiles by a factor of three. Figure 3.8 shows the number of daily RO measurements performed by the different satellites. CHAMP, indicated with green colour, provides the longest time series starting in 2001 and lasting until October 2008. CHAMP allocated about 250 profiles per day. This quantity remained constant during the period of operation. In the beginning of 2006, the daily measurements
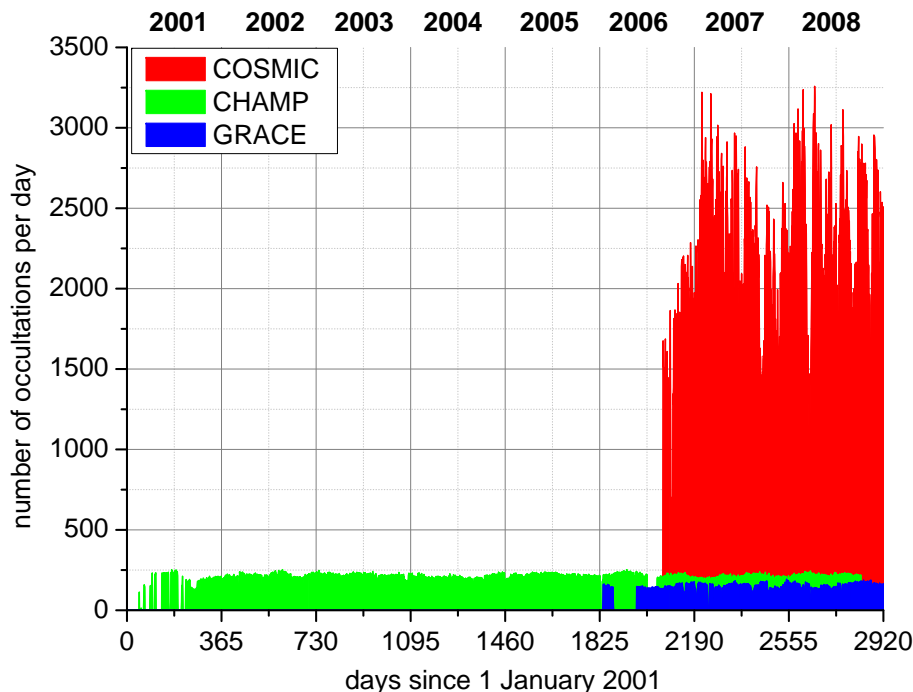

Figure 3.8: Time series of available daily CHAMP (green), GRACE (blue) and COSMIC (red) phase delay data sets (level 1b) between January 2001 and December 2008.
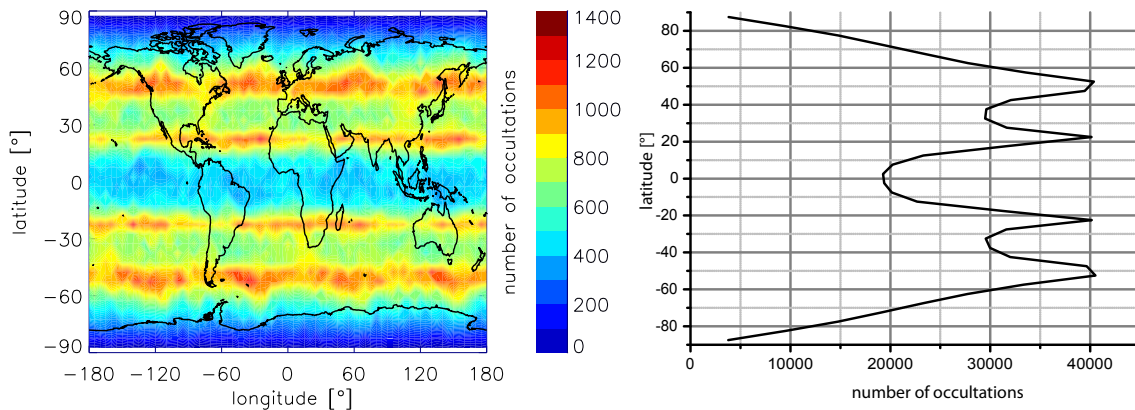
Figure 3.9: Left: Global distribution of radio occultation measurements performed by CHAMP, GRACE and COSMIC in 2008 summed up in a $5° \times 5°$ grid. Right: Latitude dependent number of RO profiles in a $5°$ resolution.

are supplemented by GRACE (blue), providing about 200 daily RO profiles. The COSMIC measurements (red) complete the applied data set. Since their activation the satellites provide on average more than 2 200 profiles per day. As visible in Figure 3.8, the daily occultation number is not constant. Especially the daily number of COSMIC occultations varies considerably. This is due to technical problems with some of the satellites[4]. During the years 2007 and 2008, a large amount of data is available by combining measurements of all three satellite missions. Therefore, all following investigations are restricted to this time period.

Because the aim of the RO method is to receive a global picture of atmospheric conditions, measurements distributed all over the world are required. Figure 3.9 displays the global distribution of the measurements during the year 2008. The radio occultations are globally but not equally distributed. Rather, four bands of preferred data rates are spanning around the globe. The maxima are located around $25°$N/S and $\sim 50°$N/S. The bands originate from the LEO spacecraft's positions in relation to the GPS satellite constellation. The polar orbiting LEO satellites have convenient position to observe rising or setting GPS satellites when crossing the polar regions. Consequently, the according radio occultations are located in the midlatitudes. In contrast, only few occultation measurements are performed when the LEO spacecraft is crossing low latitudes and the RO antenna is directed poleward due to the fact that the GPS satellites are in an $55°$ inclined orbit. Nevertheless, all grid cells include a sufficient amount of measurements in order to perform seasonal analysis on a global scale and especially in the sporadic E relevant midlatitudes. The inhomogeneous data distribution may sophisticate the results concern-
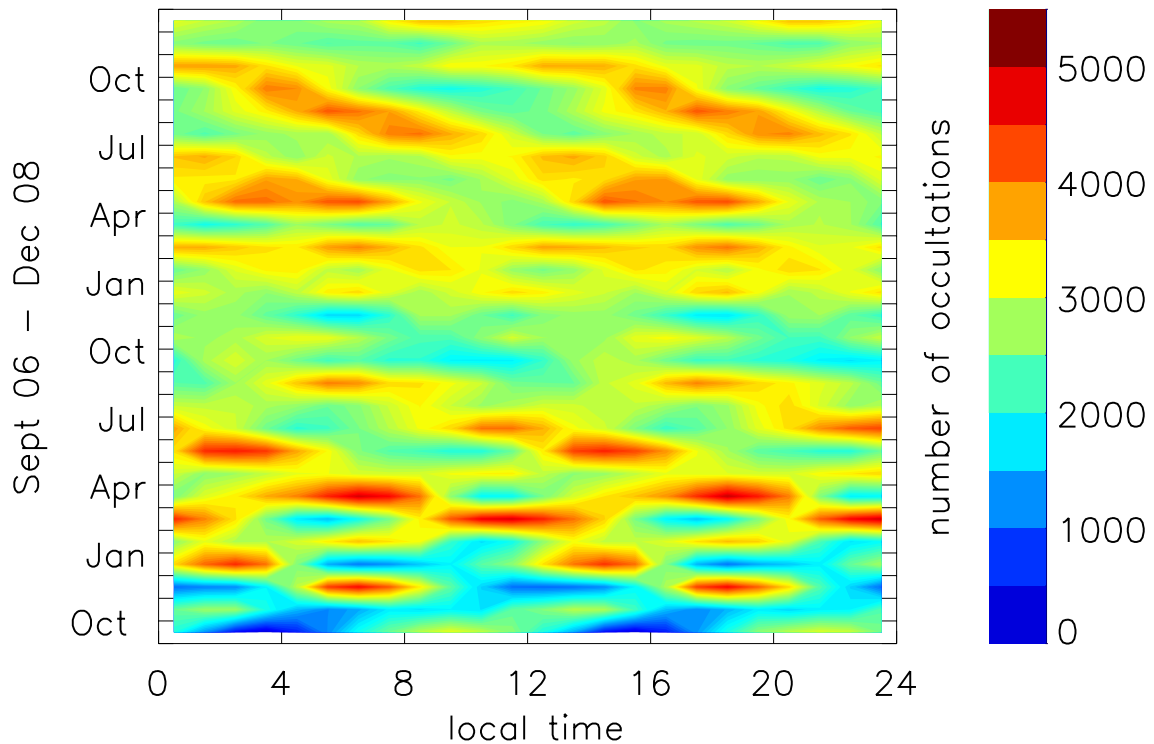
---

[4]http://www.cosmic.ucar.edu/launch/status.html#status

Figure 3.10: Local time distribution of CHAMP, GRACE and COSMIC radio occultation measurements taken between September 2006 and December 2008.

ing global sporadic E distribution. In order to avoid these potential errors mainly relations between detected sporadic E events and the total number of profiles in each grid cell, are considered in the following chapters.

Radio occultation measurements are not equally distributed with respect to local time. The absolute number of radio occultations is shown in Figure 3.10 in dependence on month and local time for the time period September 2006 – December 2008. Generally, two maxima and minima in the number of occultations are observed during the day. The maxima are travelling with about - 3 hours in 1 months. Thus, it takes about eight months until one maximum has covered all local times. The reason for the local time dependency is that the COSMIC satellite's orbit is not sun–synchronous. The satellites drift with approximately 3° in relation to the sun (Pirscher et al., 2010). To avoid a strong local time dependence of the results, in most cases three–monthly means of E_s occurrence are calculated. Between September 2006 and mid 2007 the difference between minima and maxima are exceedingly large. The reason for that is the fact that COSMIC satellites were initially orbiting in a group very close to each other. After they reached their final
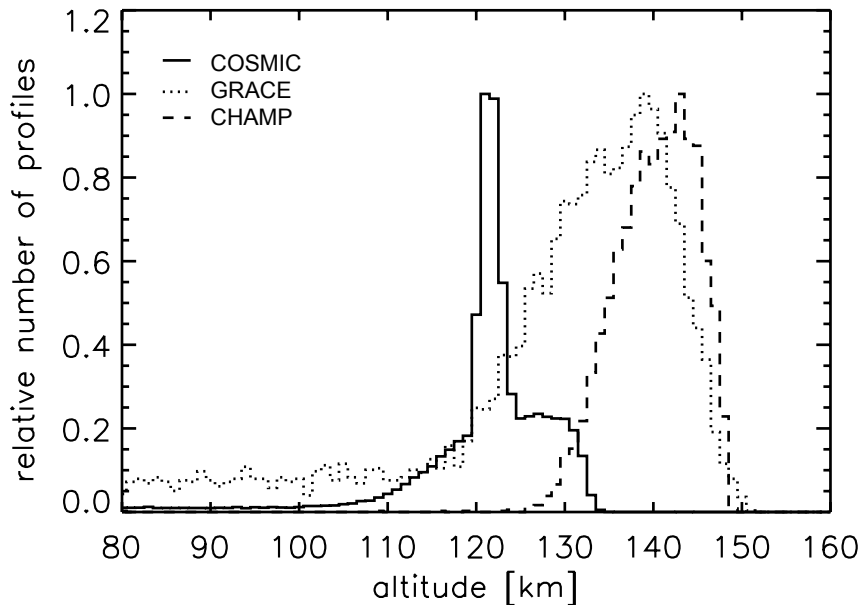
Figure 3.11: Distribution of 50 Hz GPS radio occultation measurements performed by CHAMP (dotted), GRACE (dashed) and COSMIC (solid) during January 2007.

orbit configuration in early 2008, the local time distribution of RO measurements shows a mild and regular semidiurnal component. In September, October and November 2007 the semidiurnal structure is missing and a very low number of occultations is available. As recognisable in Figure 3.8, COSMIC provided fewer measurements during that time period due to technical problems.

Sporadic E layers usually occur at altitudes between 90 and 120 km. Therefore, the 50 Hz RO data should also cover this height range. During an occultation, data recording starts with a sampling rate of 50 Hz at altitudes around 120 km varying slightly between the different satellites. The distribution of the upper boundary for the 50 Hz RO profiles collected by CHAMP (dotted), GRACE (dashed) and COSMIC (solid) for January 2007 is displayed in Figure 3.11. The uppermost value of every single measurement was sorted into 1 km height bins. To get a normalised altitude distribution, the sum of every bin was divided by the total number of RO measurements performed by the respective satellite. The curves show different properties that are dependent on the configuration of the satellites receiver. The GRACE measurements start on average at highest altitudes, mostly above 140 km. The upper boundary of CHAMP 50 Hz occultations show the broadest distribution with most of them starting around 140 km. COSMIC measurements have the narrowest distribution maximising at about 120 km.

Chapter 4

Detection of sporadic E layers from GPS radio occultation measurements

Three different methods are described in literature to extract E_s signature from GPS RO measurements:

1. via SNR (Signal–to–Noise Ratio), where scintillations in SNR are ascribed to sharp vertical electron density gradients at ionospheric altitudes (Wu et al., 2005) and (Wickert et al., 2004),

2. via phase difference ($L_1 - L_2$), which is closely related to TEC (Hocke et al., 2001),

3. via ionospheric excess phases, because the L_1 and L_2 carrier phases react diversely on increased electron density due to their different frequencies (Wu et al., 2005).

Within this study, the three methods are improved in order to relate fluctuations in the data profiles directly to sporadic E layers for the first time. Wu et al. (2005) and Hocke et al. (2001) used standard deviations in SNR profiles or TEC variations, respectively, as indirect measures of E_s activity. All three methods are applied to the CHAMP RO data collected in 2003.

In the following, the algorithms are described in more detail. The results are compared with each other and reasons are given why the SNR based method was applied for all further investigations. The parameters and limiting thresholds of the different filtering routines are shortly summarised in the end of this chapter. In order to compare results of the three different methods, they are applied to one specific profile in the following sections,
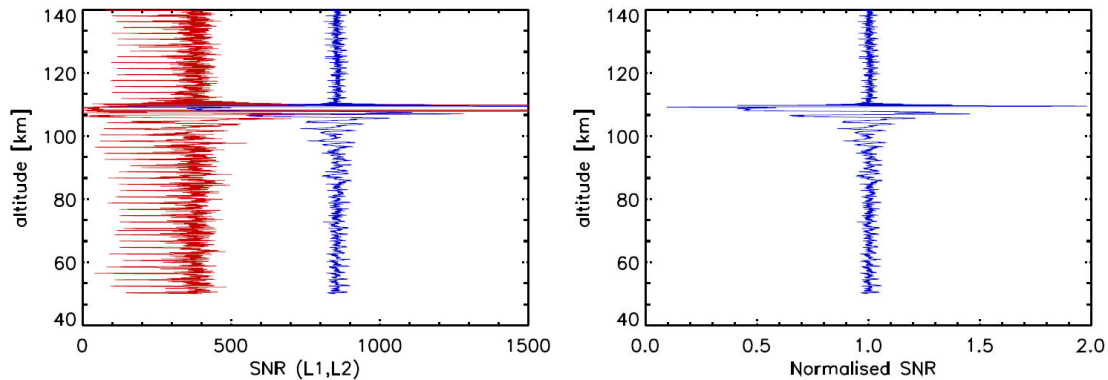
59

Figure 4.1: SNR profiles (left) for the GPS L_1 (blue) and L_2 (red) signal for a CHAMP occultation and the normalised L_1 SNR profile (right).

recorded by the CHAMP satellite on 1 January 2003 at 45°S, 117°E at 00:26 UTC. The involved occulting GPS satellite has the PRN 05.

4.1   Detection of sporadic E layers from signal amplitudes

The SNR value of the GPS L_1 signal is directly recorded by the GPS receiver onboard LEO satellites. In absence of ionospheric disturbances this value is almost constant at altitudes above 35 km, referred to as free–space value, yet decreasing quickly beneath due to fast increasing air density and absorption caused by water vapour in the lower atmosphere. Thus, the RO profiles are cut at 50 km altitude to avoid influences from the lower atmosphere on the used filtering routine. Strong SNR oscillations are mainly caused by the focussing / defocussing effect in ionospheric altitudes. It maximises when the occultation signal path is parallel to the E_s layer and decreases rapidly if it deviates from parallelism.

The SNR free–space value usually reaches values between 250 and 1 000 for CHAMP RO measurements varying significantly from occultation to occultation. It depends on the viewing angle of the GPS satellite with respect to the occultation antenna of the LEO satellite. Therefore, the first step is to normalise each SNR profile to the value 1 using the following equation:

$$SNR'(i) = \frac{SNR(i)}{\overline{SNR}}, \tag{4.1}$$

where $SNR'(i)$ is the normalised SNR at all supporting points and $\overline{SNR}$ represents the mean SNR value calculated for each profile.
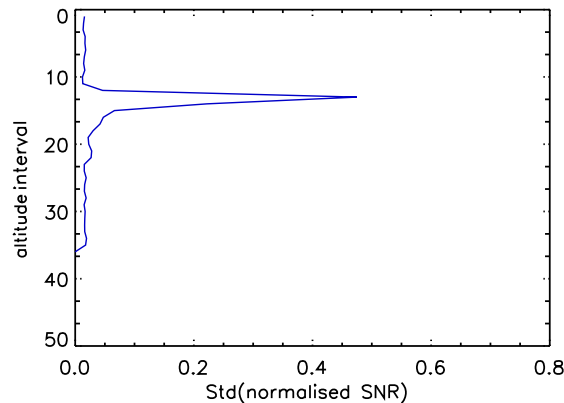
Figure 4.2: The standard deviation of the normalised SNR profile derived from one CHAMP RO on 1 January 2003 at 45°S and 117°E is plotted versus the interval number of the 2.5 km vertical intervals.

It is visible in Figure 4.1 that the SNR of the GPS L_2 signal (red) does not reach the high intensity of the L_1 signal (blue). This is due to the fact that the L_2 signal is encrypted and has to be reconstructed via cross–correlation processes. This leads to a higher fragility and to a stronger noise on this signal. Even though its higher frequency lets the L_2 signal react more sensitively on the charged medium, the mentioned disadvantage prompted us to concentrate on the analysis of the L_1 signal in the following.

The applied detection algorithm for extracting sporadic E information from SNR profiles is based on empirically found limiting thresholds and interval ranges. Therefore, about 500 RO profiles were inspected visually to find out whether they include strong scintillations in a narrow altitude range indicating sporadic E layers. The results from visual inspection were compared to the results from the numerical filtering routine. The routine's parameters were chosen in order to identify preferably the same number of E_s events from the numerical filtering routine and the visual inspection.

As a second step, the standard deviation, $Std(SNR')$, is calculated from the normalised SNR in 2.5 km altitude intervals via:

$$Std(SNR') = \frac{1}{N}\sqrt{\sum_{i=1}^{N}(SNR(i) - \overline{SNR'})^2}, \qquad (4.2)$$

where N is the number of values in each interval and $\overline{SNR'}$ refers to the mean value of the normalised SNR. The 2.5 km altitude interval is chosen to ensure that every interval includes a sufficient amount of values (approximately 50) for a statistical analysis. Nevertheless, the interval is small enough to detect vertically small–scale irregularities such

as sporadic E. If the standard deviation in a single interval exceeds the threshold of 0.2, the disturbance in the SNR profile is regarded as a significant one.

Since E_s are very thin layers, the standard deviation should rise abruptly. Consequently, a second criteria is introduced defining that the standard deviation has to rise suddenly by more than 0.14 between two adjacent intervals. In order to avoid using disturbances which result from other effects than sporadic E, all profiles are excluded from further investigation if the standard deviation exceeds the threshold of 0.2 in more than five intervals. Are all the above mentioned conditions fulfilled, it is considered that the respective profile includes a sporadic E signature. The altitude of the layer is allocated to the altitude of the maximum deviation of the SNR' profile from the normal value 1. Because the strongest variation in SNR profile represents the largest vertical electron density gradient, the true altitude of the sporadic E layer is located closely above or beneath. A double–check considering the standard deviation over the complete SNR profile revealed that the upper (lower) boundary of the E_s layer is detected in 55 % (45 %) of all cases.

With this parameters used by filtering routine, all E_s signatures are detected which were also found by visual inspection of the occultation profiles.

4.2   Detection of sporadic E layers from phase measurements

A second possibility to extract E_s information from GPS RO measurements is to analyse differences in the phases of the L_1 and L_2 signals. Both waves react slightly different on sharp electron density gradients due to their different frequencies. The higher frequency of the L_2 signal induces a stronger bending compared to the L_1 signal when propagating through the same ionospheric layer under same conditions. Hocke et al. (2001) used this phenomenon to identify fluctuations in the E layer's electron content by calculating the phase difference, ΔL, from both signals for the whole occultation profile.

$$\Delta L(i) = L_1(i) - L_2(i). \tag{4.3}$$

The parameter i again is the control variable which indicates the number of the actual supporting points. Figure 4.3 shows a ΔL profile (left). The phase difference is closely correlated to TEC, along the occultation path, which can be calculated via:

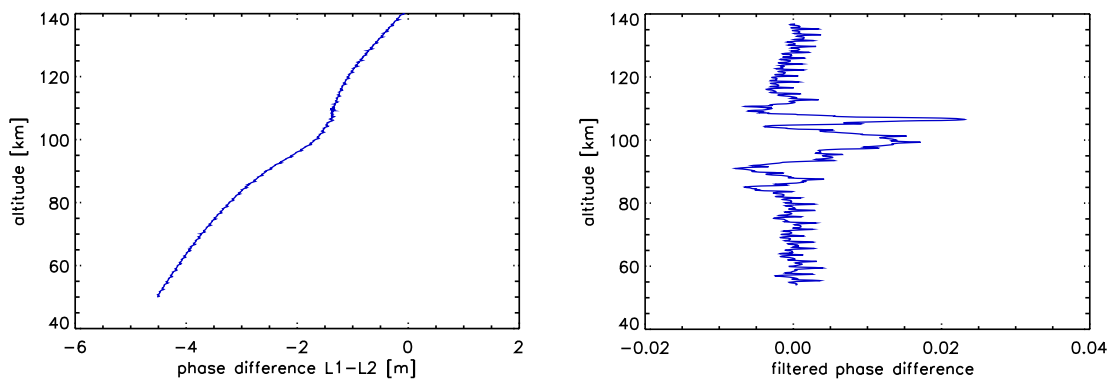$$TEC = \left(\frac{f_1^2 \cdot f_2^2}{f_1^2 - f_2^2} \right) \cdot \Delta L \cdot \frac{1}{K}, \tag{4.4}$$

Figure 4.3: Profiles of the phase difference, ΔL, (left) and the according low–pass filtered data (right).

with

$$K = \frac{e^2}{4\pi\varepsilon_0 m_e} = 40.3\frac{m^2}{s^2}, \tag{4.5}$$

where f_1 and f_2 stand for the two GPS frequencies, ε_0 represents the permittivity and m_e the electron mass.

A low pass filter is used to separate vertically small–scale fluctuations in the phase difference ΔL from background variations. The result is depicted on the right hand side of Figure 4.3. Analogue to the SNR method, the standard deviation is calculated from the phase difference profile in 2.5 km height intervals. Again, a limiting threshold is introduced. If the standard deviation is exceeding this threshold of 0.009 between one and five times, the profile is considered to include a sporadic E signature. If the threshold is reached more than five times, the respective profile is rejected from further analysis due to disturbances over a large height range which are not necessarily caused by sporadic E. The altitude of maximum deviation from the mean value of the low–pass filtered profile is considered to be the altitude of the E_s layer.

4.3 Detection of sporadic E layers from ionospheric excess phases

A third method for extracting ionospheric disturbances from RO measurements is the detection of sporadic E layers from ionospheric phase delay measurements. The excess phase is defined as the extension of the ray path induced by ionospheric conditions such as sporadic E layers. It is closely related to the *TEC* value along the RO signal path as
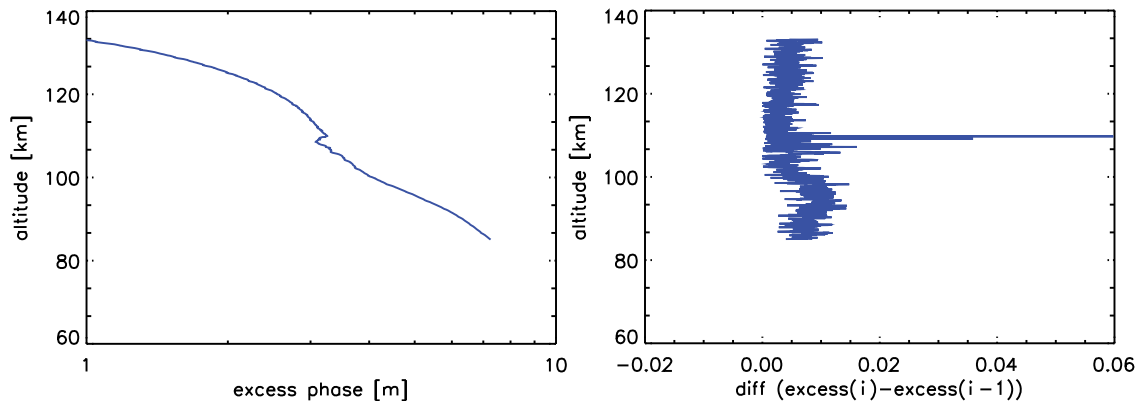
Figure 4.4: Profiles of the ionospheric excess phase (left) and the point to point variation of the excess phase (right).

indicated by:

$$d_1 = \pm \frac{K}{f_1^2} \cdot TEC, \tag{4.6}$$

where d_1 stands for the phase delay and f_1 for the used GPS frequency. The detection method relies only on measurements of the GPS L_1 signal and needs no information on the behaviour of the much noisier L_2 signal.

Wu et al. (2005) demonstrated that the excess phases can also be used to identify electron density enhancements in the ionospheric E region. A typical phase delay profile is presented on the left panel of Figure 4.4. Relative to the difference between the minimum and maximum value of the profile, the variations found in E_s altitudes are small. To extract these small fluctuations, the first step in the detection algorithm is to let the fluctuations appear more obvious in the profile. To achieve this, the difference, *diff*, of two adjacent values is calculated via:

$$diff(j) = d(i) - d(i + 1), \tag{4.7}$$

where *i* and *j* are control variables. The resulting profile is displayed in Figure 4.4 (right) with a distinctive peak around 110 km. Subsequently, the profile is divided in 1 km altitude sections and the standard deviation is calculated for each interval (Figure 4.5). In the following, the profile has to fulfil two criteria to be accepted as a sporadic E profile.
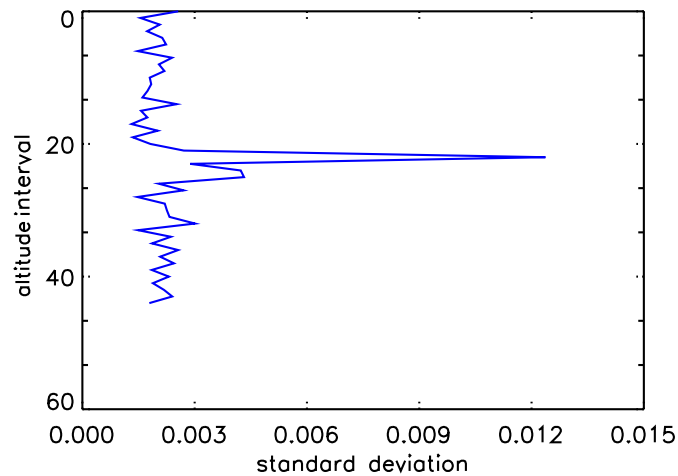
Figure 4.5: Standard deviation profile calculated from the ionospheric excess phase. The vertical intervals stretch over 2.5 km.

1. The standard deviation has to exceed the value of 0.005 in at least one section but not more than 5 sections.

2. The standard deviation has to increase abruptly between two adjacent sections by at least 0.0025.

The altitude of the section including the maximum standard deviation is associated with the sporadic E altitude.

4.4 Comparison of sporadic E detection algorithms

The three introduced methods of sporadic E detection from GPS radio occultation measurements provide nearly equal results. Their limiting thresholds and parameters are summarised in Table 4.1.

	SNR	Phase	Excess Phase
△ h of intervals	2.5 km	2.5 km	1 km
Std	0.2	0.009	0.005
max. number of intervals with large Std	5	5	5
△ Std between two adjacent intervalls	0.14	–	0.0025

Table 4.1: Parameters of the different sporadic E detection algorithms.

The daily number of detected sporadic E layers from CHAMP RO data during June, July and August 2003 is displayed in Figure 4.6. The most E_s signatures are extracted from

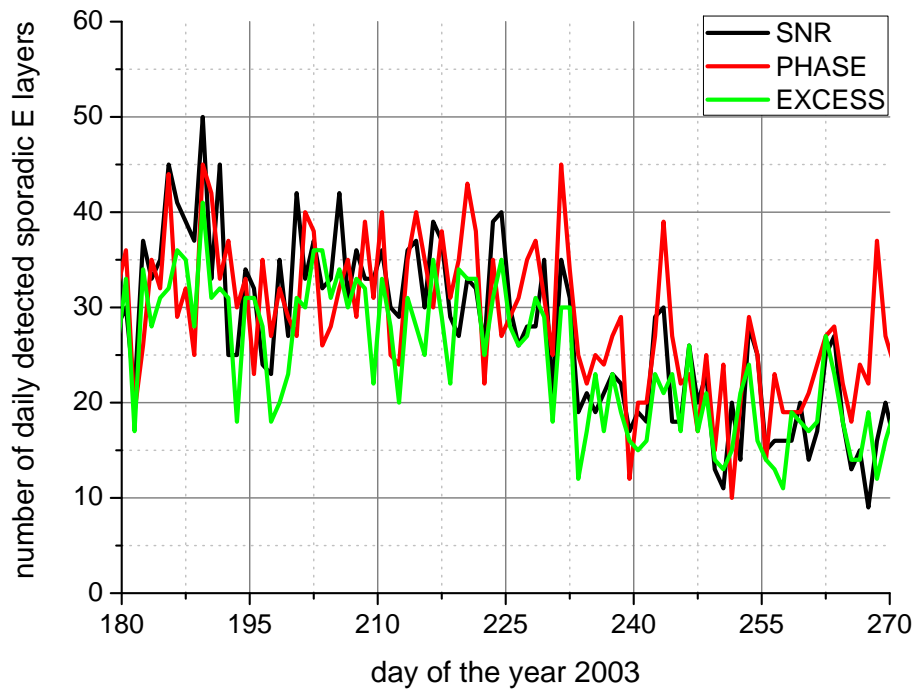**Figure 4.6:** Comparison of the daily number of detected sporadic E layers from the three different detection algorithms during June, July and August 2003 based in CHAMP RO measurements. The results from the SNR based method are indicated in black, the ones received from excess phase algorithm are indicated in green and the results from phase detections are given in red.

the data set with the phase method (red), on average 30 E_s layers per day. The SNR algorithm (black) delivers on average 28 sporadic E layers, while the method using ionospheric excess phases (green) detects about 27 E_s layers per day. Although the number of detected E_s can differ significantly between the methods on one day, the lines show generally a similar course. For instance, at day 268, 37 E_s layers were found via analysing the phase differences. On the same day the SNR / excess method only detects 16 and 12 E_s layers, respectively. The decrease of the daily number of sporadic E layers starting at day 225 is reproduced with all techniques. The algorithms are able to detect a similar number of daily sporadic E events. Nevertheless, it was decided to focus on the SNR analysing method for all further investigations.

The SNR measurements have several advantages instead of using the retrieved quantities. The most important one is that the SNR profiles are obtained directly from the L_1 signal without smoothing or further treatment of data. Any smoothing of data may loose important information on the vertically small sporadic E features. Further, the SNR

method does not rely on the noisier L_2 data and does not require the solution of LEO and GPS clocks.

It was also decided not to extract E_s information from electron density profiles. The derivation of profiles requires additional assumptions like spherical symmetry of electron density, that is not valid for sporadic E (Hajj and Romans, 1998). The SNR is relatively easy to analyse because it only relies on raw GPS L_1 data and is therefore free of errors introduced by data analysis to derive, e.g., excess phase information.

Chapter 5

Validation of the derived sporadic E parameters

Sporadic E layers are detected by applying the described SNR algorithm in Chapter 4. Since the algorithm is based on several assumptions, validations are required to confirm the analysis and to evaluate the accuracy of the applied procedure.

The validation process is divided into two parts. As a first step, a model to calculate the GPS wave propagation in the ionosphere is used to illustrate that the scintillations found in GPS RO signals from CHAMP, GRACE and COSMIC can in fact be associated to sporadic E layers. In a second step sporadic E occurrence and altitudes from GPS RO measurements are compared with E_s altitudes detected by ionosonde data from Juliusruh ($54°$N, $13°$E), Germany.

5.1   Simulation of GPS signal propagation in the ionosphere

The aim of this study is to find out how the SNR of the GPS signal reacts when crossing a sporadic E layer and whether the observed scintillations can be associated directly to E_s without any height displacement. Additionally, it will be investigated if these scintillations have another source like disturbances in the F region of the ionosphere.

The propagation of GPS signals in Earth's neutral atmosphere and ionosphere is studied usually using simulations based on the application of a multiple phase screen (MPS) model (e.g., Beyerle et al., 2003).

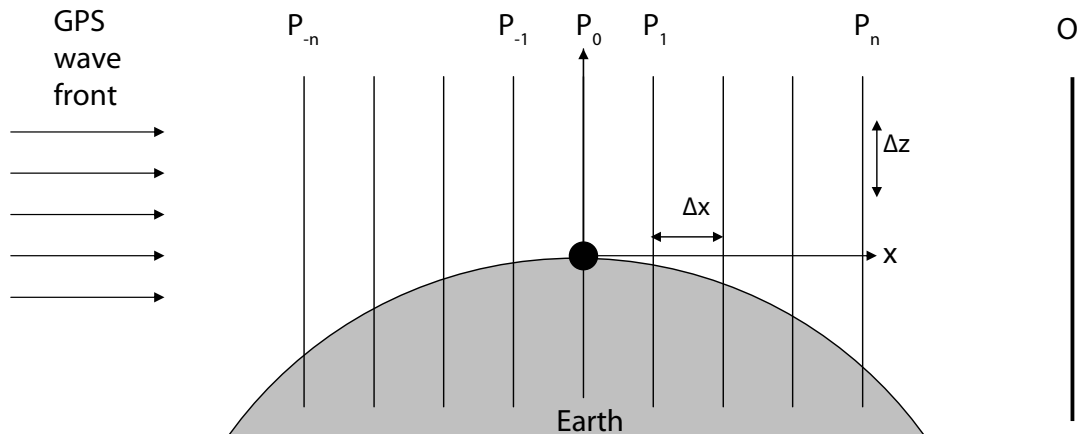In this study the model is used to understand better the GPS signal's SNR variations

<center>69</center>

Figure 5.1: Scheme of the multiple phase screen method. The atmosphere is represented by a series of phase screens. An electromagnetic wave propagates through the screens from left to right and is detected on the observation screen O.

caused by layers of enhanced electron density in the ionosphere. The model setup is visualised in Figure 5.1. The incident wave is a sine wave with unit amplitude. Within the model the atmosphere is divided into a series of segments each confined by so–called phase screens. At every single phase screen, the propagating signal is delayed subsequently by an amount of ionisation determined from the local index of refraction. Between the phase screens, the signal travels as if in vacuum.

Important parameters like the distance between the phase screens and the spacing between vertically arranged discretisation points are freely adjustable. The used settings are summarised in Table 5.1.

Parameter	Setting
Number of phase screens	501
Height discretisation	$\Delta z = 1\,\mathrm{m}$
Horizontal discretisation	$\Delta x = 4\,\mathrm{km}$
Distance LEO	$2 \cdot 10^6\,\mathrm{m}$
Frequency of the propagating wave	$1.575 \cdot 10^9\,\mathrm{s}^{-1}$

Table 5.1: Parameter definitions for the MPS simulations.

An ideal receiver tracking behaviour is assumed and noise is ignored. The result of the MPS calculation is the signal's amplitude at the last phase screen. For modelling of GPS signal propagation in ionospheric altitudes, Chapman–layers are added to the refractivity
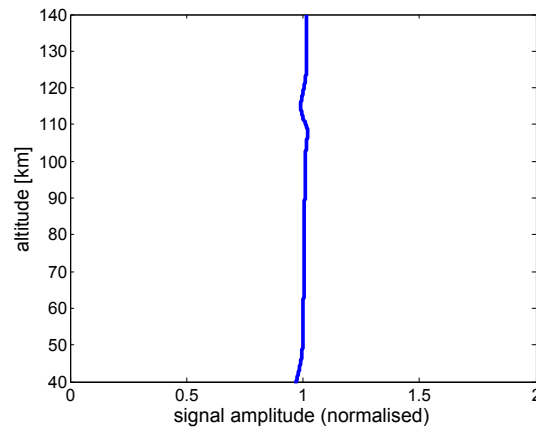
Figure 5.2: Example for a SNR profile as a result of a MPS simulation of a GPS L_1 signal travelling through an ionospheric F and E layer.

model of the atmosphere as indicated in Equation (5.1) forming the ionospheric F and E layers. The refractivity field is assumed to be spherically symmetric. Effects from the lower neutral atmosphere are not considered here since GPS signals are only propagating at altitudes above 40 km because in this study we focus on sporadic E. The F and E layers are parameterised parabolically by:

$$N_e = N_{e0} \cdot \exp\left(\frac{1}{2}\left(\frac{1 - (h_0 - h_{E,F})}{H}\right) - \exp\left(\frac{-(h_0 - h_{E,F})}{H}\right)\right), \qquad (5.1)$$

where N_e is the electron density, N_{e0} the core density of the layer, $h_{E,F}$ denotes its altitude and H its thickness. The parameter h_0 is a control variable which indicates the vertical distance from the core.

As a first step it was investigated how the SNR values of the simulated measurements react on an embedded F and E layer. In the model ionosphere these layers were parameterised with the conventions in Table 5.2 and added to the model refractivity profile.

	F − layer	E − layer
Altitude	$h_F = 300$ km	$h_E = 120$ km
Scale thickness	$H = 60$ km	$H = 10$ km
Core electron density	$N_{e0} = 1 \cdot 10^{12}$ m^{-3}	$N_{e0} = 1 \cdot 10^{11}$ m^{-3}

Table 5.2: Characteristics of the E and F layer included in the ionospheric refractivity model for multiple phase screen simulations.

As visible in Figure 5.2, the resulting SNR profile includes no envisaged disturbances excited by the high electron density values of the F layer mapping down to E layer altitudes.
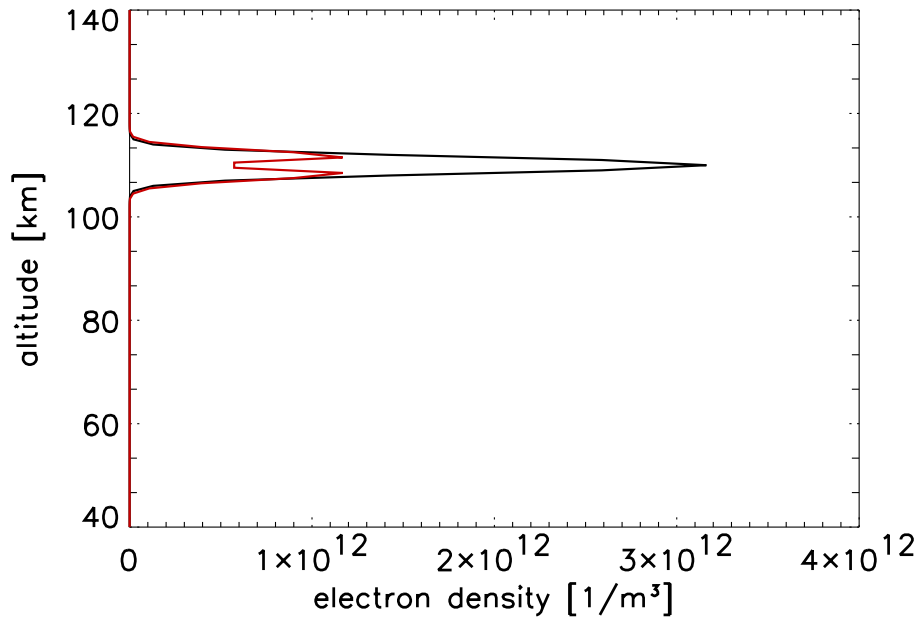
Figure 5.3: Electron density profile (black) and corresponding profile of vertical electron density gradients (red) calculated from the paramterised sporadic E layer used in MPS routine.

Only the E layer is visible as a shallow bump due to its larger vertical electron density gradients compared to F layer electron density gradients. Consequently, all strong SNR variations appearing below 140 km may be allocated to electron density anomalies in this altitude range. Disturbing effects from a regular F layer are unlikely and will be neglected in the following. Also a disturbed F layer, in presence of e.g. TIDs, will have no influence on the modelled SNR profiles in E region altitudes because F layer influences do not map to E layer altitudes as shown in Figure 5.2.

In a second step a sporadic E layer is added with a hyperbolic curved shape being concavely on its lower side. The layer is parametrised by the following equation (From and Whitehead, 1978):

$$N_e = N_0 \frac{\sqrt{S_0 F \exp(\frac{-x^2}{2P^2})}}{\sqrt{D}} \exp\left(\frac{-z^2 S_0 F \exp(\frac{-x^2}{2P^2})}{2D}\right), \tag{5.2}$$

Figure 5.4: Comparison between a measured (right, red) and a simulated SNR (left, blue) profile both including a sporadic E layer. The right profile was measured by CHAMP on 1 January, 2003 at 45°S and 117°E at 00:26 UTC.
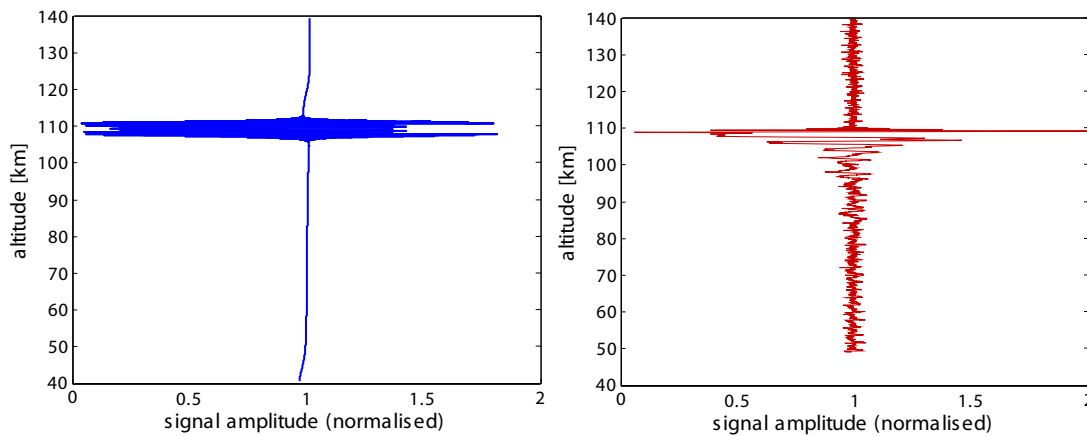
with:

$S_0 F = 0.002\,\text{s}^{-1}$	ratio of vertical ion velocity to horizontal ion velocity
$N_0 = 10^{15}\,\text{m}^{-2}$	core electron density
$z = 110\,\text{km}$	altitude of E_s layer
x	horizontal distance from center
$D = 200\,\text{m}^2/\text{s}$	diffusion coefficient
$P = 5\,\text{km}$	scale size of the vertical electron density profile

The corresponding electron density profile (black) and the vertical gradients in electron density (red) is shown in Figure 5.3. The resulting SNR profile from the simulation is displayed in Figure 5.4, left. It includes a very strong and clear scintillation at the altitude of the embedded model sporadic E layer near 110 km. In fact, a positive height offset is registered between the altitude of the embedded sporadic E layer and the maximum variation in the resulting SNR profile. It usually amounts to 500 m considering the average of several model runs with slightly different basic conditions. Regarding the detection algorithm (section 4.1) from radio occultation measurements enabling a height resolution of 1 km, the accuracy of the algorithms is sufficient to get a correct altitude assignment.

A measured SNR profile from a CHAMP occultation is displayed on the right hand side of Figure 5.4. Its shape is very similar to the simulated profile on the left and the sporadic E signature is also attributed to an altitude of 109 km. The small equidistant oscillations

covering the complete altitude range are due to background noise and the GPS receiver properties which are ignored in the simulations.

In summary, the MPS modelling method is an adequate and accepted technique to simulate the propagation of radio waves in Earth's atmosphere and ionosphere. Even thin layers such as sporadic E are reproduced in the modelled SNR profiles. Therefore this method is capable to test whether the scintillation in radio occultation measurements are caused by sporadic E. It was shown that the shape of the measured and the simulated profile are quite similar under best measuring conditions. The altitude assignment of the E_s layers does not show large differences between the measured and the simulated profile. Thus, it is concluded that the algorithm described in section 4.1 is suitable to detect the existence and to determine the altitude of sporadic E layers in GPS RO data accurately.

5.2   Comparison of GPS RO sporadic E altitudes with ionosonde measurements

The aim of the following study was to compare the sporadic E altitudes found in GPS RO measurements with established ground based ionosonde soundings. Coinciding sporadic E detections from COSMIC, located within $\pm 5°$ in north–south and east–west direction from the ionosonde are included in the comparison for 2007. The Juliusruh (54°N, 13°E), Germany ionosonde was chosen because it provides a nearly continuous time series with a temporal resolution of 15 minutes.

Ionosonde soundings give reliable measurements of the electron density and the altitudes of the layers peak density. The altitudes of sporadic E layers are given as virtual heights, $h'E_s$, values that represent the lower boundary of the measured sporadic E layers. Due to the fact that the real height is very intricate to calculate, only virtual heights are published in most cases. The data used here are taken from the DIAS (European Digital upper Atmospheric Server) project webpage[1]. In most cases, the virtual height does not equal the geometrical height. The difference between them enlarges with increasing electron density along the signal path. For sporadic E investigations, the virtual height depends on the electron concentration in the D and lower E layer. Consequently, the comparison (Figure 5.5) only focussed on nighttime or winter sporadic E events where the D layer and background ionisation is low. In total, 37 coincidences were found in 2007 including a sporadic E layer. A high correlation of about 90 % is found between E_s altitudes detected

---

[1]http://dias.space.noa.gr:8080/LatestDias2/loginPage.jsp

Figure 5.5: Comparison of sporadic E altitudes detected by ionosonde Juliusruh with in total 37 coinciding E_s altitudes found in COSMIC radio occultation measurements. Taken from Arras et al. (2010).

with the different methods. A height offset of approximately 2.8 km is calculated from the regression analysis in 100 km altitude. This means that E_s altitudes are overestimated by the RO method by ~ 2.8 km compared to the virtual heights given by the ionosonde data. The slope of 0.98 suggests that the overestimation is approximately constant with height in the range between 90 and 115 km where E_s layers are found. Since the virtual heights are slightly larger than the geometric ones, the offset between GPS RO and ionosonde E_s altitudes is larger than the calculated ~ 2.8 km.

Chapter 6

Climatology of sporadic E occurrence

The aim of this chapter is to visualise and to discuss the global sporadic E rates in dependence on latitude, longitude, altitude and local time. For the first time, the SNR method is applied to a multi–satellite data set comprising over several years.

The following figures are based on combinations of measurements performed by the CHAMP, GRACE and COSMIC satellites. The plots show for the first time monthly mean sporadic E occurrence rates based on satellite measurements binned in a $5° \times 5°$ geographic latitude / longitude grid with a resolution of 1 km in altitude and 1 hour in local time. Monthly mean values are merged to seasonal means centered around January, April, July and October. Seasons always refer to northern hemispheric conditions unless it is explicitly stated differently. The occurrence of E_s layers shows variations on different time scales. Besides daytime dependent variations, also the seasonal and interannual variabilities are analysed.

Generally, the E_s preferably occur at midlatitudes in the summer hemisphere, while the rates are low during winter. Figure 6.1 and 6.2 display the global E_s occurrence during the years 2007 and 2008, respectively, and give a general overview on global sporadic E occurrence. The E_s rate of 14.4 % is observed in both years in global and annual mean. High E_s rates are found in the northern / southern hemisphere during summer / winter season. In contrast, nearly no E_s events are detected on the northern / southern hemisphere during winter / summer conditions. Moderate E_s activity is found during equinox seasons in equatorial latitudes. Small scale variations with distinctly higher / lower E_s occurrence rates compared to adjacent grid cells are visible but may be artefacts from the distribution of radio occultation measurements. They could easily be removed by smoothing the data.

77
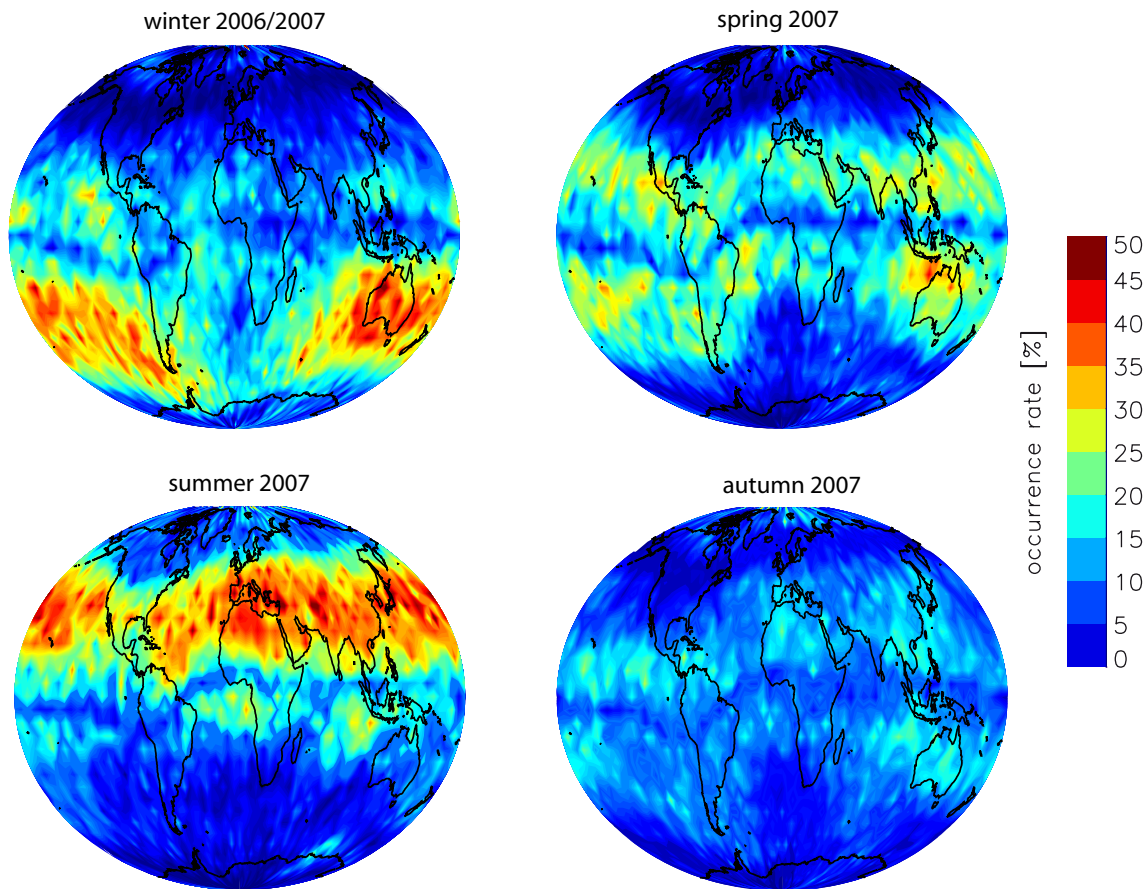
Figure 6.1: Seasonal global distribution of sporadic E occurrence rates in 2007 derived from CHAMP, GRACE and COSMIC GPS RO data. Each plot contains measurements collected during three months; winter (December 2006, January and February 2007), spring (March, April, May 2007), summer (June, July, August 2007) and autumn (September, October, November 2007).

Despite, no smoothing is applied since also real strong horizontal gradients in sporadic E rates would disappear. For example the magnetic equator appears as a slim line at low latitudes. Along this line, nearly no sporadic E events are observed during all seasons (Arras et al., 2008).

Having a closer look at the maps of Figure 6.1 and 6.2 one can see that in winter E$_s$ events appear as a broad band spanning around the globe in southern midlatitudes between $20-50°$S. This band is interrupted over the South Atlantic Ocean and South Africa. This gap stretches across approximately $90°$ in longitude. It is caused by an anomaly in Earth's magnetic field and will be discussed in more detail in Chapter 7. Over the
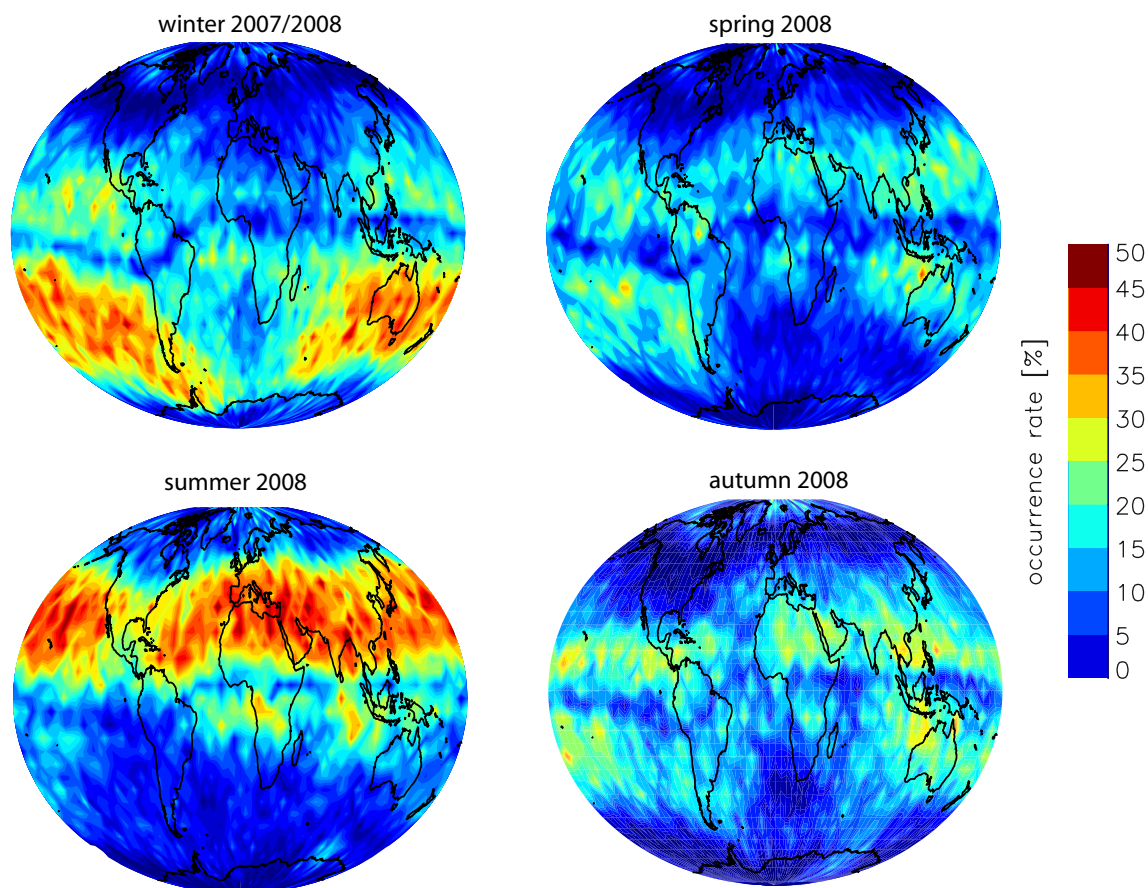
Figure 6.2: Same as Figure 6.1 but for the year 2008.

South American continent, high sporadic E rates stretch remarkably far south reaching the northern boundary of Antarctica's Peninsula. Also in the low latitudes $(10-20°N)$ of the northern hemisphere a weak E_s activity is found. But nearly no layers are detected in northern midlatitudes and over both polar regions. The highest E_s rates are observed over Australia reaching values of around 50 % i.e. every second GPS RO profile contains an E_s signature.

During spring the E_s distribution is not concentrated on one single hemisphere. A moderate sporadic E activity is observed in low latitudes on both hemispheres. Sporadic E rates between 20 % and 30 % are predominantly observed. The maxima with 45 % in 2007 and 39 % in 2008 are located again in the Australian region. It is noticeable that the bands of highest sporadic E rates do not follow geographical latitudes as they do approximately during solstice seasons. This phenomenon is connected to magnetic field properties as discussed in Chapter 7.1.

Season	Max. E_s rate	Mean E_s rate	Coordinates of Maximum
Winter 06/07	54%	16%	125°E, 20°S
Spring 2007	45%	13%	120°E, 15°S
Summer 2007	53%	16%	0°, 45°N
Autumn 2007	50%	13%	80°W, 15°N
2007 total	34%	14%	105°E, 15°S
Winter 07/08	53%	17%	100°W, 35°S
Spring 2008	39%	12%	120°E, 15°S
Summer 2008	55%	17%	60°E, 35°N
Autumn 2008	43%	13%	145°E, 15°S
2008 total	34%	14%	90°E, 20°N

Table 6.1: Summary of maxima and global mean sporadic E rates from GPS RO data for the years 2007 and 2008.

During summer high sporadic E rates appear as a band spanning completely around the northern hemisphere between about $20-50°N$. There is only a small minimum in E_s rates appearing over North America. A weak sporadic E activity is found on the southern hemisphere near the equator over Africa, the Indian Ocean and Oceania.

In contrast to autumn 2007 where sporadic E rates are very low, the occurrence rates during autumn 2008 reach comparable values to the ones measured in spring ($\sim 30\%$). Sporadic E layers are confined to lower latitudes in the northern and southern hemisphere reaching occurrence rates $\sim 20\%$.

Table 6.1 summarises the mean global sporadic E occurrence rates, their maxima and the location of their maxima for each season. Generally, the characteristic of global E_s distribution is quite similar for both years 2007 and 2008. Some differences are identified for the equinox seasons where spring 2007 shows higher E_s rates than observed during spring 2008 while the autumn months behave contrarily. Australia takes apparently a special position because high E_s rates are observed frequently in the northern Australia area. Two minima are also found in global sporadic E rates; a distinct one over the South Atlantic and a weak one over the Northern American continent. Both minima are only visible during southern summer and northern summer, respectively.

The RO technique is a relatively new method and thus long–term results of sporadic E behaviour cannot be expected. Currently, CHAMP provides the longest available consistent time series of GPS RO measurements comprising nearly eight years. Nevertheless, the CHAMP data set was used for a trend analysis in global sporadic E occurrence rates. Figure 6.3 shows the time series of latitude dependent monthly E_s rates measured by CHAMP between January 2002 and October 2008. The latitudinal resolution of this is
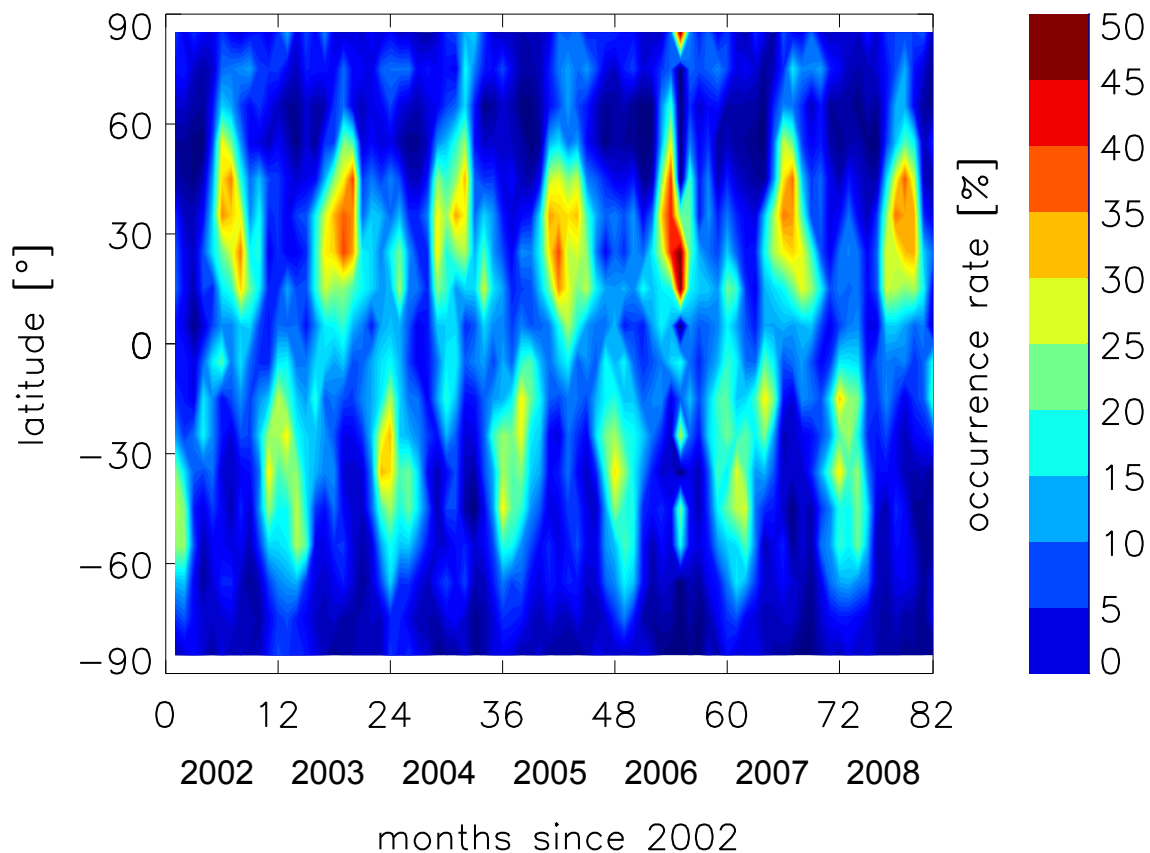
Figure 6.3: Time series of monthly latitude dependent sporadic E rates between 2002 and 2008 derived from CHAMP GPS RO data.

of 10°. The expected summer maximum alternating between the northern and southern hemisphere is clearly visible. The individual summer maxima are interrupted by very low E_s rates in spring and autumn. Weak secondary maxima are found at low latitudes on the winter hemisphere. In general, the E_s rates in the southern hemisphere are apparently reduced by 25% compared to the northern hemisphere. This is a deception resulting from the minimum in sporadic E rates in the South Atlantic region. Since E_s rates are integrated over all longitudes in a 10° latitude range to reach the values used in Figure 6.3, the low E_s rates over the SAA diminishes the integrated sporadic E rates significantly.

The summer maxima vary in intensity, in duration, and in dimension. But usually values around 40 % E_s occurrence frequency are observed in the northern hemisphere. This is different in the summer 2004 and 2006. While the summer 2004 displays only weak sporadic E activity ($\sim$ 30 %), the summer 2006 shows intens E_s rates of up to 50 %. Furthermore, the E_s maximum in summer 2004 is only of short duration. In contrast, the maximum in 2003 is a very broad one which extends from May to September.
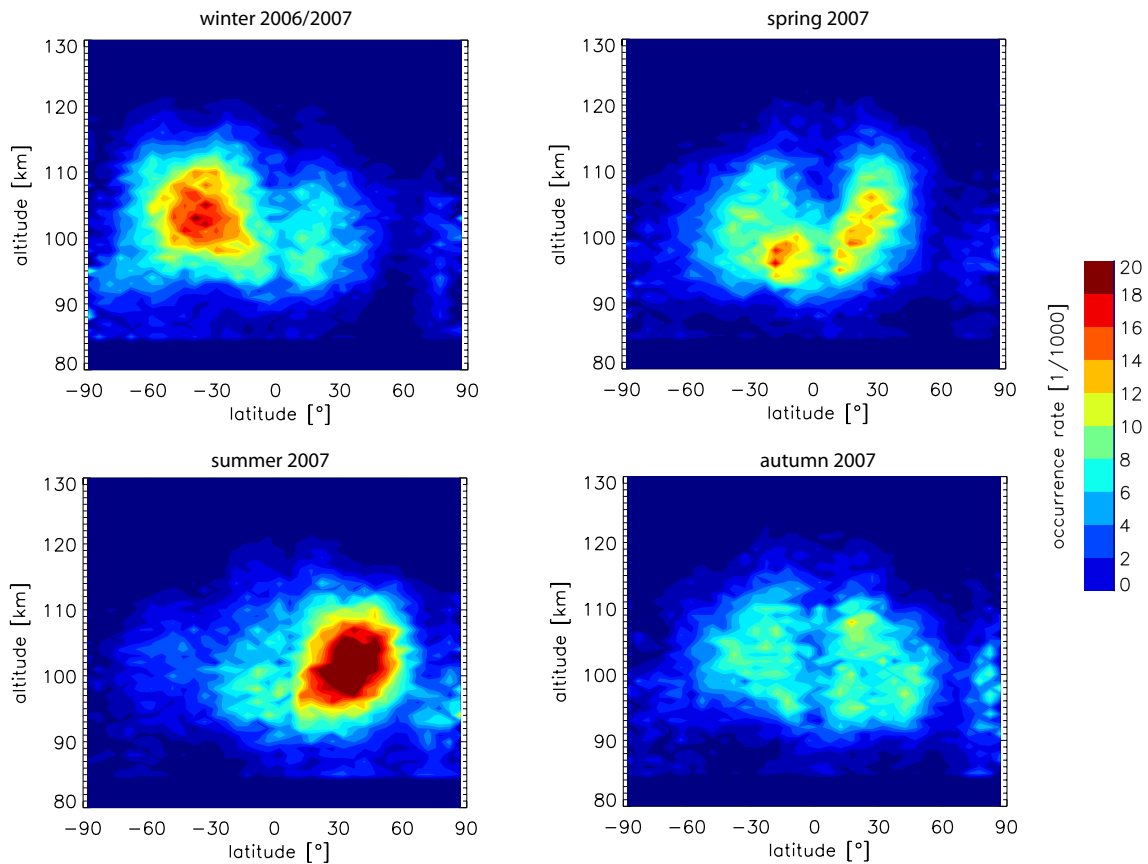
Figure 6.4: Sporadic E occurrence rates in altitude / latitude cross–sections detected from CHAMP, GRACE and COSMIC GPS RO data for the same time intervals as in Figure 6.1. The figures are plotted in an 1 km × 5° resolution.

In the southern hemisphere, typical values of the southern summer maximum amounts about 30%. A strong maximum is observed during southern summer 2003 / 2004 with sporadic E rates of approximately 35%. Usually, weak E_s rates of only 25% are observed in southern summer.

Considering the poleward boundary of the summer / winter maxima in the northern / southern hemisphere, one notices that this boundary migrates southward / northward between 2002 and 2005. The maxima in winter 2005 / 2006 in the southern hemisphere and in summer 2006 in the northern hemisphere show a special characteristic. Both maxima reach sub-polar latitudes. Afterwards, the poleward boundaries migrate slightly towards the equator again especially in the northern hemisphere. The single red spot in the northern polar region in northern hemispheric summer in 2006 may result from a low number of measurements in this grid point with one of them including a sporadic E signature. The polar E_s occurrence is discussed in the end of this section.
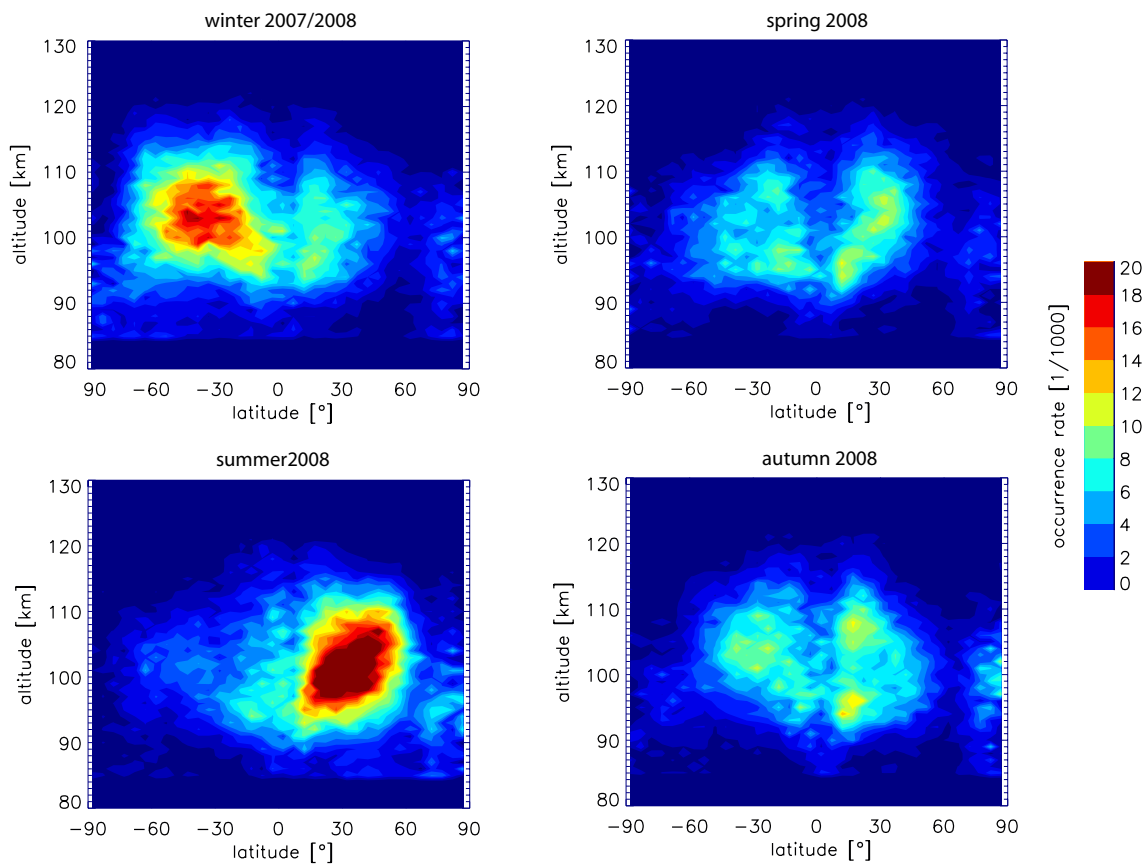
Figure 6.5: Sporadic E occurrence rates in altitude / latitude cross − sections derived from CHAMP, GRACE and COSMIC radio occultations for the same time intervals as in Figure 6.2. The figures are plotted in an 1 km × 5° resolution.

In Figure 6.4 and 6.5 the focus is set to latitude dependent sporadic E altitudes. As known from the detection algorithm (Chapter 4.1), E_s altitudes are determined with a 1 km height resolution. Note that sporadic E rates are in 1 / 1000 instead of 1/100.

Sporadic E layers appear in the altitude range between 90 and 120 km with a maximum occurrence between 95 and 115 km. The sporadic E latitude distributions are reproduced in the same way as in the maps of Figure 6.1 and 6.2. Also the gap along the equator is visible during all seasons in the latitude / altitude cross–sections.

In winter 2006 / 2007 a strong E_s occurrence is observed between 100 and 110 km with highest sporadic E rates of about 2% at approximately 105 km altitude at 40°S. A secondary maximum of nearly 1% appears in the northern hemisphere between 95 and 105 km altitude. During spring a butterfly–like structure occurs with two weak maxima. One maxima appears in the low–latitudes of the northern hemisphere in the height range between 95 and 105 km. The second peak appears in the southern hemisphere slightly

Figure 6.6: Sporadic E occurrence in dependence on latitude and local time in 2007. The seasonal time intervals are chosen analogue to Figure 6.1

below 100 km. A strong maximum is observed between 10°N and 50°N in an altitude of 95 to 110 km with more than 2% sporadic E occurrence frequency during summer 2007. However, the frequently noticed weaker secondary maximum in the winter hemisphere is missing here. During autumn a weak sporadic E activity of up to 1% is found in low latitudes in both hemispheres at altitudes between 95 and 110 km.

The characteristics of E_s distribution during the year 2008 is generally quite similar to the one monitored in 2007. Only during equinox seasons, differences in the occurrence rates are observed according to the variations noticed in Figure 6.1 and 6.2. Accordingly, E_s activity during spring 2008 is weaker than during spring 2007. In autumn 2008, the sporadic E activity is slightly stronger than during autumn 2007.

Since the formation of sporadic E layers is dependent on wind shears produced by atmospheric tides, their appearance ought to show a dependence on local time. This feature is reflected in Figure 6.6 for the year 2007 and in Figure 6.7 for 2008. These figures depict
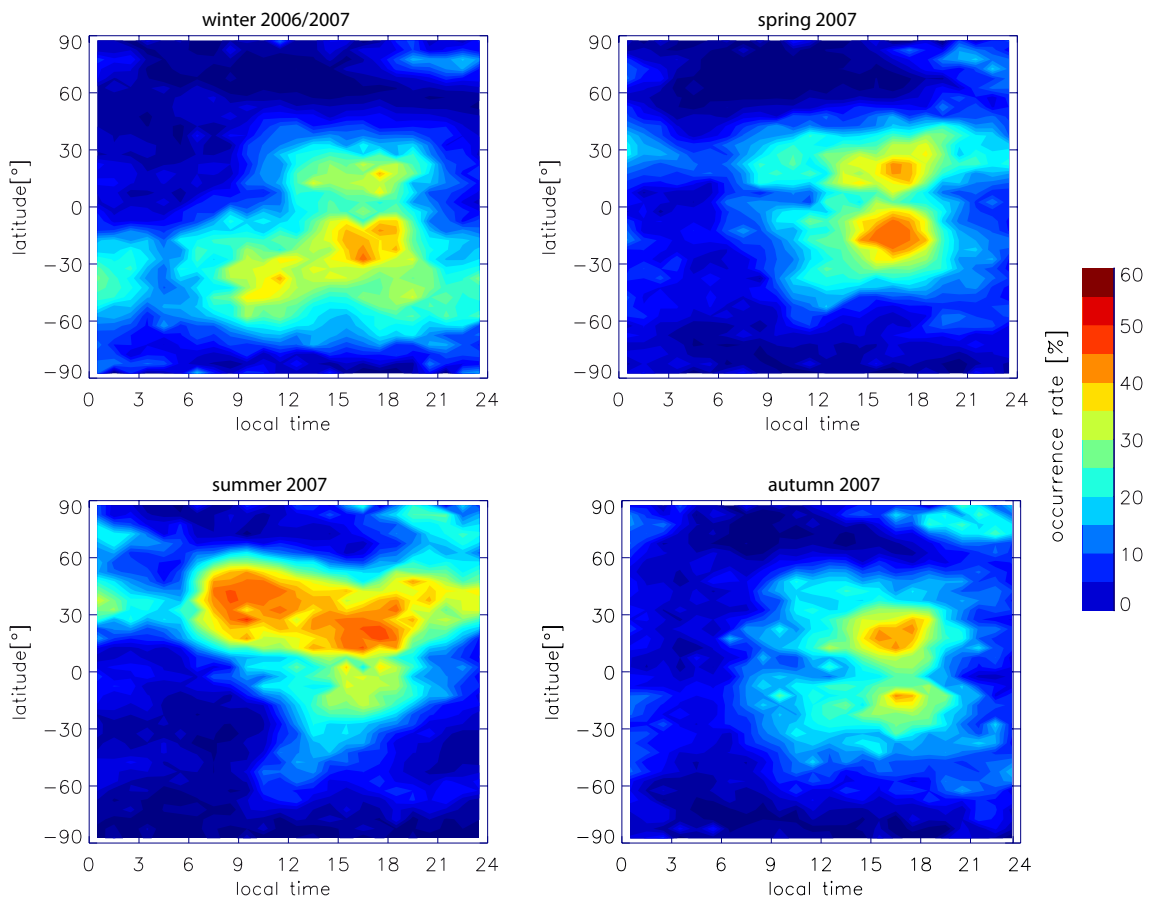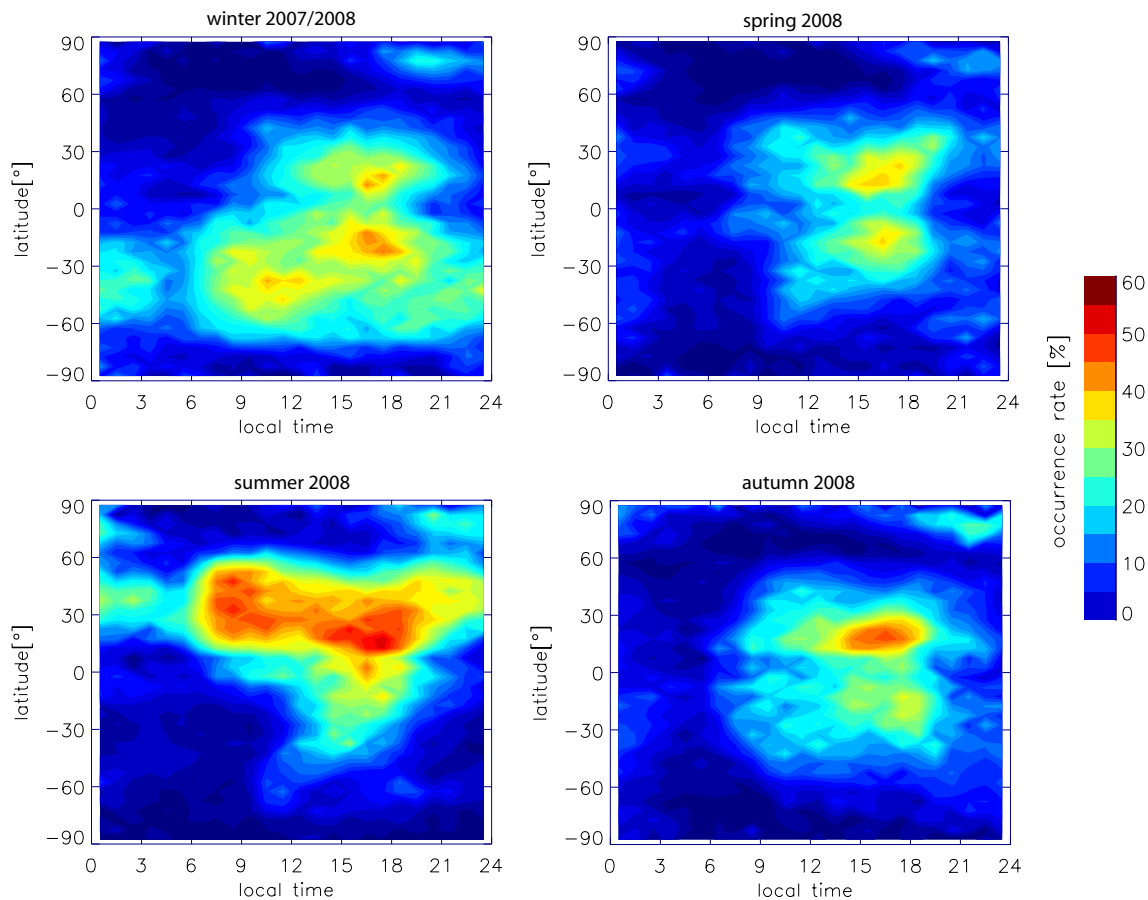
Figure 6.7: Sporadic E occurrence in dependence on latitude and local time in 2008. The seasonal time intervals are chosen analogue to Figure 6.2

the properties of E$_s$ distributions known from previous plots. Sporadic E layers appear preferably during daytime, mainly in the afternoon hours.

During northern winter, two moderate maxima in E$_s$ occurrence are observed on the southern hemisphere. The first, appearing at $30°S-50°S$ at $9-12$ local time, is located further to the south than the second more pronounced maximum that arises between 10 and $30°S$ during afternoon hours. Low sporadic E rates are also observed during the night in the southern hemisphere and in low latitudes of the northern hemisphere where they concentrate on the $12-20$ local time sector. During spring, E$_s$ occurs only during daytime in the low latitudes of both hemispheres. Highest rates are observed in the afternoon with larger occurrence rates in the southern hemisphere. During summer, the sporadic E activity relocates almost completely to the midlatitudes in the northern hemisphere. Furthermore, sporadic E layers are observed over the complete day with strong enhancements between 7 and 20 local time. Similar to southern summer, the strong

maximum is split into two parts. The earlier part, appearing in the late morning, is located further north than the later one in the afternoon. E_s rates diminish to $10-30\%$ during night. Simultaneously, a weak E_s activity is monitored in the low latitudes of the southern hemisphere during $12-20$ local time. The sporadic E distribution during autumn appears to be quite similar to the one in spring. However, the maximum with higher E_s rates is located in the northern hemisphere. The structure in midlatitudes, including two minima and two maxima, indicates coupling processes especially the the semidiurnal tide. Further studies are exemplarily performed in comparison with wind measurements from MR Collm (Chapter 7.2).

Similar to the features observed in the plots presented earlier in this chapter, the latitude versus local time cross–sections show principally the same structures in the years 2007 and 2008. The noted properties and differences are also visible in the Figures 6.6 and 6.7 including the stronger spring E_s rates in 2007 compared to 2008, the stronger autumn values in 2008 in the northern hemisphere and the slightly higher sporadic E rates during summer 2008.

An interesting feature appears in the latitude–local time cross–sections. Sporadic E rates show an additional weak maximum in polar latitudes during evening hours. It is present with varying intensity in all seasons of the years 2007 and 2008. Relatively high sporadic E rates in northern polar latitudes are also reproduced in Figure 6.3 concentrating on winter 2004 / 2005 and summer 2006. The southern polar region, however, is free of such E_s events. Consulting also Figure 6.4 and 6.7 it can be recognised that polar sporadic E layers are found in a relatively low altitude range between 90 and 105 km.

Figure 6.8 contains the geographic distribution of the 2008 sporadic E events in the northern polar region. Only data collected between 18 and 23 local time are considered. Enhanced E_s rates form an ellipse that follows the auroral oval. In the literature, polar sporadic E layers are ascribed to auroral events (Maehlum, 1962) that appear preferably during premidnight hours as well.

Obviously, the process responsible for sporadic E formation at polar latitudes is different from the one at midlatitudes. Electric fields become too strong in the polar cusp regions and cannot be neglected as in midlatitudes (Equation (2.2)) because they weaken the wind shear mechanism (Nygren et al., 1984). Furthermore, not the meteors and their evaporated metallic ions are the basis for sporadic E layers in polar regions. Rather particle influx originating directly from solar wind or from the plasma tail are responsible for high ionisation rates in the polar ionosphere. Yet, electron precipitation alone is not capable to produce thin layers of enhanced electron density. Therefore, a special con-
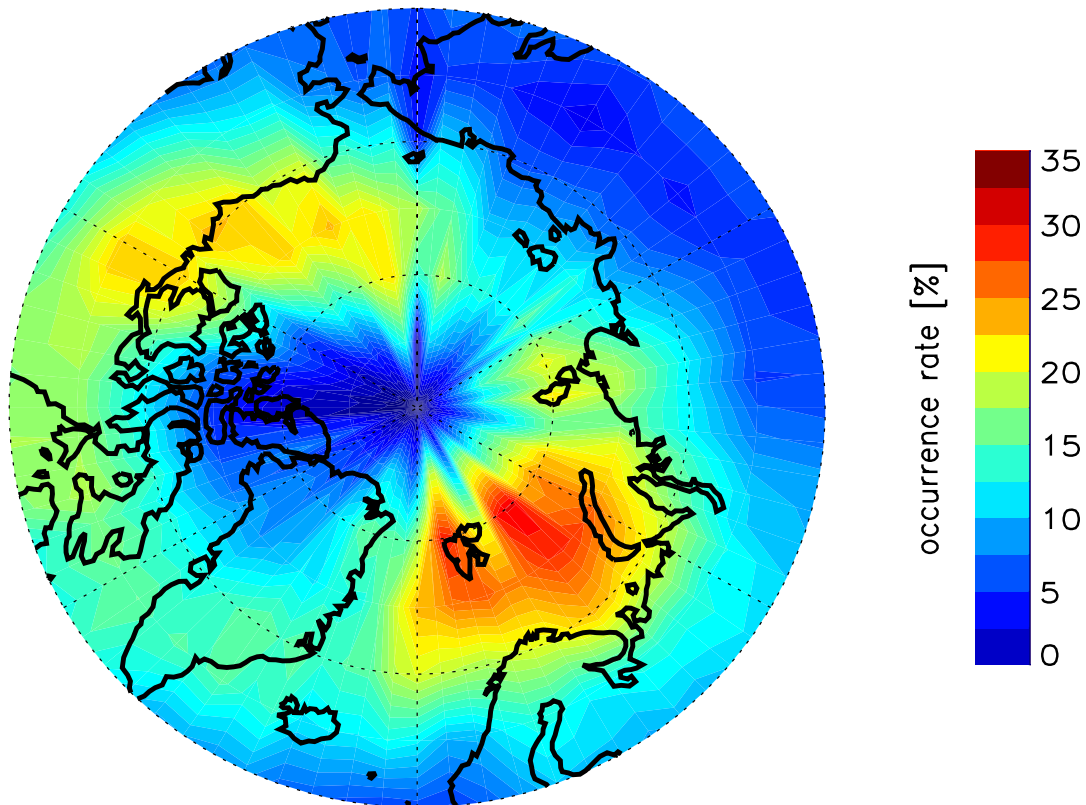
Figure 6.8: Distribution of sporadic E in northern polar latitudes for premidnight hours based on CHAMP, GRACE, and COSMIC RO measurements taken in the year 2008.

verging agent is needed. MacDougall and Jayachandran (2005) proposed a two–step mechanism for E_s formation in cusp latitudes. First, auroral zone electric fields seem to be strong enough to rearrange the electrons and ions into thin patterns. They typically point northward in the evening hours turning southward during night. If the electric field points in northwest direction, it leads to a horizontal convergent plasma flow. Then, the relatively thick layers are rearranged by the polar cap dusk–to–dawn electric field leading to a vertical convergence of ionisation concentrations into narrow layers.

In summary, the global sporadic E distribution shows an annual cycle with highest E_s occurrence rates in the respective summer hemisphere and distinct minima during winter. However, the cycle is not exactly sun–synchronous. The E_s occurrence cycle is delayed compared to solar seasons. It becomes obvious in the equinox seasons when the vernal hemisphere shows always lower sporadic E rates than the autumnal hemisphere.

The structure of high E_s rates in local time distributions in midlatitudes suggests the dependence of sporadic E layer formation on MLT dynamics as it is also proposed in the

wind shear theory. The dominating patterns in MLT winds are tides and especially the semidiurnal tide shows large amplitudes in midlatitudes.

Chapter 7

Geophysical parameters influencing sporadic E occurrence characteristics

This chapter explores the origin of the strong variations of sporadic E occurrence observed on different temporal and spatial scales. According to theory, these variations may result from coupling processes between the E region ionosphere and other geophysical parameters.

For sporadic E formation, several components have to work together:

1. Long–lived metallic ions originating from meteors evaporating in Earth's atmosphere are essential for E_s formation. Their daily number show a characteristical annual cycle (Figure 2.3).

2. The mechanism that seems to be most effective to compress the metallic ions into thin layers is based on wind shears produced by tidal winds in low and midlatitudes.

3. The global E_s distribution and the wind shear theory imply that Earth's magnetic field and especially its horizontal intensity plays an important role in E_s formation and its global distribution.

The sporadic E occurrence is presented in connection with the just mentioned parameters. For the comparison of E_s with tidal winds and meteor rates the focus is set to northern midlatitudes. For a case study, E_s rates from GPS RO measurements are compared to co–locating MR winds and meteor rates. The analysis of E_s in association with Earth's magnetic field is based on global data.
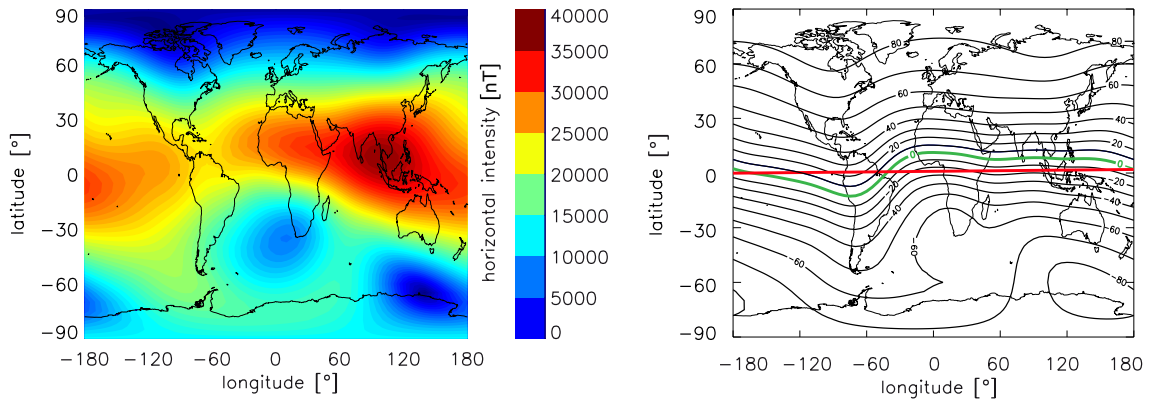
Figure 7.1: Parameters of Earth's magnetic field calculated with the IGRF model representing 2007 conditions; (left) horizontal intensity of the magnetic field, (right) the magnetic inclination. The geographic equator is indicated as a red line. The dip equator is plotted in green.

7.1 Earth's magnetic field

The clear visibility of the magnetic equator in global sporadic E maps (cf. Figure 6.1 and 6.2) as well as the low E_s rates over the South Atlantic region triggered the investigation of a possible connection between E_s occurrence and Earth's magnetic field represented by the International Geomagnetic Reference Field (IGRF). Magnetic field values are calculated using the 10th version of the model released in 2004 (Macmillan and Maus, 2005). In the following, the applied IGRF data represent year 2007 conditions.

The plots in Figure 7.1 show global maps of Earth's magnetic field. Its horizontal intensity (B_{hori}) is displayed on the left, while the right image shows the inclination *I*. These components are closely related to each other via:

$$B_{hori} = B_0 \cos I, \tag{7.1}$$

where B_0 denotes the total intensity of Earth's magnetic field. It is visible in the left part of Figure 7.1 that large B_{hori} values are located in lower latitudes with a strong maximum over southeast Asia. The horizontal intensity decreases quickly poleward. Remarkably low B_{hori} values are found in the South Atlantic and Southern African region. This phenomenon is called South Atlantic Anomaly (SAA). Even the magnetic inclination shows atypically high values in this area (cf. Figure 7.1). Generally, the geomagnetic latitude does not exactly follow the geographic one. For example, the geographic equator (indicated in red) is intersected twice by the dip equator (indicated in green) and by both the 20°S and 20°N isoline of magnetic field's inclination. This fact reflects the wave–like
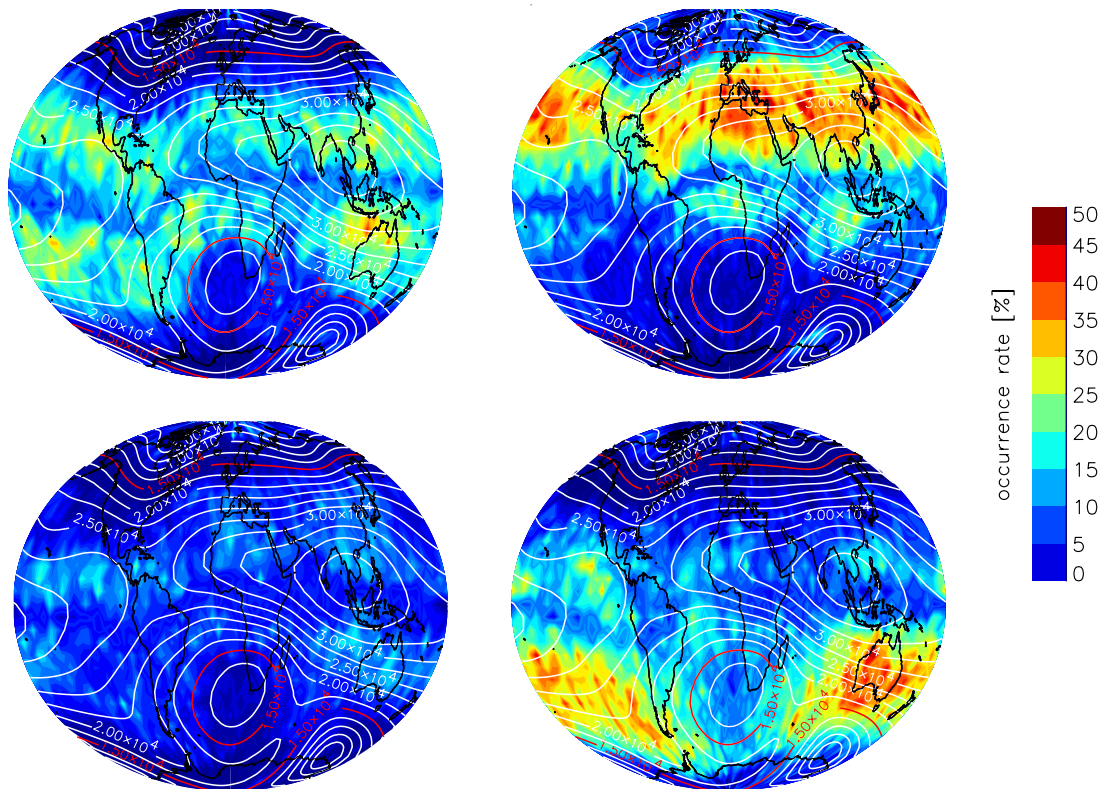
Figure 7.2: Global maps of sporadic E occurrence rates for four different seasons. The upper panel includes spring 2007 (left) and summer 2007 (right) and the lower panel shows the conditions during autumn 2007 (left) and winter 2006/2007 (right). The horizontal intensity of Earth's magnetic field is added as white isolines. The red isoline remarks the course of the $1.5 \cdot 10^4$ nT horizontal intensity.

structure that the magnetic field shows in comparison to geographic latitudes.

According to theory, sporadic E formation depends on the horizontal component of Earth's magnetic field since the formula for the vertical movement of ions (cf. Equation (2.4)) includes the term $B_0 \cos I$. Therefore, focus is set on the comparison of E_s occurrence in association with B_{hori} values in the following. In Figure 7.2, the seasonal E_s maps for the year 2007 are complemented by B_{hori} values marked as white isolines. A qualitative direct correlation between E_s rates and B_{hori} is found. In regions with high horizontal intensities, e.g. Southeast Asia (summer 2007) or Australia (winter 2006/2007), also large E_s occurrences rates are found. This fact explains the relatively high sporadic E rates observed in Patagonia and the northern boundary of Antarctica (northern winter conditions). This area belongs to geographic high latitudes, where usually E_s formation is very sparse and different processes apart from the wind shear mechanism are responsible for E_s formation. However, the horizontal intensity and the inclination favour E_s formation
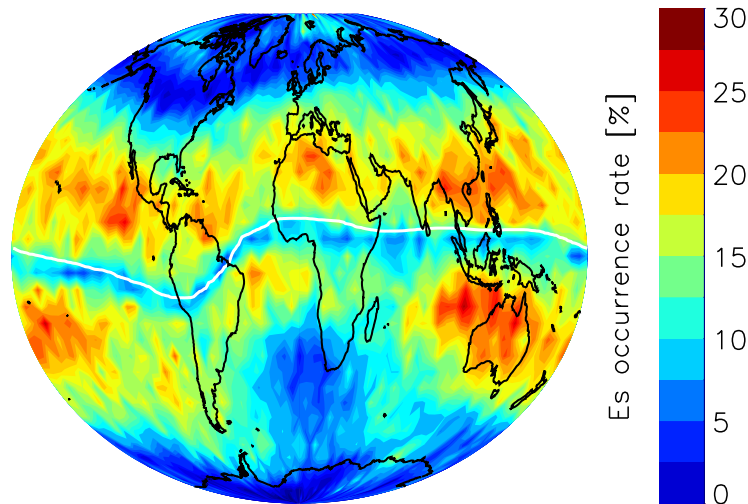
Figure 7.3: Global map of sporadic E rates observed with COSMIC during the year 2007. The white line represents the course of the dip equator.

here. In areas with low horizontal intensity, also E_s rates are usually small. Nearly no sporadic E events are observed in the vicinity of the SAA. Obviously, the $1.5 \cdot 10^4$ nT in the horizontal magnetic field intensity appears as a lower limit, because only few E_s events are observed in regions with smaller B_{hori} values. It can be detected in both near the SAA region (especially during southern summer) and in the northern hemisphere (in northern summer) where the E_s rates follow apparently the wave–like structure of the B_{hori} iso-lines. However, there is no convincing explanation yet why sporadic E layers only appear in regions with B_{hori} larger than approximately $1.5 \cdot 10^4$ nT.

Furthermore, very weak sporadic E activity is observed in the equatorial region. The narrow band of low E_s activity follows directly the course of the magnetic dip equator (cf. Figure 7.3) indicated with a white line. The E_s rates in Figure 7.3 are based on one year COSMIC measurements. Although the E_s occurrence is only given in a spatial resolution of $5° \times 5°$, the narrow band of low rates is clearly visible. The missing of sporadic E is attributed to the strong magnetisation of electrons near the dip equator (Kelley, 1989). The electrons are confined to magnetic field lines that are exactly horizontal along the equator. Therefore, they are not able to follow converging ions moving with neutral winds. As a consequence, a large electric field would build up prohibiting the E_s formation process. However, there are reports on sporadic E observations near the dip equator from ionosonde soundings (e.g. Smith and Matsushita, 1962; Closs, 1970). They were named q–type sporadic E layers and are characterised by producing only very weak radio echoes. Whitehead (1963) summarised the theory of q–type sporadic E formation and the main properties of these layers.
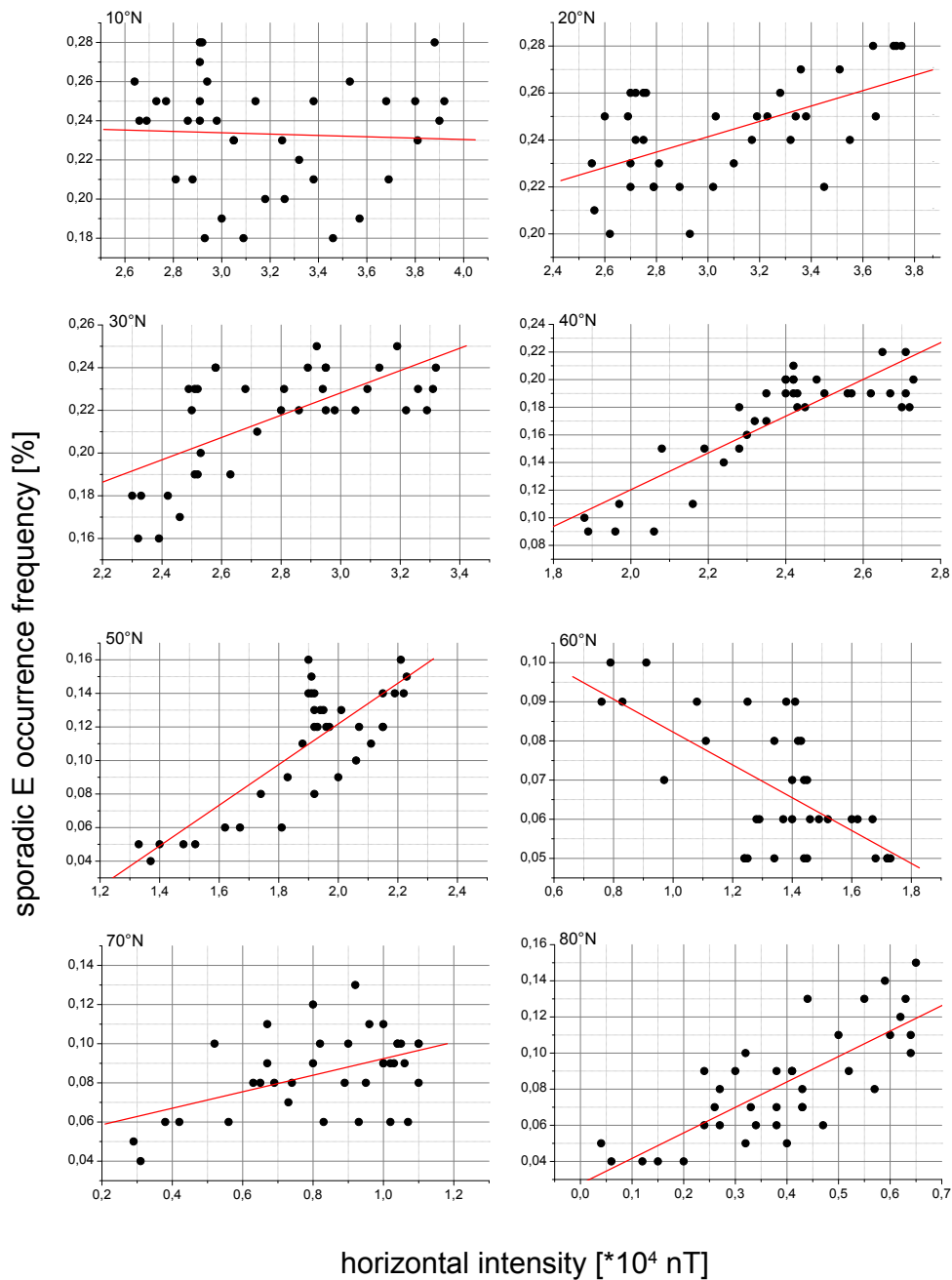
Figure 7.4: Correlation plots of sporadic E occurrence derived from COSMIC RO measurements during 2007 versus horizontal intensity of Earth's magnetic field for the northern hemisphere for different latitude bands. Note the varying scaling.
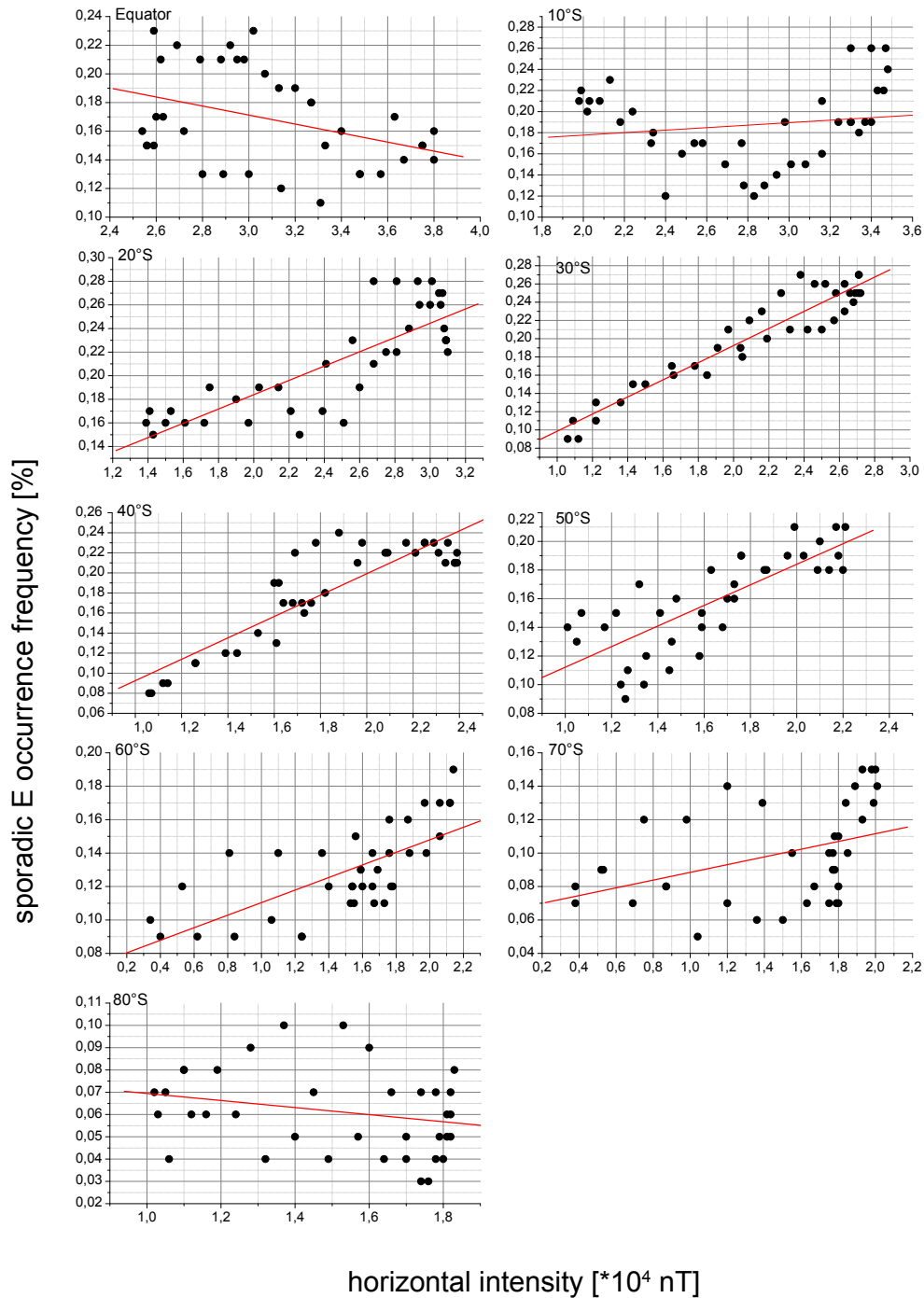
Figure 7.5: Same as Figure 7.4 but for the equator and the southern hemisphere. Note the different scaling.

Latitude	Y $-$ intercept A	Slope B	Correlation R
80°S	0.09	- 0.02	- 0.25
70°S	0.07	0.02	0.41
60°S	0.07	0.04	0.69
50°S	0.04	0.07	0.78
40°S	-0.01	0.11	0.89
30°S	0.00	0.11	0.95
20°S	0.06	0.06	0.82
10°S	0.15	0.01	0.16
0°	0.27	- 0.03	- 0.37
10°N	0.24	- 0.003	- 0.05
20°N	0.14	0.03	0.57
30°N	0.07	0.05	0.65
40°N	-0.14	0.13	0.85
50°N	-0.12	0.12	0.81
60°N	0.12	- 0.04	- 0.67
70°N	0.05	0.04	0.48
80°N	0.03	0.14	0.78

Table 7.1: Parameters of linear regression lines in Figure 7.4 and 7.5. The lines are given in the form $Y = A + BX$. The coefficient R represents the correlation between the horizontal intensity of Earth's magnetic field and sporadic E occurrence.

It was found that equatorial E_s is not the result of an instability process but it forms from wave–like irregularities in the electron density of the equatorial electrojet. Whitehead (1963) reported further that q–type layers occur in low altitudes around $95 - 105$ km. This feature is also reproduced in E_s detection from RO measurements (cf. Figure 6.4 and 6.5). The few E_s events present in the equatorial region are detected at lower altitudes, mainly between 95 and 105 km, compared to midlatitudes.

The obvious correlation between E_s rates and the horizontal intensity of Earth's magnetic field in Figure 7.2 is investigated in more detail in the following. Accordingly, E_s rates from COSMIC RO measurements during the year 2007 are plotted versus the horizontal intensity between 80°S and 80°N. Each plot in Figure 7.4 and 7.5 refers to a latitude band of 10° width. A linear regression analysis is performed for each latitude band and the resulting regression lines are added in the plots. The parameters of the regression lines are summarised in Table 7.1.

Generally, the expected positive correlations are found in midlatitudes in both hemispheres with values of up to 95 % in 30°S and slightly higher correlations in the southern hemisphere. Along the geographic equator, in 10°S and 10°N, no clear tendency of the regression line is visible. It might be due to the vicinity of the magnetic equator where the E_s formation process does not follow the wind shear mechanism and are thus not oblig-

atory correlated with the horizontal intensity. At midlatitudes, high correlations between both parameters are found with values between 70 and 95 %. In 60°N, the correlation suddenly reverses to -67 %. Possibly, E_s formation is already influenced by the polar ionosphere in this latitude region. In polar latitudes, the sporadic E formation does also not primarily depend on B_{hori} but rather on large electric fields (Nygren et al., 1984). For the sake of completeness, correlation plots for the polar regions are displayed although no direct connection between both components is expected. Nevertheless, in 60°S a positive correlation of nearly 70 % can be found. This may be a result of the shape of Earth's magnetic field. On a circle at 60°S geographic latitude one passes 50°S magnetic latitude, the SAA as well as approximately the magnetic pole on the southern hemisphere. There is a large span in B_{hori} values reaching from $0.2 \cdot 10^4$ nT to $2.2 \cdot 10^4$ nT. No clear assignment of this region to midlatitudes or polar latitudes is possible.

7.2   Atmospheric Tides

According to the wind shear theory, sporadic E layer formation depends on vertical wind shears. Atmospheric tides produce considerably stronger shears than the background circulation. Tides, especially the semidiurnal and the diurnal components, are by far the strongest oscillations within the lower thermosphere. The highest amplitudes of the diurnal tide are found at lower latitudes, while the semidiurnal shows stronger activity in higher midlatitudes (e.g. Pancheva et al., 2002). Tidal amplitudes may reach values of more than 40 m/s (Manson et al., 2002a; Jacobi et al., 2009). Therefore, it is expected that the daily variations in E_s occurrence and its height dependency may result from changes in the MLT wind field caused by atmospheric tides. In the following the correlation between tidal winds and E_s occurrence are qualitatively investigated. Hereby, the focus is set to measurements performed by the meteor radar located at the Collm observatory (51.3°N, 13.0°E).

The MR technique is based on accurate measurements of the Doppler shift of radar signals reflected from ionised meteor trails. The method is described in detail by Hocking et al. (2001). The Collm meteor radar operates at a frequency of 36.2 MHz and enables temperature and wind measurements in the altitude range between 80 and 100 km above ground (Jacobi et al., 2007). The single measurements are classified into six height intervals centered at 82 km, 85 km, 88 km, 91 km, 94 km and 98 km. Hourly means of the zonal and meridional winds are calculated for further investigations. Unfortunately, the MR measurements only reach altitudes of about 100 km located just below of the preferred sporadic E range.

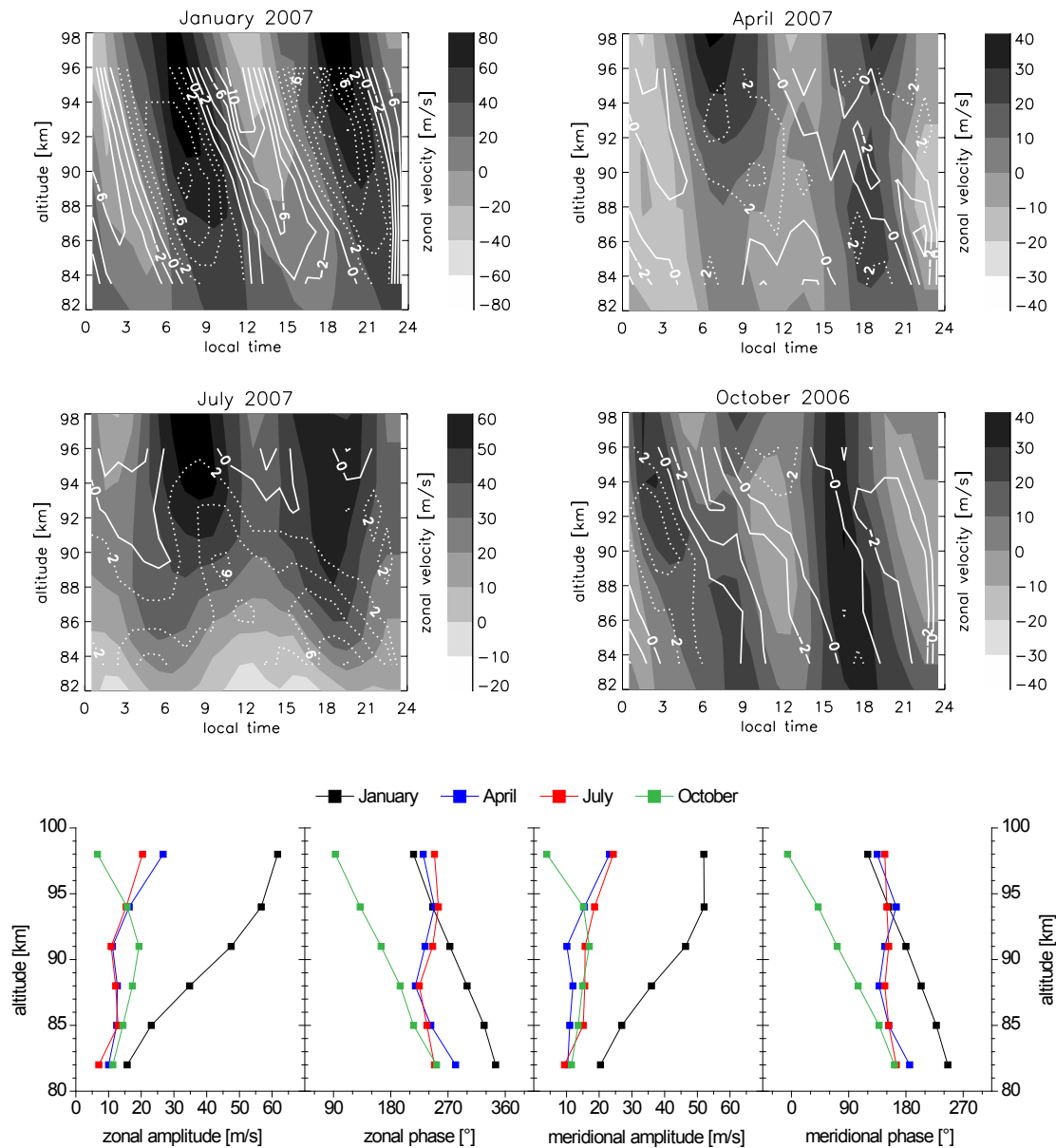**Figure 7.6:** Monthly mean winds measured with the meteor radar at Collm (black−white coded) for four different seasons in 2007. In the upper and middle panels the white isolines indicate the zonal wind shears. Positive shears are indicated with dotted isolines and negative shears with solid ones. The lower panels represent amplitudes and phases of the zonal and meridional semidiurnal tide, respectively.

In the following, plots of monthly means of hourly horizontal winds are presented. In Figure 7.6 zonal winds are shown in the upper and middle panel describing the conditions for October 2006 and January, April, July 2007. Wind shears, S, are simply calculated via:

$$S = \Delta U / \Delta z, \qquad\qquad (7.2)$$

where ΔU represents the change of the zonal wind velocity between the center of two adjacent height intervals. This vertical distance is described by Δz. The zonal wind shears are additionally displayed as white isolines in the upper and middle panel of Figure 7.6. Solid lines represent negative, dashed lines positive wind shears.

The SDT is obviously the dominating feature of the northern midlatitude MLT wind field during the whole year. The most distinct semidiurnal structure in the zonal wind is found in winter with two large maxima and minima during the day. Corresponding large negative wind shears are found in the early morning and afternoon hours. During the other months, the semidiurnal structure is also clearly recognisable, but it is not as dominating as during winter which is attributed to smaller SDT amplitudes. Negative wind shears are therefore very weak during April and October compared to January. In summer, negative values are only found above ~ 90 km due to the increase of vertical zonal wind gradients. In the lower panel of Figure 7.6, the SDT amplitudes and phases of the zonal (left) and meridional (right) oscillations are displayed. These components are calculated by fitting monthly mean winds, SDT, DT, and terdiurnal tidal oscillations to one month of individual hourly data for each height interval. Maximum amplitudes of the SDT appear in winter. In summer, large amplitudes are only found at higher altitudes. This behaviour of the SDT is well known from available climatologies (e.g. Manson et al., 2002b; Kürschner and Jacobi, 2005).

The phases of an oscillation are defined as the time of the maximum amplitude appearance and are given in degrees. The profiles of the phases can be used to derive the vertical wavelength of the SDT. In January and October the vertical wave lengths are about 40 km but in April and July they are very long and can therefore not be estimated from this figure.

Following the wind shear theory, it is expected that sporadic E layers appear in zones of negative zonal wind shear. Thus, Figure 7.7 compares the wind shears with the altitude $-$ local time dependent sporadic E occurrence. The sporadic E rates are based on seasonal mean CHAMP, GRACE and COSMIC E_s rates, that are centered around the months of January, April, July 2007 and October 2006, within a latitude range of $50° - 55°$N. The rates are binned into hourly intervals of local time to get a comparable view on the correlation between sporadic E and zonal wind shear. Figure 7.7 shows height $-$ local
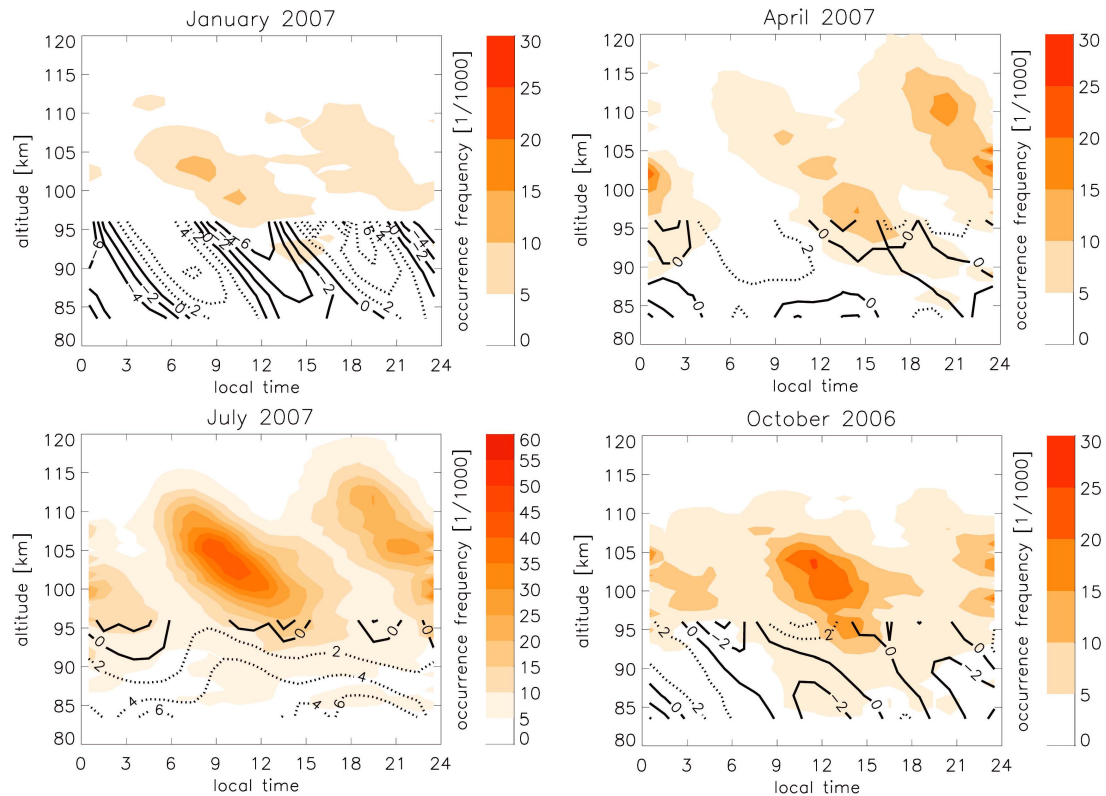
Figure 7.7: Altitude / local time cross–sections of sporadic E rates (red contours) in the latitude range $50°$-$55°$N and zonal wind shears from MR Collm (black isolines). The shears are given in ms^{-1} km^{-1}. Positive shears are indicated with dotted isolines, negative ones with solid isolines. The plots represent the conditions during the period autumn 2006 to summer 2007. Note the different scaling for summer E$_s$ rates compared to the other seasons.

time cross sections of E$_s$ rates (displayed in colour code) in comparison to the zonal wind shears (isolines) taken from Figure 7.6 for four different seasons. The E$_s$ rates are given in 1 / 1000. As expected, the highest E$_s$ probability is found in summer with values of up to 5.6 %. Although the rates are very weak (especially during January), a clear semidiurnal structure is recognisable in all season. Additionally, a descending structure of E$_s$ rates with local time is visible in all panels. During all seasons this descending structure corresponds qualitatively well with the negative wind shears indicated as solid isolines in the lower part of the panels. At first glance, there is an intense contradiction. Strongest wind shears, required for E$_s$ formation, appear in winter whereas the highest sporadic E rates are measured in summer where the shears are distinctly smaller. However, in addition to the vertical zonal wind shears, the meteor rates have to be considered for the correct interpretation of this phenomenon (Haldoupis et al., 2007). It will be discussed in

more detail in Section 7.3.

Further, there is also a diurnal component in the E_s rates in Figure 7.7. During all seasons, one of the two descending maxima is stronger than the other one. Possible influences contributing to this signal could be a diurnal tide in the wind field producing additional wind shears, an increased background ionisation during daytime, and the diurnal cycle of meteor entry (cf. Figure 2.3), which has its maximum in the early morning hours. The latter effect can be widely excluded since the metallic ions produced by meteor influx have lifetimes of more than 24 hours in the MLT region. Therefore they should not show exceedingly high concentrations in the morning. Also the second effect is likely not responsible for the diurnal component in E_s rates because the lifetime of ions produced from air atoms and molecules is too short to be transported by winds. Although the amplitudes of the DT and the corresponding vertical zonal wind shears are for most times of the year comparably small in relation to the SDT ones, DT cannot be excluded unambiguously as an agent for E_s formation in northern higher midlatitudes. During autumn, also the terdiurnal tide reaches significant amplitudes (Beldon et al., 2006). Nevertheless, the focus is set to the SDT because the effect of the DT and the terdiurnal tide are relatively small. Figure 7.8 shows the resulting phases of a least square fit of a $12-$hour sinusoidal oscillation, SDT, to the E_s and wind shear data. The phases are defined here as the local time of maximal E_s occurrence and, in contrast to the typical convention, as the local time when the minimum value in zonal wind shear is reached. For the semidiurnal E_s probability, the phases are highlighted which are significant according to a $t-$test. Significant SDT structures are usually found in the upper altitude range. However, in lower altitudes and during winter, where E_s rates are low anyway, there is only a weak SDT component. Therefore, there is no clear overlapping height interval between the wind shear and E_s phase profiles in three of four seasons. But if the wind shear phase is extrapolated linearly to larger altitudes, they fit well to the E_s phases again. Thus, a strong qualitative correlation between both phases is found during the year, even if insignificant E_s phases are included in the visual inspection. Only in October a discrepancy between both phases is found at lower altitudes. This is due to the very low sporadic E rates there.

Over the course of the day the phases show a descending structure. It is known from theory and ground based observations (Haldoupis et al., 2006) and Christakis et al. (2009) that the descent of the sporadic E layers follows the phase velocity of the the SDT convergent node at altitudes above about 100 km. Below, the descent velocity slows down due to enhanced ion–neutral collision frequencies. This phenomenon is only weakly visible in July (cf. Figure 7.7 and 7.8) where the E_s rate slope is weakly bent below about 95 km. During all other months constant slopes are observed at lower altitudes. This could result
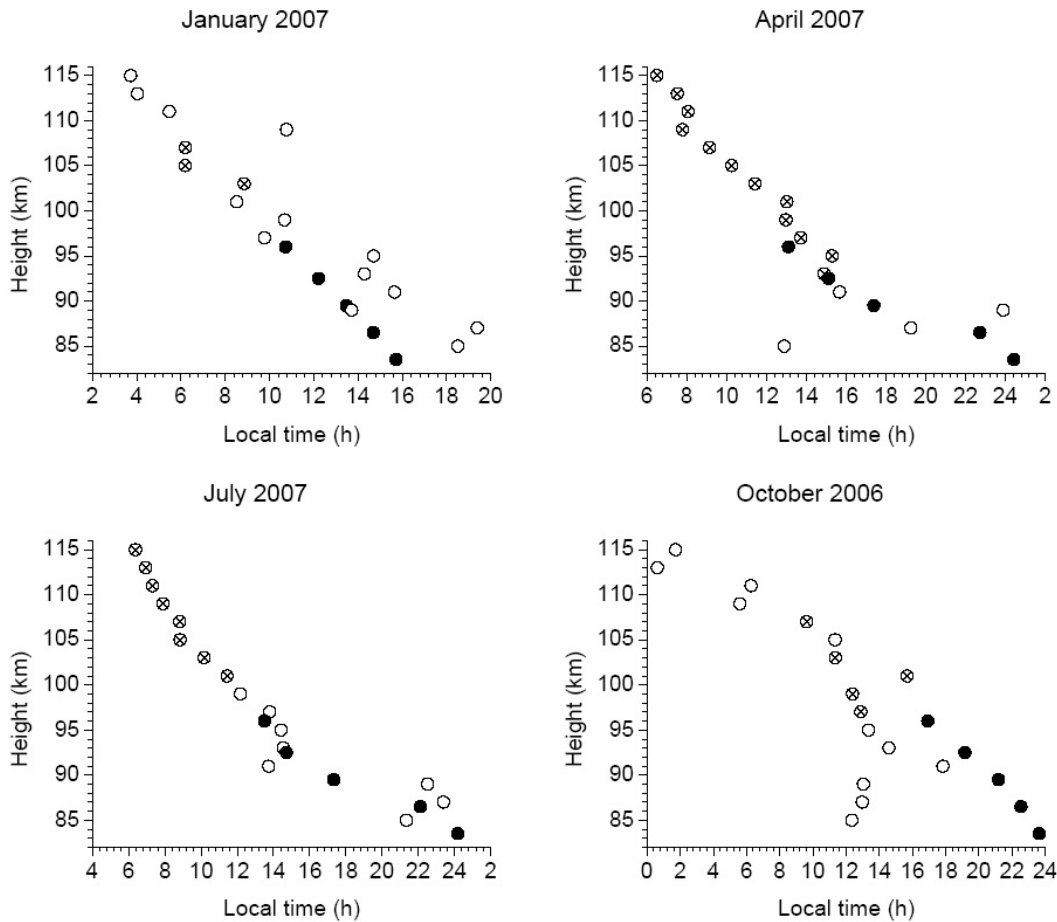
Figure 7.8: Phases of the zonal SDT component from MR measurements (solid dots) in comparison to the time of maximum sporadic E occurrence marked as circles. In those altitudes where semidiurnal E_s occurrence is significant according to a $t-$test, the circles are marked with a cross.

from the observation of E_s with the RO method which does not allow for the observation of the behaviour of a single E_s layer but for quarterly means in the latitude range between $50°$ and $55°$N. Fine structures are therefore not present in the available RO data set. Accordingly, only a qualitative correspondence between sporadic E and the SDT phase decent is found.

The descent of the SDT components of E_s rates are calculated from a linear fit of the significant points in Figure 7.8. Values of 2.2 km/h, 2.4 km/h, 2.5 km/h and 1.5 km/h in January, April, July and October are obtained, respectively. In comparison, the SDT wind shear gradients reach 2.5 km/h, 1.0 km/h, 1.1 km/h and 1.8 km/h in January, April, July 2007 and October 2006. In January and October, the descent rates reach similar values.

The E_s descent is only slightly smaller. It could be attributed to the fact that at lower altitudes E_s formation becomes too slow to remain inside the convergence zone (Haldoupis et al., 2006). In April and July, the mechanism is more complex. The descent speeds of both E_s and wind shears are much smaller compared to SDT winds (Figure 7.6). This is caused by the fact that the vertical wind shear depends not only on the wave phase but also on the amplitude growth with height. In summer, the SDT amplitude often decreases with height. Thus, the wind shear phase gradient is stronger (negative) than the wind phase gradient.

In general, sporadic E layers appear preferably in regions of negative vertical zonal wind shear. Since the semidiurnal tide is the dominating oscillation in northern midlatitudes, the E_s occurrence rates show a semidiurnal structure. Obviously, weak negative wind shears are strong enough for E_s formation and wind shears alone do not explain the annual cycle of sporadic E occurrence. Over the course of the day the E_s rates follow the descending SDT negative wind shear node that causes the two descending sporadic E rate maxima during the whole year (Figure 7.7).

7.3   Metallic ions in the Mesosphere and Lower Thermosphere region

Metallic ions in lower ionospheric altitudes are deposited by meteoroids evaporating in Earth's atmosphere. The metallic ion concentration in lower ionospheric altitudes is thus dependent on the intensity of the meteor influx. The meteor influx shows a clear seasonal cycle displayed in Figure 7.9 (blue). The plot is based on daily meteor numbers detected with the MR Collm during the year 2007 covering the altitude range between 80 and 100 km. Strong annual variations in the daily meteor counts are observed with largest values detected in June, July and August and lowest rates in February and March. After passing the winter minimum, the meteor rates increase steeply to the summer maximum. The summer rates are about twice as high compared to the winter months. But the summer rates decrease less abruptly during the autumn months. This behaviour leads to an asymmetric course during the year. In January and December, two sharp peaks occur. They can be attributed to the strong meteor showers called Quadrantids (January) and Geminids (December).

Because sporadic E layers consist mainly of metallic ions, it is not surprising that the course of the daily E_s rates is, in general, similar to the one of the meteor rates. A qualitative comparison between daily meteor rates and daily E_s rates (red line) is displayed
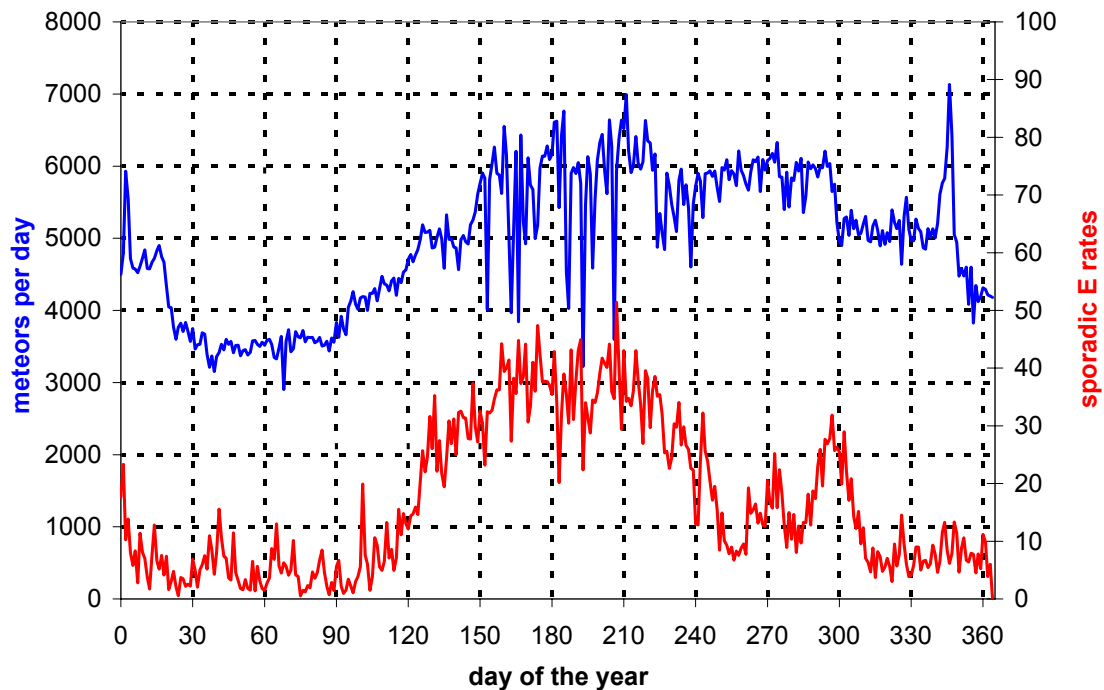
Figure 7.9: Annual cycle of daily meteor rates (blue) measured with the Collm meteor radar and sporadic E rates (red) based on COSMIC RO measurements at northern mid-latitudes ($50° - 55°$N) during the year 2007.

in Figure 7.9. The E_s rates are based on COSMIC RO measurements performed during the year 2007 in a latitude band between $50°$N and $55°$N. Analogue to meteor rates, the lowest values in E_s occurrence is observed in February and March. In spring, they suddenly increase to the maximum rates in June, July and August. Afterwards, they decrease quickly in September but showing a secondary maximum at the end of October. Nevertheless, the annual cycle of E_s occurrence is more symmetric than the one of the meteor rates. The winter minimum is also time–shifted compared to the solar annual cycle by about two month. Both curves show the steep increase in spring and the maximum rates during the whole summer. However, at the end of August the courses of both curves differ from each other. The meteor rates are still high during September and October while the E_s rates behave differently.

In order to explain this phenomenon, we have to consider again the vertical zonal wind shears. For that reason, the zonal vertical wind shear based on the WINDII (WIND Imaging Interferometer) climatology are displayed in Figure 7.10 (Zhang et al., 2007). Unfortunately, the WINDII climatology provides only data for lower latitudes confining the comparison to the latitude band $40-45°$N. As a second disadvantage, the WINDII data
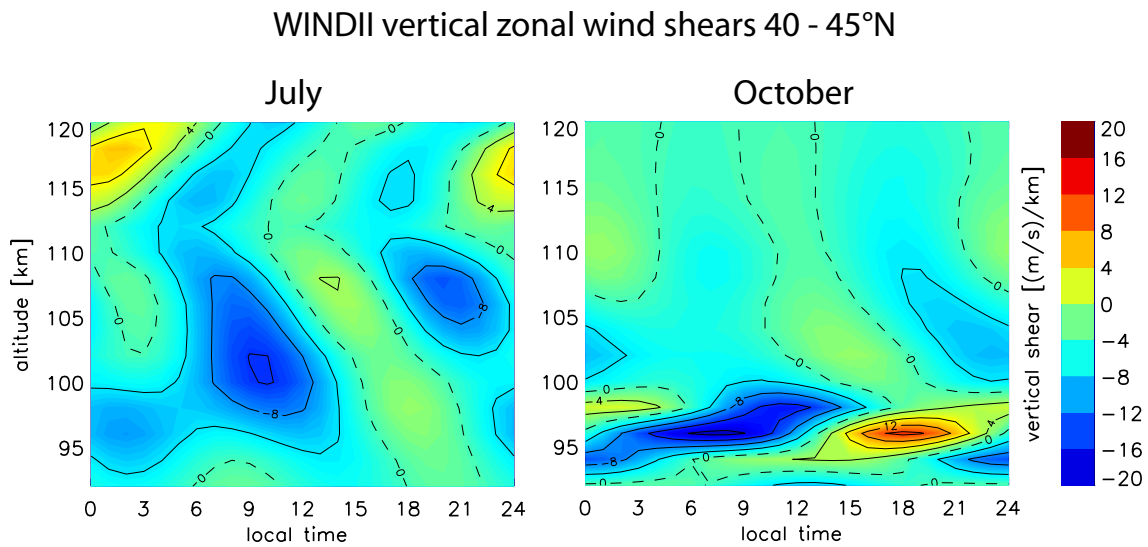
Figure 7.10: Vertical zonal wind shears based on the WINDII climatology at $40° - 45°$N for July (left) and October (right).

comprise of measurements taken in the early 1990's where different atmospheric conditions prevailed in compared to the investigated sporadic E and meteor time series. But these data give an overview and provide information on the wind conditions at altitudes between 100 and 120 km not available from ground based measurements. The strongest shears are observed below 100 km in autumn. Above, the shears weaken quickly. In summer, the situation changes. The negative zonal wind shears reach smaller absolute values than in summer. They are present during the complete height range and are strong enough to compress the metallic ions into thin E_s layers. In contrast, the shears are hardly present in autumn. Although during October the meteor rates are as high as during July, the missing wind shear prevents sporadic E formation and the E_s rates show generally a decreasing course in the autumn months.

Chapter 8

Summary and conclusions

This study is based on GPS radio occultation measurements performed by the low–Earth orbiting satellites CHAMP, GRACE, and FORMOSAT–3 / COSMIC between 2001 and 2008. These satellites provide in total up to 2 500 globally distributed profiles per day of electron density in the ionosphere and of density, temperature and water vapour content in the lower neutral atmosphere. The profiles have a very high vertical resolution of several meters and therefore enable the detection of vertically small structures in Earth's atmosphere and ionosphere. One of them are sporadic E layers which are the main topic of this thesis.

The number of daily GPS RO measurements, their global distribution, and the high vertical resolution of the profiles are an excellent basis to investigate the lower ionosphere on a global scale. For the first time, data supplied by an ensemble of satellites are used to receive a global and comprehensive picture of sporadic E layer occurrence and the associated coupling process between the neutral atmosphere and ionosphere. Sporadic E layers are phenomena of the lower ionospheric E region that appear as thin sheets of enhanced electron density. They occur mainly in the midlatitudes of the summer hemisphere in the altitude range between 95 and 120 km. Sporadic E layers are characterised by strong vertical electron density gradients due to their enhanced electron density compared to the background ionisation.

GPS–based radio occultations exploit signals received onboard LEO satellites for atmospheric limb sounding. The GPS signals are influenced by the atmospheric refractivity field resulting in a time delay and bending of the signals. The GPS signals are sensitive to strong gradients in the electron density and are considerably disturbed when propagating though them. This fact is used to extract the signature of an E_s layer from the RO profile by analysing the SNR of the GPS L_1 signal. The empirical detection procedure is based on several assumptions. Thus, the detection algorithm and resulting sporadic E altitudes

were validated subsequently by applying two validation processes.

In the first step of the validation it is investigated how the GPS signals are modified when propagating through the various ionospheric layers by using the Multiple Phase Screen method. Within this model, the atmosphere is divided into a series of phase screens. At the single phase screens, the GPS signal is modified due to the present electron density. Between the screens, the waves travel as if in vacuum. With this method it is demonstrated that strong variations in GPS signals can be attributed to sporadic E layers. Subsequently, sporadic E altitudes, revealed from RO measurements, were compared with those detected from ionosonde soundings in Juliusruh (54°N, 13°E), Germany. A good correlation of $\sim 90\,\%$ was determined from coinciding sporadic E altitude measurements of both techniques.

The sporadic E climatology shows that E_s occurrence is subject to variations on several time scales. The observed daily fluctuations with higher rates during daytime and lower rates at night are interfered by an annual cycle with the largest values measured in summer. The variations are caused by geophysical parameters controlling the sporadic E formation. The interaction of these parameters, namely the concentration of metallic ions in the lower ionosphere, the horizontal intensity of Earth's magnetic field, and vertical wind shears, is summarised in the wind shear theory that describes the E_s formation process in midlatitudes.

Accordingly, the observed E_s rates are associated to these geophysical parameters in more detail. It is shown that Earth's magnetic field and especially its horizontal intensity is responsible for the global arrangement of E_s layers. Correlation analysis between both parameters were performed for the first time. They reveal that sporadic E formation depends directly on the horizontal intensity of Earth's magnetic field. Correlations are extremely high at midlatitudes of the southern hemisphere reaching values of up to 95 %. Considering the equatorial latitudes, the dip equator appears as a band of very low E_s activity. In the equatorial region as well as in polar latitudes the sporadic E formation does not follow the wind shear process because electric fields become too large there. It is found that E_s occurrence rates are oriented along the polar oval in northern polar region.

Investigations of coupling processes between E_s and MLT winds were performed in northern midlatitudes. The meteor radar located at Collm Observatory provides wind and meteor rate measurements which were compared with seasonal E_s rates. It is found that the vertical zonal wind shear produced by the semidiurnal tide has the strongest influence on sporadic E behaviour in northern midlatitudes. On seasonal average, E_s rates show a clear semidiurnal structure in altitude / local time cross–sections throughout the year

following the downward moving phase of the tidal wind shear.

The ion concentration in the ionosphere depends on the meteor influx reaching its maximum in early summer. In the first half of the year, daily E_s rates follow very closely the course of the daily meteor number. But the differences observed in the second half of the year can only be explained when taking into account additionally the wind conditions.

Returning to the introductory questions, we can now provocatively conclude that sporadic E layers do not appear sporadically. They follow distinct regularities and occur frequently under the convenient interaction of tidal winds, metallic ion concentration, and Earth's magnetic field. At this point we cannot say which parameter is most influencing E_s formation, because a comprehensive part of this work concentrates on northern midlatitudes. Further, it is also not possible to draw an inverse conclusion on tidal winds from E_s occurrence. We have seen that very weak wind shears appearing in spring or autumn are sufficient for E_s formation. We may speculate that the strength of the shear is influencing the intensity of the sporadic E layers and the accompanying electron density maximum. Unfortunately, this parameter is not available from SNR measurements from GPS RO data.

Most likely, additional parameters contribute to E_s formation. For instance, the relatively strong variation of global E_s occurrence in spring and autumn leads to the assumption of additional controlling parameters. It will be future work to identify them. Apart from that, we cannot yet explain the large variations in the inter–annual E_s occurrence.

The correlation of sporadic E rates with the horizontal intensity of Earth's magnetic field raises further questions: Why does the $1.5 \cdot 10^4$ nT isoline appear as a limit where nearly no E_s events are observed below it? And why do we observe sporadic E layers in the northern polar region following the polar oval but do not find the corresponding feature in the southern polar hemisphere?

Regarding the annual cycle of E_s occurrence, the two peaks in autumn around day 270 and 300 cannot be explained so far. Yet, it can be envisaged that the dynamic conditions during that time play a decisive role since the important wind shears are very weak at higher altitudes during autumn.

With the aggregation of GPS RO data sets in the upcoming years, it will be possible to investigate whether E_s occurrence rates show a dependence on the solar cycle. By using additional GLONASS and Galileo signals in the future, the number of daily radio occultation measurements will increase significantly. Thus, the spatial as well as the temporal resolution of RO profiles will improve. Further, the investigation of small–scale

variations in E_s occurrence and time series of them over a small area will become possible. The knowledge of sporadic E behaviour and its variations is important since they disturb severely GPS and radio communication signals and the use of global navigation and communication will increase in the following years.

This study presented first global sporadic E occurrence in an unprecedented high spatial resolution. It confirms the theoretically predicted coupling processes by comparing sporadic E rates with IGRF model analysis as well as with MLT wind and meteor rate measurements in northern midlatitudes. Thus, this thesis is a valuable contribution to the knowledge of coupling processes between the neutral mesosphere and lower thermosphere region and the lower ionosphere.

Bibliography

Anthes, R. A., Bernhardt, P. A., Chen, Y., Cucurull, K., Dymond, K. F., Ector, S., Healy, S. B., Ho, S.-P., Hunt, D. C., Kuo, Y.-H., Liu, H., Manning, K., McCormick, C., Meehan, T. K., Randel, W. J., Rocken, C., Schreiner, W. S., Sokolovskiy, S. V., Syndergaard, S., Thompson, D. C., Trenberth, K. E., Wee, T.-K., Yen, N. L., and Zhang, Z.: THE COSMIC/FORMOSAT-3 MISSION: Early Results, Bull. Am. Met. Soc., 89,3, 313–333, doi:10.1175/BAMS-89-3-313, 2008.

Arras, C., Wickert, J., Jacobi, C., Heise, S., Beyerle, G., and Schmidt, T.: A global climatology of ionospheric irregularities derived from GPS radio occultation, Geophys. Res. Lett., 35, L14 809, doi:10.1029/2008GL034158, 2008.

Arras, C., Jacobi, C., and Wickert, J.: Semidiurnal tidal signature in sporadic E occurrence rates derived from GPS radio occultation measurements at higher midlatitudes, Ann. Geophys., 27, 2555–2563, 2009.

Arras, C., Jacobi, C., Wickert, J., Heise, S., and Schmidt, T.: Sporadic E signatures revealed from multi-satellite radio occultation measurements, Adv. in Radio Sci., 8, 225–230, 2010.

Baggaley, W. J.: Ionospheric Sporadic-E parameters: Long-term trends, Science, 24, 830–831, 1984.

Beldon, C. L., Muller, H. G., and Mitchell, N. J.: The 8-hour tide in the mesosphere and lower thermosphere over the UK, 1988–2004, J. Atmos. Sol. Terr. Phys., 86, 655–668, 2006.

Beyerle, G., Gorbunov, M. E., and Ao, C. O.: Simulation studies of GPS radio occultation measurements, Radio Science, 38, 5, doi:10.1029/2002RS002800, 2003.

Borries, C., Jakowski, N., and Wilken, V.: Storm induced large scale TIDs observed in GPS derived TEC, Ann. Geophys., 27, 1605–1612, 2009.

Budden, K. G.: The propagation of radio waves: the theory of radio waves of low power in the ionosphere and magnetosphere, Camebridge University Press, 1985.

Christakis, N., Haldoupis, C., Zhou, Q., and Meek, C.: Seasonal variability and descent of mid-latitude sporadic E layers at Arecibo, Ann. Geophys., 27, 923–931, 2009.

Closs, R. L.: Blanketing type sporadic-E associated with the equatorial electrojet, J. Atmos. Terr. Phys., 32, 265–276, 1970.

Craig, R. A.: THE UPPER ATMOSPHERE Meteorology and Physics, Academic Press New York and London, 1965.

de la Torre, A., Schmidt, T., and Wickert, J.: A global analysis of wave potential energy in the lower stratosphere derived from 5 years of GPS radio occultation data with CHAMP, Geophys. Res. Lett., 33, L24 809, doi:$10.1029/2006GL027696$, 2006.

Evans, J. V.: Theory and practice of ionosphere study by Thomson scatter radar, Proc. of the IEEE, 57, 496–530, 1969.

Fjeldbo, G. and Eshleman, V. R.: The atmosphere of Mars analyzed by integral inversion of the Mariner IV occultation data, Planet. Space Sci., 16, 1035–1059, 1968.

Fjeldbo, G., Kliore, A. J., and Eshleman, V. R.: The neutral atmosphere of Venus as studied with Mariner V radio occulation experiment, Astronom. J., 76, 2, 123–140, 1971.

Forbes, J. M., Russell, J., Miyahara, S., Zhang, X., Palo, S., Mlynczak, M., Mertens, C. J., and Hagan, M. E.: Troposphere-thermosphere tidal coupling as measured by the SABER instrument on TIMED during July–September 2002, J. Geophys. Res., 111, A10S06, doi:$10.1029/2005JA011492$, 2006.

From, W. R. and Whitehead, J. D.: On the peculiar shape of sporadic-E clouds, J. Atmos. Terr. Phys., 40, 1025–1028, 1978.

Grebowsky, J. M. and Bilitza, D.: SOUNDING ROCKET DATA BASE OF E- AND D-REGION ION COMPOSITION, Adv. Space Res., 25, 183–192, 2000.

Greenwald, R. A., Baker, K. B., Dudeney, J. R., Pinnock, M., Jones, T. B., Thomas, E. C., Villain, J.-P., Cerisier, J.-C., Senior, C., Hanuise, C., Hunsucker, R. D., Sofko, G., Koehler, J., Nielsen, E., Pellinen, R., Walker, A. D. M., Sato, N., and Yamagishi, H.: DARN/SUPERDARN A global View of the Dynamics of High-Latitude Convection, Space Science Reviewes, 71, 761–796, 1995.

Gurvich, A. S. and Krasilnikova, T. G.: Navigation Satellites for Radio sensing of the Earth's Atmosphere, Sov. J. of Remote Sensing, 7(6), 1124–1131, 1990.

Hagan, M. E. and Forbes, J. M.: Migrating and nonmigrating diurnal tides in the middle and upper atmosphere excited by tropospheric latent heat release, J. Geophys. Res., 107(D24),4754, doi:10.1029/2001JD001236, 2002.

Hagan, M. E. and Forbes, J. M.: Migrating and nonmigrating semidiurnal tides in the upper atmosphere excited by tropospheric latent heat release, J. Geophys. Res., 108(A2), 1062, doi:10.1029/2002JA009466, 2003.

Hajj, G., Kursinski, E., Romans, L., Bertiger, W., and Leroy, S.: A technical description of atmospheric sounding by GPS occultations, J. Atmos. Sol. Terr. Phys., 64, 451–469, 2002.

Hajj, G. A. and Romans, L. J.: Ionospheric electron density profiles obtained with the Global Positioning System: Results from the GPS/MET experiment, Radio Sci., 33, 175–190, 1998.

Hajj, G. A., Ao, C. O., Iijima, B. A., Kuang, D., Kursinski, E. R., Mannucci, A. J., Meehan, T. K., Romans, L. J., de la Torre Juarez, M., and Yunck, T. P.: CHAMP and SAC-C atmospheric occultation results and intercomparisons, J. Geophys. Res., 109, doi:10.1029/2003JD003909, 2004.

Haldoupis, C., Meek, C., Christakis, N., Pancheva, D., and Bourdillon, A.: Ionogram height-time-intensity observations of descending sporadic E layers at mid-latitudes, J. Atmos. Sol. Terr. Phys., 68, 539–557, 2006.

Haldoupis, C., Pancheva, D., Singer, W., Meek, C., and MacDougall, J.: An explanation for the seasonal dependence of midlatitude sporadic E layers, J. Geophys. Res., 112, A06 315, doi:10.1029/2007JA012322, 2007.

Heise, S., Wickert, J., Beyerle, G., Schmidt, T., and Reigber, C.: Global monitoring of tropospheric water vapor with GPS radio occultation aboard CHAMP, Adv. Space Res., 27, 2222–2227, 2006.

Hocke, K., Igarashi, K., Nakamura, M., Wilkinson, P., Wu, J., Pavelyev, A., and Wickert, J.: Global sounding of sporadic E layers by the GPS/MET radio occultation experiment, J. Atmos. Sol. Terr. Phys., 63, 1973–1980, 2001.

Hocking, W. K., Fuller, B., and Vandepeer, B.: Real-time determination of meteor-related parameters utilizing modern digital technology, J. Atmos. Sol. Terr. Phys., 63, 155–169, 2001.

Hofmann-Wellenhof, B., Lichtenegger, H., and Wasle, E.: GNSS Global Navigation Satellite Systems - GPS, GLONASS, Galileo & more, Springer Wien, New York, 2008.

Huang, X. and Reinisch, B.: Vertical electron density profiles from the digisonde network, Adv. Space Res., 18(6), 121–129, 1996.

Jacobi, C., Fröhlich, K., Viehweg, C., Stober, G., and Kürschner, D.: Midlatitude mesosphere/lower thermosphere meridional winds and temperatures measured with Meteor Radar, Adv. Space Res., 39, 1278–1283, 2007.

Jacobi, C., Arras, C., Kürschner, D., Singer, W., Hoffmann, P., and Keuer, D.: Comparison of mesopause region meteor radar winds, medium frequency radar winds and low frequency drifts over Germany, Adv. Space Res., 43, 247–252, 2009.

Jakowski, N.: TEC Monitoring by Using Satellite Positioning Systems, Modern Ionospheric Science, EGS, 1996.

Jakowski, N., Wehrenpfennig, A., Heise, S., Reigber, C., Lühr, H., Grunwaldt, L., and Meehan, T. K.: GPS radio occultation measurements of the ionosphere from CHAMP: Early results, Geophys. Res. Lett., 29(10), 1457, doi:10.1029/2001GL014364, 2002.

Kaplan, E. D. and Hegarty, C., eds.: UNDERSTANDIG GPS PRINCIPLES AND APPLICATION, Artech House, Boston, London, 2006.

Kelley, M. C.: The Earth's Ionosphere: Plasmaphysics and Electrodynamics, Academic Press, Inc. San Diego, 1989.

Kopp, E.: On the abundance of metal ions in the lower ionosphere, J. Geophys. Res., 102, 9667–9674, 1997.

Kraus, H.: Die Atmosphäre der Erde, Eine Einführung in die Meteorologie, Springer-Verlag Berlin, Heidelberg, 2004.

Kürschner, D. and Jacobi, C.: The mesopause region wind field over Central Europe in 2003 and comparison with a long-term climatology, Adv. Space Res., 35, 1981–1986, 2005.

Kursinski, E. R.: THE GPS RADIOOCCULTATION CONCEPT: THEORETICAL PER-FORMANCE AND INITIAL RESULTS, Ph.D. thesis, California Institute of Technology, Pasadena, California, 1997.

Kursinski, E. R., Hajj, G. A., Bertiger, W. I., Leroy, S. S., Meehan, T. K., Romans, L. J., Schofield, J. T., McCleese, D. J., Melbourne, W. G., Thornton, C. L., Yunck, T. P., Eyre, J., and Nagatani, R. N.: Initial Results of Radio Occultation Observations of Earth's Atmosphere Using the Global Positioning System, Science, 271, 1107–1110, 1996.

Kursinski, E. R., Hajj, G., Hardy, K. R., Schofield, J. T., and Linfield, R.: Observing the Earth's atmosphere with radio occultation measurements using the Global Positioning System, J. Geophys. Res., 102, 23 429–23 465, 1997.

Larsen, G. B., Høeg, P., Syndergaard, S., Sørensen, M. B., Grove-Rasmussen, J., and Benzon, H.-H.: Ørsted GPS Atmosphere Profiling Status and Preliminary Results, URSI XXVI General Assembly, Toronto, 1999.

Lei, J., Syndergaard, S., Burns, A. G., Solomon, S. C., Wang, W., Zeng, Z., Roble, R. G., Wu, Q., Kuo, Y.-H., Holt, J. M., Zhang, S.-R., Hysell, D. L., Rodrigues, F. S., and Lin, C. H.: Comparison of COSMIC ionospheric measurements with ground-based observations and model predictions: Preliminary results, J. Geophys. Res., 112, A 07 308, doi:10.1029/2006JA012240, 2007.

Leighton, H. I., Shapley, A. H., and Smith, E. K.: International Series of Monographs on Electromagnetic Waves, chap. The Occurrence of Sporadic E during IGY, pp. 166–177, Pergamon Press, 1962.

Liljequist, G. H. and Cehak, K.: Allgemeine Meteorologie, Friedr. Vieweg & Sohn Verlags-gesellschaft, Braunschweig, Germany, 1984.

Lindal, G. F.: The atmosphere of Neptune: an analysis of radio occulation data acquired with Voyager 2, Astronom. J., 103, 967–982, 1988.

Lindal, G. F., Wood, G. E., Hotz, H. B., Sweetnam, D. N., Eshleman, V., and Tyler, G. L.: The atmosphere of Titan: An analysis of the Voyager 1 radio occultation measure-ments, Icarus, 53, 348–363, 1983.

MacDougall, J. W. and Jayachandran, P. T.: Sporadic E at cusp latitudes, J. Atmos. Sol. Terr. Phys., 67, 1419–1426, 2005.

Macmillan, S. and Maus, S.: International Geomagnetic Reference Field–the tenth gen-eration, Earth Planets Space, 57, 1135–1140, 2005.

Maehlum, B.: Geofysiske publikasjoner, vol. XXIII, chap. The Sporadic E auroral zone, pp. 1–32, 1962.

Maksyutin, S. V., Sherstyukov, O. N., and Fahrutdinova, A. N.: Dependence of sporadic E layer and lower thermosphere dynamics on solar activity, Adv. Space Res., 27, 1265–1270, 2001.

Manson, A. H., Luo, Y., and Meek, C.: Global distribution of diurnal and semi-diurnal tides: observations from HRDI-UARS of the MLT region, Ann. Geophys., 20, 1877–1890, 2002a.

Manson, A. H., Meek, C., Hagan, M., J., K., Franke, S., Fritts, D., Hall, C., Hocking, W., Igarashi, K., MacDougall, J., Riggin, D., and Vincent, R.: Seasonal variations of the semi-diurnal and diurnal tides in the MLT: multi-year MF radar observations from 2-70°N, modelled tides (GSWM, CMAM), Ann. Geophys., 20, 661–677, 2002b.

Mathews, J. D.: Sporadic E: current views and recent progress, J. Atmos. Sol. Terr. Phys., 60, 413–435, 1998.

Mathews, J. D. and Bekeny, F. S.: Upper Atmosperic Tides and the Vertical Motion of Ionospheric Sporadic Layers at Arecibo, J. Geophys. Res., 84, 2743–2750, 1979.

Mc Kinley, D. M.: Meteor Science and Engineering, Graw-Hill Book Company, 1961.

Misra, P. and Enge, P.: GLOBAL POSITIONING SYSTEM Signals, Measurements and Performance, Ganga-Jamuna Press, 2001.

Namboothiri, S. P., Jiang, J. H., Kishore, P., Igarashi, K., Ao, C. O., and Romans, L. J.: CHAMP observations of global gravity wave fields in the troposphere and stratosphere, J. Geophys. Res., 113, D07 102, doi:10.1029/2007JD008912, 2008.

Nygren, T., Jalonen, L., Oksman, J., and Turunen, T.: The role of electric fields and neutral wind direction in the formation of sporadic E-layers, J. Atmos. Terr. Phys., 46, 373–381, 1984.

Pancheva, D., Merzlyakov, E., Mitchell, N. J., Portnyagin, Y., Manson, A. H., Jacobi, C., Meek, C. E., Luo, Y., Clark, R. R., Hocking, W. K., MacDougall, J., Muller, H. G., Kürschner, D., Jones, G. O. L., Vincent, R. A., Reid, I. M., Singer, W., Igarashi, K., Fraser, G. I., Fahrutdinova, A. N., Stephanov, A. M., Poole, L. M. G., Malinga, S. B., Kashcheyev, B. L., and Oleynikov, A. N.: Global-scale tidal variability during the PSMOS campaign of June-August 1999: interaction with planetary waves, J. Atmos. Sol. Terr. Phys., 64, 1865–1896, 2002.

Pancheva, D., Haldoupis, C., Meek, C. E., Manson, A. H., and Mitchell, N. J.: Evidence of a role for modulated atmospheric tides in the dependence of sporadic E layers on planetary waves, J. Geophys. Res., 108(A5), 1176, doi:10.1029/2002JA009788, 2003.

Pannekoek, A.: Über die Erscheinungen, welche bei einer Sternenbedeckung durch einen Planeten auftreten, Astronomische Nachrichten, 164, 5–10, 1904.

Pirscher, B., Foelsche, U., Borsche, M., Kirchengast, G., and Kuo, Y.-H.: Analysis of Migrating Diurnal Tides Detected in FORMOSAT-3/COSMIC Temperature Data, J. Geophys. Res., in press, 2010.

Plane, J. M. C.: Atmospheric Chemistry of Meteoric Metals, Chem. Rev., 103, 4963–4984, 2003.

Poli, P., Moll, P., Puech, D., Rabier, F., and Healy, S. B.: Quality Control, Error Analysis, and Impact Assessment of FORMOSAT-3/COSMIC in Numerical Weather Prediction, Terr. Atmos. and Oceanic Sci., 20, 101–113, doi:10.3319/TAO.2008.01.21.02(F3C), 2009.

Prölls, G. W.: Physik des erdnahen Weltraums, Springer-Verlag, 2004.

Ratcliffe, J. A. and Weekes, K.: PHYSICS of the UPPER ATMOSPHERE, chap. The Ionosphere, pp. 377–470, Academic press New York and London, 1960.

Reigber, C.: CHAMP – A challenging micro-satellite payload for geophysical research and application, Feasibility study for DARA, Final Report, Potsdam, 1995.

Reigber, C., Lühr, H., and Schwintzer, P., eds.: First CHAMP Mission Results for Gravity, Magnetics and Atmospheric Studies, Springer-Verlag Berlin, Heidelberg, New York, 2003.

Reigber, C., Lühr, H., Schwintzer, P., and Wickert, J., eds.: Earth Observation with CHAMP Results from Three Years in Orbit, Springer Berlin, Heidelberg, New York, 2005.

Rendtel, J.: Sternschnuppen, Urania-Verlag, 1991.

Rocken, C., Anthes, R., Exner, M., Hunt, D., Sokolovskiy, S., Ware, R., Gorbunov, M., Schreiner, W., Feng, D., B., H., Kuo, Y.-H., and Zou, X.: Analysis and validation of GPS/MET data in the neutral atmosphere, J. Geophys. Res., 102, 29 849–29 866, 1997.

Rocken, C., Kuo, Y.-H., Schreiner, W. S., Hunt, D., Sokolovskiy, S., and McCormick, C.: COSMIC System Description, Terr. Atmos. and Oceanic Sci., 11,1, 21–52, 2000.

Schmidt, T., Wickert, J., Beyerle, G., and Reigber, C.: Tropical tropopause parameters derived from GPS radio occultation measurements with CHAMP, J. Geophys. Res., 109, D13 105, doi:10.1029/2004JD004566, 2004.

Schmidt, T., Wickert, J., Beyerle, G., and Heise, S.: Global tropopause height trends estimated from GPS radio occultation data, Geophys. Res. Lett., 35, doi:10.1029/2008GL034012, 2008.

Schreiner, W. S., Sokolovskij, S. V., Rocken, C., and Hunt, D. C.: Analysis and validation of GPS/MET radio occultation data in the ionosphere, Radio Sci., 34, 949–966, 1999.

Smith, E. K., J. and Matsushita, S., eds.: International Series of Monographs on ELECTROMAGNETIC WAVES, Pergamon Press, 1962.

Syndergaard, S.: Retrieval of electron density profiles at CDAAC, CEDAR-DASI Workshop, Santa Fe, New Mexico, 2007.

Tricomi, F. G.: Integral Equations, Dover Publications, 1985.

Tsybulya, K. and Jakowski, N.: Medium- and small-scale ionospheric irregularities detected by GPS radio occultation method, Geophys. Res. Lett., 32, L09 103, doi: 10.1029/2005GL022420, 2005.

Tyler, G. J.: Radio propagation experiment in the outer solar system with Voyager, Proc. of the IEEE, 10, 1404–1431, 1987.

Ward, A., Bagiu, M., and Reigber, C.: GRACE Gravity Recovery and Climate Experiment, Goddard Space Flight Center, Greenbelt, Maryland, USA, 2004.

Ware, R., Exner, D., Feng, M., Gorbunov, M., Hardy, K., Herman, B., Kuo, Y., Meehan, T. K., Melbourne, W. G., Rocken, C., Schreiner, W., Sokolovskiy, S., Solheim, F., Zou, X., Anthes, R., Businger, S., and Trenberth, K.: GPS sounding of the atmosphere from low Earth orbit – preliminary results, Bull. Am. Met. Soc., 77, 19–40, 1996.

Whitehead, J.: The formation of the sporadic-E layer in the temperate zones, J. Atmos. Terr. Phys., 20, 49–58, 1961.

Whitehead, J.: Recent work on mid-latitude and equatorial sporadic-E, J. Atmos. Terr. Phys., 51, 401–424, 1989.

Whitehead, J. D.: Formation of the sporadic E layer in the temperate zones, Nature, 188, 567–567, 1960.

Whitehead, J. D.: Theory of equatorial sporadic E, J. Atmos. Terr. Phys., 25, 167–173, 1963.

Wickert, J.: Das CHAMP-Radiookkultationsexperiment: Algorithmen, Prozessierungssystem und erste Ergebnisse, Ph.D. thesis, Karl-Franzens-Universität zu Graz, STR 02/07 GeoForschungsZentrum Potsdam, 2002.

Wickert, J., Reigber, C., Beyerle, G., König, R., Marquardt, C., Schmidt, T., Grunwaldt, L., Galas, R., Meehan, T. K., Melbourne, W. G., and Hocke, K.: Atmosphere Sounding by GPS Radio Occultation: First Results from CHAMP, Geophys. Res. Lett., 28 (17), 3263–3266, 2001.

Wickert, J., Pavelyev, A., Liou, Y., Schmidt, T., Reigber, C., Igarashi, K., Pavelyev, A., and Matyugov, S.: Amplitude variations in GPS signals as a possible indicator of ionospheric structures, Geophys. Res. Lett., 31, L24 801, doi:10.1029/2004GL02607, 2004.

Williams, B. P., Croskey, C. L., She, C. Y., Mitchell, J. D., and Goldberg, R. A.: Sporadic sodium and E layers observed during the summer 2002 MaCWAVE/MIDAS rocket campaign, Ann. Geophys., 24, 1257–1266, 2006.

Wu, D. L., Ao, C. O., Hajj, G. A., de la Torre Juarez, M., and Mannucci, A. J.: Sporadic E morphology from GPS-CHAMP radio occultation, J. Geophys. Res., 110, A01 306, doi:10.1029/2004JA010701, 2005.

Yunck, T. P., Lindal, G. F., and Liu, C.-H.: The role of GPS in precise Earth observation, Proc. of the IEEE, Position, Location and Navigation Symposium, Orlando, Florida, USA, 1988.

Yunck, T. P., Liu, C. H., and Ware, R.: A history of GPS sounding, Terr. Atmos. and Oceanic Sci., 11, 1–20, 2000.

Zhang, S. P., McLandress, C., and Shepherd, G. G.: Satellite Observations of mean winds and tides in the lower thermosphere. Part 2: WINDII monthly winds for 1992 and 1993, J. Geophys. Res., 112, doi:10.1029/2007JD008457, 2007.

Acknowledgements

First of all I would like to thank Prof. Dr. Christoph Jacobi for supervising this thesis. The spatial distance between Potsdam and Leipzig disappeared due to hours of insightful personal discussions, phone calls and reams of motivating and supporting emails. Thank you very much for many helpful ideas solving scientific problems. Further, I deeply appreciate your valuable contributions for the papers and the DFG application.

My special thank goes to Dr. Jens Wickert who gave me the opportunity to work on this challenging research topic. Thank you for your support, guidance and the exceptional possibilities I had during the past years. For a PhD student it is not common to have the chance to publish my results and to attend several international conferences where I met many colleagues who gave me useful hints in data interpretation.

I wish to thank the GFZ section 1.1 members, especially Dr. Stefan Heise, Dr. Torsten Schmidt, and Dr. Georg Beyerle for the positive and productive working atmosphere, for providing the preprocessed radio occultation data sets, IDL and Matlab routines, and for assisting with helpful comments. I'm grateful also to Mrs. Hemmerling and to Mrs. Winkler for taking over much of the accruing administration work.

I am also obliged to Prof. Dr. Hermann Lühr for his help in interpreting the sporadic E data especially in connection to magnetic field properties.

Zum Schluss möchte ich mich auch bei meinen Mädels Kathrin, Stefanie und Ana ganz herzlich bedanken. Ihr habt den Alltag auf eure liebe und humorvolle Art unheimlich aufgelockert, habt mich immer wieder motiviert und mir zugehört, wenn es Probleme gab und ihr seid mir beim Korrekturlesen eine große Hilfe gewesen.

Ein ganz liebes Dankeschön soll an Holger, an meine Familie und an meine Freunde gehen. Es ist einfach gut zu wissen, dass ihr immer für mich da seid und dass ich meinen Weg nicht allein gehen muss. Danke, für die unendliche Geduld, die ihr mir entgegenbringt, die viele Zeit, die ihr euch nehmt, um mich zu unterstützen und die schier grenzenlose Motivation und positive Lebenseinstellung, die ihr vermittelt.